Universität zu Köln
Institut für Kernphysik

Neutron Induced Single-Event-Effects in Gallium-Nitride High Electron Mobility Transistors

Inaugural-Dissertation

zur

Erlangung des Doktorgrades

der Mathematisch-Naturwissenschaftlichen Fakultät

der Universität zu Köln

vorgelegt von

Dorothea Wölk

aus Aachen

Gutachter: Prof. Dr. Alfred Dewald
Prof. Dr. Thomas Michely

Tag der Disputation: 05.03.2024

Dissertation accepted by the Faculty of Mathematics and Natural Sciences of the University of Cologne in 2024.

Abstract

This work is focused on the study of radiation-induced, especially neutron induced, single event effects in normally off gallium nitride high electron mobility transistors (GaN HEMTs). Normally off gallium nitride high power transistors have been commercially available on the market for a short number of years. Due to a large bandgap between conduction and valence band, this semiconductor material is inherently more resistant to failure due to induced charge carriers. In particular, the sensitivity to charge introduced by single particles has thus far only been investigated briefly. The knowledge about the reliability of the devices against radiation effects is important to ensure the reliability and functionality for safety-relevant applications in space as well as on Earth. At this point in time, no protocols for testing GAN HEMTs on radiation hardness and single event effects have been published.

In this study, three commercially available gallium nitride high electron mobility transistors of different device designs were investigated and compared with respect to their sensitivity to single event effects caused by radiation, especially neutrons. For this purpose, the devices under test were irradiated with the same assembly using five different types of particles and measured online. Irradiation was performed using high-energy xenon ions, ultra-high-energy lead ions, high-energy protons, monoenergetic neutrons and neutrons whose energy is similar to the atmospheric spectrum. The devices were irradiated with drain voltage applied but blocked and for each measured device the leakage current between drain and source as well as gate and source were recorded, likewise failures of the devices due to short circuit were registered.

From the measurement data it was possible to determine the failure rate and the cross section for Single Event Effects due to particle ion interactions. Furthermore, the dependence of the failure rate on the energy deposition in the material and the comparability of proton and monoenergetic neutron measurements with the failure rate due to atmospheric neutrons were investigated. By observing gate and drain leakage current, two different failure mechanisms could be observed.

In this work, no failures below 60% of the nominal drain voltage and 50% of the measured breakdown voltage of the devices were observed. Summarized and interpreted in the context of previous measurements, no inherent radiation hardness of the investigated gallium nitride high electron mobility transistors over comparable silicon or silicon carbide transistors could be shown for single particle effects.

Zusammenfassung

Diese Arbeit befasst sich mit der Untersuchung von strahlungsbedingten Einzelteilchen Effekten (SEE) in normal gesperrten Gallium Nitrid High Electron Mobility Transistoren (GaN HEMT Transistors). Erst seit wenigen Jahren gibt es kommerziell erhältliche selbstsperrende Gallium Nitrid Power Transistoren auf dem Markt. Dieser Halbleiter hat aufgrund seiner großen Bandlücke zwischen Leiter und Valenzband eine inhärente Widerstandfähigkeit gegenüber induzierten Ladungsträger. Dieser Vorteil wurde in Bezug auf Strahlungseffekte erst anfänglich untersucht. Insbesondere die Empfindlichkeit gegenüber eingebrachter Ladung durch einzelne Teilchen ist bisher kaum untersucht. Das Wissen über die Robustheit der Bauteile gegenüber Strahlungseffekten ist wichtig, um die Zuverlässigkeit und Funktionalität für sicherheitsrelevante Anwendungen im Weltall sowie auf der Erde zu gewährleisten.

In dieser Arbeit wurden dreie kommerziell erhältliche Galliumnitrid-Transistoren mit HEMT-Struktur aber unterschiedlichen Bauelementedesign hinsichtlich ihrer Empfindlichkeit gegenüber Einzelereignis-Effekten durch Strahlung, insbesondere Neutronen, untersucht und verglichen. Dafür wurden die Bauteile mit immer gleichem Setup mit fünf verschiedenen Teilchenarten bestrahlt und online gemessen. Bestrahlt wurde mit hochenergetischen Xenon-Ionen, ultra-hochenergetischen Blei-Ionen, hochenergetischen Protonen, monoenergetischen Neutronen und Neutronen, deren Energie dem atmosphärischen Spektrum ähnelt. Die Bauteile wurden mit angelegter Drain Spannung aber ungeschaltet bestrahlt und für jedes gemessene Bauteil wurde der Leckstrom zwischen Drain und Source, sowie der Leckstrom zwischen Gate und Source aufgezeichnet und Ausfälle der Bauteile durch Kurzschluss registriert.
Mit den Messungen war es möglich, die Ausfallrate und den Wirkungsquerschnitt für die Nukleonen-Wechselwirkungen zu bestimmen. Des Weiteren wurde die Abhängigkeit der Ausfallrate von dem Energieeintrag ins Material und die Vergleichbarkeit von Messungen mit Protonen und monoenergetischen Neutronen mit der Ausfallrate durch atmosphärische Neutronen untersucht. Durch die Beobachtung von Gate- und Drain-Leckstrom konnten zwei unterschiedliche Ausfallmechanismen beobachtet werden. Außerdem wurde der Einfluss der angelegten Drain- und Gate-Spannung auf die Bauteilempfindlichkeit untersucht.
Im Rahmen dieser Arbeit wurden keine Ausfälle unter 60% der Nenn-Drain-Spannung und 50% der gemessenen Durchbruchspannung der Bauelemente beobachtet. Zusammenfassend konnte für Einzelteilchen Effekte keine inhärente Strahlungshärte der untersuchten Gallium Nitrid High Elektron Mobility Transistoren gegenüber vergleichbaren Silizium- oder Siliziumcarbid-Transistoren für Neutronen gezeigt werden. Allerdings war der gemessene Wirkungsquerschnitt immer am unteren Ende zu den Vergleichsdaten.

Contents

List of Figures

List of Tables

Acronyms and Units

2DEG	Two-Dimensional Electrons Gas
AlGaAs	Aluminum Gallium Arsenide
AlGaN	Aluminum Gallium Nitride
ANITA	Atmospheric-like Neutrons at The Svedberg Laboratory (Uppsala, Sweden)
CERN	Conseil Européen pour la Recherche Nucléaire (Genf, Switzerland)
CHARM	Cern High energy AcceleRator Mixed Field Facility
ChipIR	Radiation chamber at the ISIS
COTS	Commercial Of The Shelf
DD	Displacement Damage
DUT	Device Under Test
E_G	Bandgap Energy
E_F	Fermi Level
ELDRS	Enhanced Low Dose Rate Sensitivity
ESD	Electrostatic Discharge
FBH	Leibniz Ferdinand-Braun-Institut (Berlin, Germany)
FIT	Failure In Time
GaAs	Gallium Arsenide
GaN	Gallium Nitride
GANIL	Grand Accélérateur National d'Ions Lourds (Caen, France)
HEMT	High-Electron-Mobility Transistor
HFETs	Heterostructure Field-Effect Transistors
I_{DS}	Drain leakage current
I_{GS}	Gate leakage current
IEL	Ionizing Energy Loss
IGBT	Insulated-Gate Bipolar Transistor

INT (FhG)	(Fraunhofer-) Institut für Naturwissenschaftlich-Technische Trendanalysen (Euskirchen, Germany)
ISIS	Neutron and Muon Source at the Rutherford Appleton Laboratory (Oxfordshire, United Kingdom)
LET	Linear Energy Transfer
MOSFET	Metal–Oxide–Semiconductor Field-Effect Transistor
μ	carrier mobility
NIEL	Non-Ionizing Energy Loss
rad	radiation absorbed dose $[1\,rad = 0.01\,Gy = 0.01\,\frac{J}{kg}]$
SEB	Single Event Burnout
SEE	Single Event Effects
SEGR	Single Event Gate Rupture
Si	Silicon
SiC	Silicon Carbide
SMU	Source Measurement Unit
TID	Total Ionizing Dose
TRIUMF	Tri-University Meson Facility (Canada)
TSL	The Svedberg Laboratory
V_{DS}	Drain Source Voltage
V_{GS}	Gate Voltage
WNR	Weapons Neutron Research at the Los Alamos Neutron Science Center (USA)

1. Introduction

Although cosmic rays and their effect in the atmosphere have been known since the beginning of the last century [1], the effects of radiation on semiconductor devices were not initially considered. Even the first reports about strange electronic failures in connection with radiation were ignored at the time. As early as the first above-ground nuclear bomb tests, between 1954 and 1957, many different anomalies in the electronics used were reported and even complete failure of some devices was also observed. A rough estimate at that time was that the failures started at a particle impact of about $10^{11}\,particles/cm^2$ [2].
Notably in the late 1950s and fueled by more extensive satellite testing, atmospheric radiation from cosmic rays again became a focus of research and extensive studies of cosmic rays began in the International Geophysical Year 1957. Nevertheless, even in further development, early satellite electronics proved to be unreliable [3]. At this point, electronic components were evolving rapidly, becoming smaller and requiring less voltage to switch, meaning that less charge was needed for one state or another. Particularly in early digital and memory technology, the susceptibility of electronic components to the charge introduced by ionization became apparent, this was often the first area of research due to these factors. In contrast to this, larger power devices that operated with larger electric fields were found to be not as sensitive to radiation introduced ionization.
In 1978, it was first published that alpha particles can also cause failures in computer memory RAMs. The component defects at sea level were caused by the decay of an alpha emitter that had been incorporated into the device during the production process of the ceramic package. Further investigation revealed that the manufacturing company in Colorado was located downstream an old uranium mine, leading to contamination of the packaging material [4]. These first indications that not only in satellites but also in everyday applications device failures can be caused by injected particle radiation, which set off a cascade of more in-depth investigations into the radiation resistance of electronic components.
It was shown that not only ionization produced by heavy ions but also individual nuclear reactions can lead to component failure [2], to which the first specific heavy ion tests on satellite electronics were attempted [5].
With the more frequent discovery of errors in other electronic components, such as the failure of bipolar RAMs in 1980 due to alpha particles, it became apparent that this failure

mechanism must be considered more comprehensively.
At this time, Ziegler and Lanford began studies on terrestrial cosmic rays and their effects at sea level in more detail and published estimates of the particle showers that reach the Earth's surface, as well as their effect on electronic devices and a first concept of error frequency estimation [6].
Furthermore, mass testing of electronic components at various altitudes has since been conducted by several research groups. Thus, several hundred components were deliberately operated underground, at sea level, at an elevation of 1500 m and at an elevation of 3000 m in order to be able to determine an altitude dependency [2]. Until the 1990s, mass tests were regularly performed on the Jungfraujoch (Grindelwald, Switzerland) in the Alps to predict an altitude-dependent error rate [7].
Ideas began to form on how to speed up these very time and material-consuming measurements in order not to be engaged in testing for months or even years during the production of the components. However, the atmospheric neutron spectrum was difficult to reproduce at the time, and so the scientists began to experiment with monoenergetic and thermal neutrons. In 1984 the first tests with monoenergetic neutrons and protons were carried out to find an alternative. The results showed a comparability between the neutron and proton testing, so that with a scaling factor prediction could be made about the failure rates due to cosmic ray produced neutrons and pions [6]. During 1991, the first study of particle-induced failure mechanisms in electronic devices using a microbeam was published [8]. Since then, there have been more and more in-depth experiments and simulations, so that the failure mechanisms triggered by heavy ions, neutrons or protons in silicon devices are very well studied and understood. There is now extensive literature and test standards for various altitudes and applications [9, 10, 11, 12, 13].
Additionally, it became clear in the 1990s, following inexplicable failures of traction propulsion converters, that power electronics could also be affected by terrestrial cosmic rays. To support the assumption that cosmic radiation was responsible for the failures, the failure rate of the components was measured under the following conditions: a laboratory with a tin roof, in the basement of a high rise building with 2.5 m concrete shielding, and in a salt mine 140 m below ground. As one can see in figure 1.1 during the measurements in the salt mine there were no failures to be seen, which confirmed the hypothesis that even high-power transistors could be vulnerable to (cosmic) radiation [14].
Today nearly all safety-related electronic systems like airplanes, satellites and automotive are regularly analyzed for single event effect (SEE)-susceptibility. Even so despite the fact that the knowledge of silicon-based technologies such as transistors, diodes and other electronic components is quite extensive, the emerging change in energy supply and increasing energy consumption will lead to the need for more efficient, lower-loss technologies.

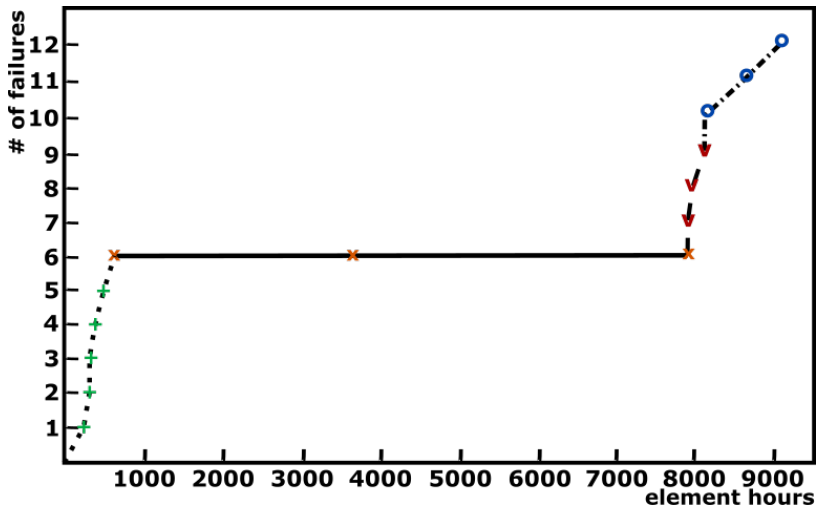

Fig. 1.1.: Failure rate of power diodes vs. time measured in the laboratory (+ and v), salt mine (x) and the basement of a high-rise building (○), from [14]

Silicon-based MOSFETs have a technological limit at around 600V, so other materials and designs are increasingly being used [15]. First and foremost, compound semiconductors such as silicon carbide and gallium nitride promise better conditions for handling high voltages due to their larger bandgap and thermal conductivity. The various advantages of individual materials are shown in figure 1.2. A clear superiority of the wide bandgap materials over silicon can be observed. Silicon carbide is slightly more thermally conductive than gallium nitride, but in return gallium nitride can withstand higher electric fields. There are now a large number of technologies and materials on the market, of which each can cover a part of the applications in the best way possible.

Commercial gallium nitride transistors, mainly in the form of high electron mobility transistors, have been on the market since approximately 2010. These devices take advantage of the wide bandgap of gallium nitride and the piezoelectric effect when two different crystal lattice constants meet to create a lateral working component whose structure and operation differ significantly from conventional silicon and silicon carbide transistors. Due to the lateral principle of operation, the natural state of such a transistor is conductive (normally on), and it is only in recent years that technological development has progressed to such an extent that it has been possible to produce non-conductive components in the non-switched state (normally off). These components are of great interest for the upcoming electrification, as they have a very low weight and volume at high power capability and thus bring less additional weight, for example, into cars or airplanes. Most specifically in such applications, reliability is of utmost importance.

However, because of the type of component at this stage of development, specifically the normally off design, which is fairly new, little empirical values or statistically reliable studies

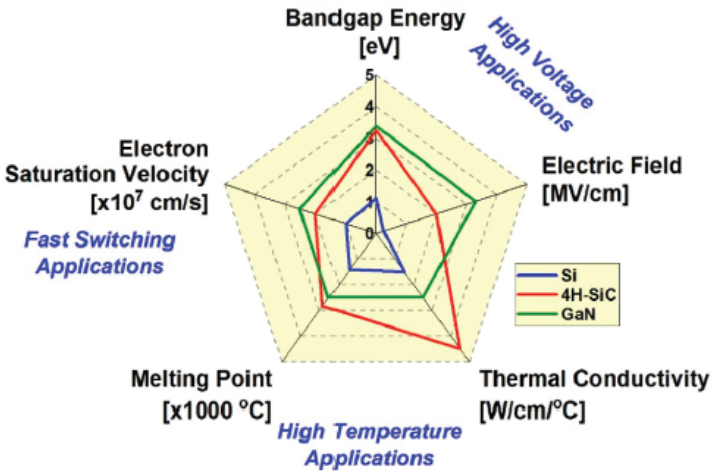

Fig. 1.2.: Comparison of the material properties between silicon (blue), silicon carbide (red) and gallium nitride (green) [15].

to radiation reliability are available at this point in time. Initial studies on normally on devices have been published since 2014, but normally off devices are now only slowly coming to the attention of radiation effects studies.

Aim and Outlook of this Thesis

The aim of this work was to investigate the relatively new commercial off the shelf (COTS) normally off gallium nitride (GaN) high electron mobility power transistors (HEMTs) for their single event effect (SEE) radiation sensitivity in terrestrial applications.
The investigation of radiation induced effects on this type of component is still in its infancy. Only in the last years have there been the first publications about distinct SEE testing on these devices [16, 17, 18, 19, 20, 21]. At the beginning, mainly low-voltage and normally on components were investigated as those have been available on the market for some time and are suitable for the use in high-frequency circuits. Over the last five years, the focus has shifted to power transistors with applications above $300\,V$ and normally off devices. For this work, commercially available gallium nitride high electron mobility transistor components of dissimilar device designs were selected and comparative SEE measurements under different radiation environments were made.
As an approach to the topic the next chapter gives an overview on semiconductor devices and the important properties for radiation effects. Following a description of the different radiation environments on Earth and in space, the interaction of particles with matter is discussed, focusing specifically on the effects of particle irradiation in semiconductor devices.

In particular, the special features of the gallium nitride high electron mobility transistor and the current state of research on radiation effects in the same will be discussed.
Chapter three includes the method and standards for single event effect testing in power transistors as well as the experimental setup and the procedure for the measurements performed.
In chapter four the properties of the selected components and the carried-out experiments are described. A distinction between three heavy ion and proton tests and two neutron experiments is made. In the individual subchapter, both the accelerator facility and the time and conditions of the irradiation are described and the different irradiation steps are presented as first results.
Presented in chapter five are the experimental evaluation and the interpretation. The significance and conclusions drawn from the measurements are also discussed.
Finally, the study is summarized once again and further research possibilities are presented.
In the appendix the logbooks of the experiments and further plots from the experimental data are given.

2. Background, Theory and Current State of Knowledge

The goal of this chapter is to give a short overview of the theoretical background needed for SEE testing in semiconductor technologies. For this purpose, the properties of semiconductors as well as different radiation environments, their occurrence and the effect of radiation on matter and semiconductor devices are briefly discussed.
In the following the special properties of the compound semiconductor gallium nitride and the high electron mobility transistor design will be discussed, as well as previous research results of radiation tests and emerging failure mechanisms of this type of devices.

2.1. Semiconductors

2.1.1. Bandgap and Electron Density

The energy distribution of electrons in solid materials is given through the atoms energy states. In solids these states split into more energy states forming electron bands which can be occupied fully, partially or left empty. In the unexcited condition, the internal states are fully occupied and the last occupied band is called the valence band, higher lying is called conduction band.
Metals have a high electron density and form band structures within the Fermi-energy, allowing free movement of electrons. The clearance between the valence band and the conduction band is called bandgap and is the most important factor for the conductivity of a material, because it determines how much energy is needed to excite an electron in order to create the possibility to move between atoms. Metals have bandgaps below $0.4\,eV$, bandgaps between $0.4\,eV$ and $4\,eV$ are classified as semiconductors and bandgaps over $4\,eV$ as isolators [22].
If energy is introduced into the solid one or more electrons can be excited and change from the valence band to the conduction band. This is called an excited state. In this process, the electrons from the valence band leave a positive hole. The electrons, like the holes, in the conduction band have a high mobility and thus lead to the conductive property of the

solid. The electron density is given by the Fermi-Dirac distribution [23].
The Fermi level may be considered as reference energy under equilibrium conditions. Intrinsically the semiconductor Fermi level is near the center of the bandgap between valence and conduction band but the temperature dependence of $f(E)$ causes many semiconductor properties to shift.
Although both electrons and holes can move in the band structure, the effective mass of both determines that electrons are much more agile and therefore contribute more to the conductivity of a material.

2.1.2. Direct and Indirect Bandgap

Conductivity depends on the carrier motion possibility which is mainly influenced by the crystal properties as well as the electron density given by the Fermi-Dirac Equation.
The particle energy for electrons and holes is given by

$$E = \frac{\hbar^2 k^2}{2 m_{eff}} \tag{2.1}$$

with $\hbar k = p$ the particle momentum and the effective mass m_{eff}.
m_{eff} is higher for holes than for electrons thus the hole velocity is lower than the velocity of electrons.
Recombination and absorption probability of electrons through the bandgap is dependent on the position of band structures minimum and maximum in the $E - k$ diagram (example for GaN in figure 2.7). If the minimum of the upper quantum state has the same k-vector as the maximum of the lower quantum state direct band-to-band transitions are possible. When they have different k-vectors the transition needs additional momentum, usually from a phonon, as the momentum of a photon normally is too small. These are called indirect transitions. For indirect semiconductors this probability is low but it is often the dominant recombination way for direct semiconductors (light emitting diodes and lasers).

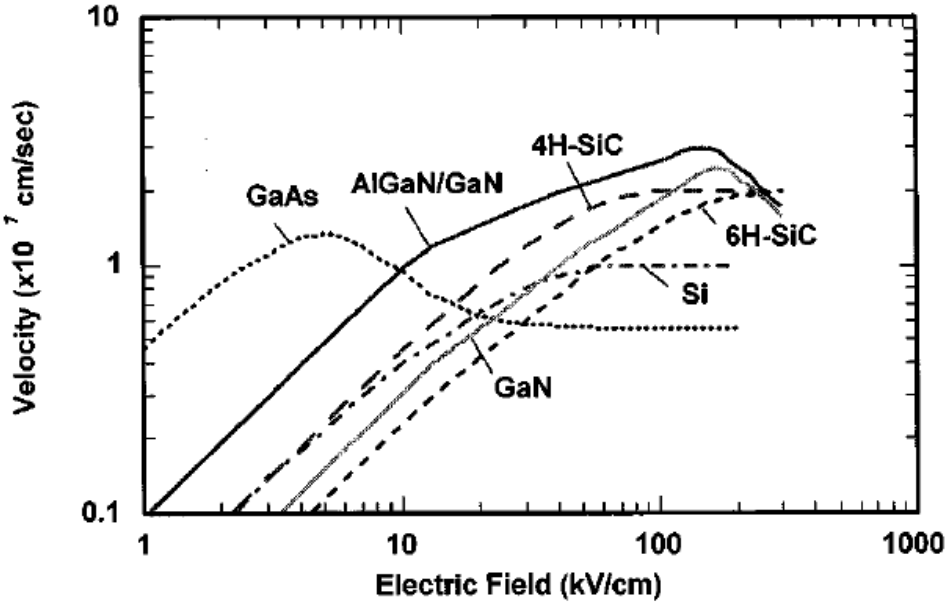

Fig. 2.1.: Electron velocity versus electric field for some semiconductor materials [25]

2.1.3. Carrier Density and Transport

Even in equilibrium the thermal energy can lift electrons from the valence to the conduction band, in addition, the material intrinsic carrier density depends on the energy, temperature and bandgap width

$$n_i^2 \;=\; N_C\, N_V\, e^{-E_G\,/\,kT} \tag{2.2}$$

with N_C =carrier density in the conduction band, N_V =carrier density in the valence band and E_G =the bandgap energy [26].

Gallium nitride (GaN) and Silicon carbide (SiC) have low values of n_i which allows them to work at high temperatures with low leakage current. Dopants and impurities in the crystal affect these properties, but since doping is irrelevant for the mode of operation in the devices under test in this work it will not be further discussed here.

The carrier transport within the crystal structure can take place through diffusion or drift processes. In presence of a concentration gradient ($\frac{dN}{dx}$), a diffusion current from carrier diffusion occurs, creating a diffusion current density J

$$J \;=\; q\,D\frac{dN}{dx} \tag{2.3}$$

with q = charge, $D = \mu\frac{kT}{q}$ =diffusion constant (Einstein relation) and μ the carrier mobility possibility due to drift. μ is dependent on an electric field and given by $\mu = \frac{v}{E}$

with v the velocity and E the electric field [12] as is shown in figure 2.1 where the velocity is plotted against the electric field. In semiconductors the mobility decreases with increasing doping concentration due to carrier scattering.
A bandgap junction that forms when two semiconductors with different bandgaps are placed in contact is called heterojunction. The differences in the bandgaps of the materials form a discontinuity in the band diagram (band offset), hindering the carrier flow. These differences are asymmetrical between valence and conduction band. Conduction about the heterostructure depends exponentially on the barrier height, while additionally the offset must be large enough to prevent leakage [23].
For heterostructures of the same material the bandgap is defined by the molar fraction. For example, the valence band offset of $Al_XGa_{(1-X)}As$ is $\Delta E_v = 0.55\, X_{Al}$ that gives a bandgap of

$$E_G = 1.25\, X \tag{2.4}$$

2.2. Radiation and the Effects in Electronic Devices

2.2.1. Environmental Radiation

Systems for space, aviation or Earth applications are exposed to various radiation environments during their service life. Here, we will briefly describe those environments that can affect the performance of components. The three big sources are cosmic radiation that comes from outer space, terrestrial radiation from the Earth and human made radiation environments. In particular, the particle type and energy characteristic of these environments will be mentioned. However, not only the type of particle, but also the particle's energy distribution and possible shielding is important when predicting the radiation effect for semiconductor devices [12]. A rough overview of the main occurrences of the particle species is shown in the table 2.1.

Cosmic Radiation

The term cosmic radiation concerns different environments, which consist mainly of protons and/or electrons as the most numerous particles, followed by heavy ions. Their appearance and distribution can have different origins [27].

Galactic Cosmic Rays

The origin of the galactic cosmic rays is not yet completely clarified but they affect every place in the universe [28]. They consist for the most part of hydrogen together with a mix of other fully ionized nuclides (50% protons, 25% alpha particles, 13% CNO-nuclides (carbon, nitrogen and oxygen), 1% electrons and 1% others). Most of the particles have atomic numbers $< Z = 26$. The cosmic ray fluence rate can be assumed as

$$\frac{dN}{dE} \propto E^{-3} \tag{2.5}$$

with around $10^4 \frac{1}{cm^2\, s}$ with an energy of $100\, MeV$ [27]. Despite the fact that particles with low energies can be shielded against, a large number of ions with extremely high energies remain which are difficult to protect from.

Solar Flares

Heavy particle flares and coronal mass ejections from the sun produce energetic protons and heavy ions which travel along the magnetic field lines of the sun. Some of them reach the Earth and can cause significant damage to electronic systems and devices. The distribution of ion species is similar to the galactic cosmic rays, but on average the energy is lower.

Tab. 2.1.: Incomplete overview of the main particles in the respective environment [12].

Particle	**E [MeV]**	**Environment**
p	1 - 500	Earth radiation belts and solar flares
e^-	< 7	Earth trapped radiation belts
n	0.001 - 1000	terrestrial (cosmic ray interaction in the atmosphere)
α	< 9	decay from radioactive impurity in the device
galactic		
cosmic rays	$< 20000^*$	steady background in deep space

*a very small number of cosmic rays have much higher energies

Near Earth Electron and Proton Belts

The magnetic dipole field of the Earth traps high energy charged particles spiraling along its field lines. These trapped particles near the Earth consist of protons and electrons in large numbers around the Earth's atmosphere, forming a belt like area. At the pole region they are reflected along the magnetic field lines in the opposite direction.

There are three radiation belts, a proton belt and an inner and outer electron belt. The distribution is geometrically more complicated than bands weakening towards the poles and not constant with height, but on average, the inner electron belt at the equator extends from the atmosphere to an altitude of about 7 km. Electrons in the inner belt have lower energies than those in the outer belt or the protons. The outer electronic belt reaches up to a height of 55000 km. Between the two electron belts lies the proton belt, which extends, on average from 6400 km to a height of 24000 km at the equator and lower at the poles, thus partially overlapping the electron belts. The energy distribution for those protons differs in height but can reach energies higher than 500 MeV.

In addition, at the South Atlantic Anomaly, roughly over Brazil, the proton belt extends down to 200 km above the Earth surface. The reason for this is the slightly shifted and rotated magnetic axis (to the Earth axis).

Depending on the orbit altitude, the radiation belts are the main cause of radiation effects in spacecrafts. The orbits can pass through the proton as well as the electron belt.

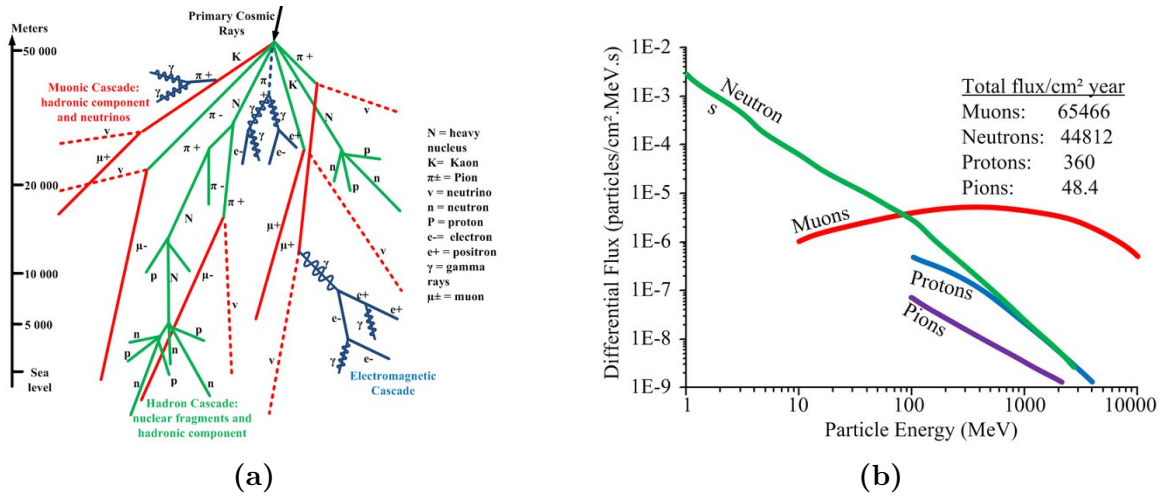

(a) **(b)**

Fig. 2.2.: (a) Particle shower of possible secondary reactions in the Earth's atmosphere. (b) Energy spectrum of the produced particles at sea level (New York) [29].

Terrestrial Radiation

Radioactivity occurring on Earth can be roughly summarized into three categories:

- primordial radionuclides
- cosmogenic radionuclides
- human produced radionuclides

Primordial particles have their origin in three still existing natural decay chains from the Thorium-, Uranium- and Actinium series. The main radiation of interest product are alpha particles, affecting semiconductor and electrical system per impurities in material, metallization and refractory metals.
From cosmic rays entering and interacting with the atmosphere various ionized particles are generated. Through further interactions between the secondary particles and the atmosphere, a cascade of mainly pions, muons, nucleons, electrons and photons is formed, when reaching sea level as is shown in the left part of figure 2.2 [6].
Neutrons are produced in the outer atmosphere by cosmic rays interacting with nitrogen and oxygen. The small but significant flux of atmospheric neutrons on the Earth's surface varies with the location and increases with altitude [1]. In New York at sea level it is about $13\frac{n}{cm^2\,hour}$ and is often given as reference flux [10]. The energy distribution of produced particles at sea level in New York is shown in the right part of figure 2.2. The total flux of the neutrons decreases with increasing neutron energy [6].
Furthermore, there are residuals of human-produced radiation from nuclear weapon testing, nuclear reactor emissions, and other experiments since the middle of the 20th century. The

effects are still measurable and give us an extra plus for the natural radiation. Both man-made radioactivity and naturally occurring radioactivity vary significantly from place to place.
One place where the radioactive environment is evident but still has to be considered for electronic systems is in nuclear reactors and experimental sites for accelerators or handling of radioactive substances. Gamma radiation, total dose levels above $1\,Mrad(Si)$[1], and high intensity of fission neutrons are part of everyday life there.

2.2.2. Particle Interactions

In order to evaluate the potency of radiation effects in semiconductors, it is necessary to briefly discuss the different interactions of particles with matter.

Gamma Rays

γ-rays interact with the electron of the atom via photo effect, Compton effect or pair production depending on the energy. The amount of naturally occurring gamma radiation has a negligible effect on electronic components but Co60-sources are often used to study the ionizing effect on materials and devices. Co60 produces γ-rays with $E_\gamma = 1.17\,MeV$ and $E_\gamma = 1.33\,MeV$ which in turn produce high energy electrons via Compton scattering and pair production. Electron energy peaks about $500\,keV$ and produces ionization effects [22] as well as vacancies and interstitials.

Electrons

Electrons interact through inelastic scattering and ionization while the possibility of scattering rises with the electrons energy decreasing. Table 2.2 gives the ionization potential of electrons, protons and alpha particles for the energy of 1 and $10\,MeV$. Because the energy transfer from the electron is small, it can travel a long distance with many collisions and is significantly deflected because of the low mass. Furthermore, the electron and electron scattering take place between indistinguishable particles [30]. Finally, the depleted electron is absorbed by an atom by forming an anion or neutralizing a cation and with that can change the doping of a semiconductor.
For fast electrons with an energy above $1\,GeV$ Bremsstrahlung production is the dominating process but this has no major part in single event effects on semiconductor devices.

[1] *rad* is a CGS-unit of absorbed radiation dose, which is still partly used; $100\,rad = 1Gy$ in SI-units

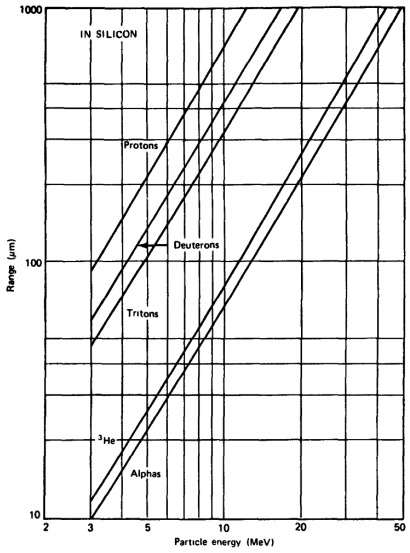

Fig. 2.3.: Calculation of the particle ranges vs. energy for different particle types within silicon in a log-log plot. It shows the empirical dependency $R = a\,E^b$ where the slope depending on b is not really variant for the different particles [22].

Protons

Protons are the most numerous particles in space. Due to the large number of events, there is a uniformly distributed amount of damage in a device. The proton interaction with matter depends on the proton energy.
Low-energy protons interact mainly via Coulomb scattering and cause more damage through displacement and ionization effects. Thereby the dominant mechanism is ionization of the material through the production of electron-hole pairs while losing energy.
High-energy protons interact more via nuclear reactions and nuclear-scattering, with the consequence that above $50 - 100\,MeV$ the radiation effects from protons and neutrons are comparable [31].

Alpha Particles and Heavy Ions

α-particles and heavier charged particles (ions above $A = 4$) interact mainly via Coulomb interactions by ionization due to creation of electron-hole pairs and excitation of electrons in the valence band [28]. Energy loss within the material for high initial energies is described by the Bethe-Bloch-formula. In figure 2.3 the range in silicon is shown for different particle types. The energy deposition occurs in the material and therefore the slowing power per path length is described by the Bragg curve.
For both alpha and heavy ion particles, there are nuclear reactions also possible but have a much lower probability. Nuclear reactions within the crystal material can be such as

transfer-, fusion- and compound reactions.
The nuclear reaction products are also charged particles with a high energy but shorter range which lead to further ionization in the crystal. Since fusion products normally occur ionized, an electron pickup reaction takes place decreasing $\frac{dE}{dx}$ and counteracts the effect of the increased energy at reduced velocity [22].
For less ionized particles like Alpha-particles the electron pickup does not become significant until the near end of their path. They are the decay-products within the semiconductor material due to incorporation of radioactive impurities in the device.

Neutrons

Neutrons are not charged and do not interact with the electrons of the material. All ionization processes triggered by neutrons are from secondary reactions of the reaction products. The incoming neutron itself interacts via elastic and inelastic scattering, capture and nuclear reactions. The various probabilities of nuclear interactions with neutrons change with the neutron energy. For neutrons under $0.5\,eV$ (at room temperature), so called thermal and slow neutrons, the interactions include elastic scattering and most probable the capture reaction (n, γ). For faster neutrons the probability for scattering becomes greater and more energy is transferred to a recoil nuclide.
Overall having a small interaction probability and a long traveling distance the importance of neutron induced radiation effects in semiconductors were small. But with decreasing device size and faster switching, the devices' sensitivity to neutrons and alpha particles increases.

Muons are also part of the radiation environment but less relevant to single event effects in electronic devices. In this work only ions, protons and neutrons will be discussed as initial particles.

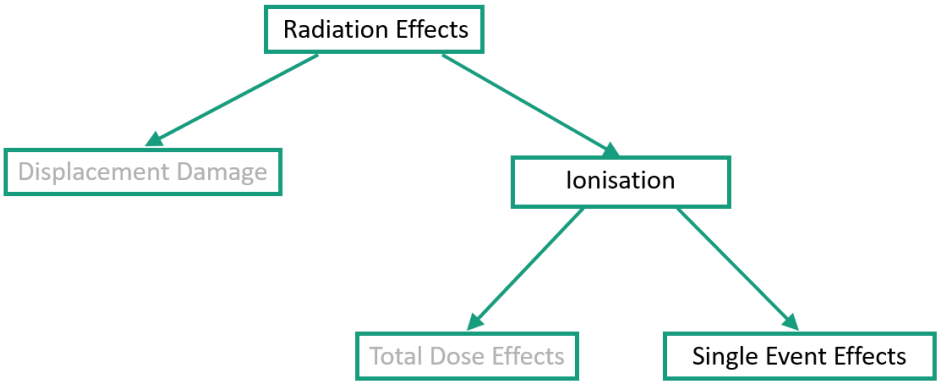

Fig. 2.4.: Categorization of radiation effects that can occur in semiconductor devices. Displacement damage and total dose effects are only mentioned briefly in this section.

2.2.3. Radiation Effects in Semiconductors

In semiconductor devices, radiation effects are manifested by a reduction in device characteristics, failure or destruction of the device. This appears through increased pair generation and recombination currents, reduced charge collection capability and shifting of the operating points of the components. Most failures due to radiation are the accumulation of small effects by a large number of particles from the radiation environment.
If a particle hits the device and its sensitive volume within the semiconductor structure it will interact through different processes with the material. Most common are

(i) energy loss due to interactions with electrons, which leads to ionization within the crystal (IEL, *ionizing energy loss*)

(ii) energy loss due to scattering, this moves atoms out of the crystal lattice and leads to defects like vacancies, interstitials, Frenkel pairs and dislocations (NIEL, *non-ionizing energy loss*).

A special case of (i) are so-called single event effects which can lead to the failure of a device by the deposited energy theoretically of a single particle. These effects (figure 2.4) and mechanism will be briefly outlined in the following.

Tab. 2.2.: Partial overview of particles electron-hole pair production of passing particles [33].

Energy	**α-particle**	**Protons**	**Electrons**
$[MeV]$	$[Ion\ pairs/cm]$		
1	60000	8000	50
10	16000	1000	45

Total Ionizing Effects

Incoming charged particles are most likely to interact with the numerous electrons in the crystal. Scattering leads to energy transfer, exciting the electron, raising it to the conduction band and creating a hole in the valence band (electron-hole pair). When this process happens due to photons the minimal energy needed for a direct semiconductor device is the bandgap energy. On average charged particles need 2.2-4 times the bandgap energy to create electron-hole pairs, since a part of the energy is needed by other interactions [32].
The dose for ionization effects are given in *rad*

$$1\,rad\ =\ 0.01\,Gy\ =\ 0.01\,\frac{J}{kg}$$

However, in excitation processes by heavy ions there is a shower of secondary electrons which can have an average path length of several lattice constants.
Semiconductor devices are sensitive to ionization taking place in the insulating regions and oxides, since the charge migrates quickly. The electrons are swept out by the field but the holes migrate more slowly due to their higher effective mass, leading to traps at boundary layers and changes of the surface state. This may change key properties of the semiconductor device like the threshold voltage or the leakage current. Charge trapping also occurs in compound semiconductors, but has less influence on the device properties because compound semiconductors have a greater surface state density and therefore traps have less influence in percentage terms [12].
The recombination of electron-hole pairs and the healing of traps decreases the damage that ionizing effects can have on semiconductors and is called *annealing*.

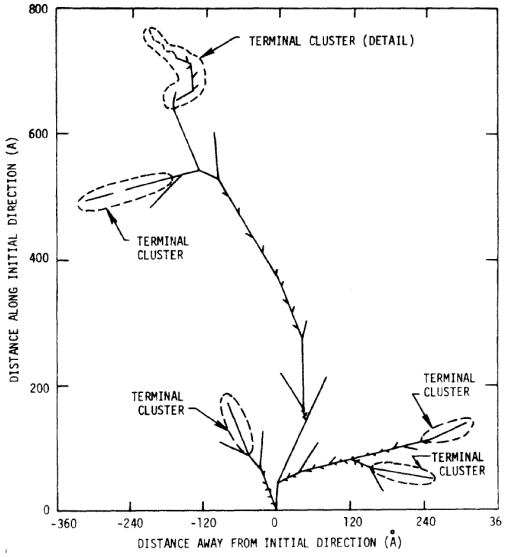

Fig. 2.5.: Calculation of neutron induced displacement damage in Si for $E_n = 50\ keV$ using Monte Carlo calculation and accounting for cluster defects [35].

Displacement Effects

After an initial high energy loss through electromagnetic interaction slowing down increases the probability of scattering for electrons and protons in semiconductors, Rutherford scattering (lattice damage) becomes more relevant than ionization [34]. The scattering can lead to displaced atoms within the crystal lattice mainly describable by elastic Rutherford scattering or so-called Coulomb scattering.

The minimum energy needed to move an atom from its lattice place is called displacement threshold energy and is correlated to the lattice binding energy. A comparison of the threshold energy T_D for Si, SiC and GaN is given in table 2.3.

Depending on the energy, different defects occur in the crystal. If the energy is rather low and close to T_D a defect interstitial (Frenkel pair) can form. Electrons in radioactive environments, especially in space, have such a high velocity that relativistic scattering has to be considered [34].

If the incoming energy is much higher than T_D the knock-on atom gets enough energy to interact further. These secondary knock-on reactions are shown in figure 2.5. It can be seen that an initial neutron with an energy of $500\,keV$ produces secondary knock-on atoms which travel several $10\,nm$ before stopping, producing vacancy-interstitial pairs and cascade damage regions [35].

Scattering from the atomic nuclei in the crystal is also possible but due to the Coulomb field the cross section for this is orders of magnitude smaller [34].

Disruption of the crystal lattice changes the charge transport properties of the semiconduc-

tor. This is triggered by several mechanisms. First, early studies have shown that the effects of the minority carrier lifetime τ after irradiation can be related to the particle fluence Φ by reducing the carrier lifetime [36]. The lifetime degradation is related to the electronic properties of the device especially for minority carrier devices.
The second mechanism that leads to damage in the semiconductor through displacement is the removal of charge carrier. Here, defects within the bandgap lead to traps for charge carriers changing the doping density. A large number of defects leads to a change in the Fermi level.
As a third effect the carrier mobility μ_0 decreases with an increasing number of defects as the impurities within the bandgap increase carrier scattering. The effects are grouped together as DD-effects and illustrate why semiconductor devices that require a long carrier lifetime are more susceptible to displacement effects and compound semiconductor devices are relatively resistant [12].

NIEL - non ionizing energy loss describes non-ionizing damage effects in materials per dose deposited in the material for a given particle type. It gives the fraction of energy deposited in the material by these interactions, but not necessarily their damaging effects [37]. Thus, *NIEL* and nuclear stopping power are the same quantity, in absence of nuclear reactions. The value can be calculated analytically using the differential cross section and including the kinematic scattering processes

$$NIEL = \frac{N_A}{A}[\sigma_e T_e + \sigma_i T_i] \tag{2.6}$$

with $\sigma_{e/i}$ the total elastic and inelastic cross section, $T_{e/i}$ the average effective recoil energies for elastic and inelastic reaction (corrected for the ionization loss), N_A the Avogadro's number and A the gram atomic weight of the target material [34].

Single Event Effects

The short term current produced by the ionizing track of a single charged particle passing through a semiconductor or insulator can harm a device irreversibly, and may be caused by neutrons, protons or ions. The necessity of only one incoming particle leads to the fact that so called Single Event Effects (SEE) already become important at much lower fluence than ionizing or displacement effects and the probability of the SEE is statistically distributed. By specification, a SEE occurs when a single particle (or its secondary products) introduces so much charge into the device that its function is temporarily or permanently disrupted or a continuation of the function becomes impossible.

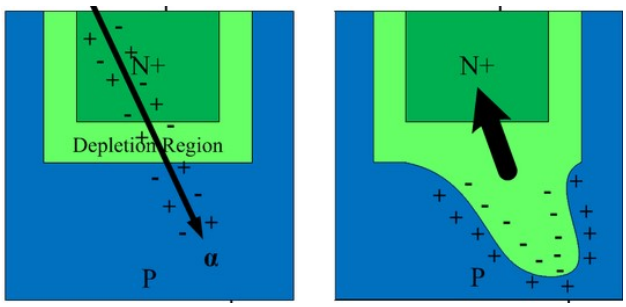

Fig. 2.6.: Influence of a single particle on the E-fields in a semiconductor [29]

A charged particle creates a track of electron-hole pairs when entering or passing through matter, which spreads outwards from the passageway. In this excitation process a shower of secondary electrons is produced which can have an average path length of several lattice constants. The initial track of electron-hole pairs is about $0.1\,\mu m$ in diameter but spreads laterally with the time. The track diameter increases about $1\,\mu m$ in about $1\,ns$ leaving a high density of electron-hole pairs. The amount of charge density created is proportional to the linear energy transfer of a particle. This large charge carrier density acts on the electric field by changing or collapsing it as indicated in figure 2.6 for an alpha particle traversing a p-n junction [12].
Most sensitive areas for SEE in a device are defined by the cross sections while the breakdown mechanism differs depending on the device type and materials.
The other process, playing a dominant role in SEE on semiconductor devices, is the nuclear interaction of the incoming particle with a crystal or isolator atom of the devices structure. The cross section for nuclear reactions in the crystal is about five orders of magnitude smaller than those of the other effects mentioned, but the secondary products also contribute to the ionization process and interact further within the device. The secondary products themselves have less energy and shorter path length but can have a larger energy transfer than the initial particle and interact with greater probability with the electrons in the lattice.
A distinction is made between reversible and destructive effects on a device. Reversible effects include upsets (SEU) and functional interrupt (SEFI). The main mechanism for destructive failure through SEE is well studied in Si devices but only recently under close investigation for compound semiconductor devices. Most important for high power transistors are gate rupture (SEGR) and burnout (SEB) of the devices.

Single Event Gate Rupture (SEGR) happens in Si MOSFETs due to particle interaction with the gate oxide in connection with charge generation in the epitaxial layer [38]. When a heavy ion crosses the gate oxide it temporarily reduces the electric field and depletion zone collapses due to the electron-hole pairs generated in the epitaxial layer by the ion track. This has the effect of applying a greater proportion of the drain voltage to the gate oxide, leading to a breakdown of the gate oxide. Despite many studies, the exact mechanism remains unclear [15].
Studies showed that Si MOSFETs are most vulnerable for SEGR while in blocking state. The damage depends on the ion energy, the penetration range, location of the strike, application angle and the drain source voltage.

Single event burnout (SEB) is a short-circuiting of the device followed by irreversible damage to the devices structure. The electric field in the MOSFET epilayer is redistributed by the impact of an ion, peaking around the epi/substrate interface and the body/drain junction. The introduced ionization at the epi/substrate interface is sufficient to start avalanching. In Si MOSFETs a single-ion induces conditions that cause a localized high-current state, which can trigger an inherent bipolar transistor structure due to the npn or pnp layers causing carrier avalanching through the epilayer. This current is maintained by band to band tunneling and as the temperature rises, microscopic melting points in the silicon occur. Permanent damage may be avoided by quenching, but after the silicon melts the device is irreversibly damaged [39]. The deposited power density increases with increasing LET and depends on the device bias. Recent publications suggest that a single event burnout in a SiC device, MOSFET or diode, is a more catastrophic form of degeneration, triggered by a rapid high energy distribution in a local area. [15]
Si MOSFETs are most vulnerable at high blocking voltages (high electronic fields) and n-type MOSFETs seem to be more susceptible because of the higher mobility of electrons compared to holes. The gate bias seems to have no effect on the susceptibility.
Studies on SiC MOSFETs showed that they are nearly as vulnerable as Si MOSFETs for SEB and also showed degeneration effects. Although it was initially assumed that the switching on of the parasitic transistor also leads to burnout in SiC MOSFETs, more recent investigations show that other mechanisms underlie within this technology which resemble the SEB principle in SiC diodes [40].

2.3. Gallium Nitride for Power Devices

In recent years, more and more power transistors made of wide bandgap semiconductor materials like silicon carbide and gallium nitride have come onto the market. Especially gallium nitride devices which have been in use for high-frequency applications with lower voltages for some time already, but lateral transistor structures for above $1900\,V$ have since been presented [41] and high-power transistors above $500\,V$ are increasingly being used.

Gallium nitride has many benefits for semiconductor construction. It is classified as a wide bandgap semiconductor with a bandgap of $3.4\,eV$ and GaN has therefore a high temperature semiconductor resistance of higher than 300 °C. With a breakdown field of $3.3\,\frac{MV}{cm}$ for a $1\,\mu m$ thickness a GaN layer theoretically withstands $330\,V$ [42]. Table 2.3 gives an overview of the different material properties in comparison to the traditionally used silicon (Si) and the second big wide bandgap material SiC. The most used semiconductor, silicon, in comparison has only a breakdown field of only $0.3\,\frac{MV}{cm}$ for a $1\,\mu m$ layer and resists only about $30\,V$. While Si is limited to lower voltages, SiC can handle much higher electric fields but only lower frequencies (up to $4\,GHz$) than GaN due to its lower mobility.

Nonetheless, one of the challenges for the production of GaN power transistors is the difficulty to produce sufficiently pure wafers and large enough crystals. Today most of the GaN crystals are grown on sapphire, but also silicon and silicon carbide substrates are used. In comparison, GaN grown on Si or SiC has 10^8 to $10^9/cm^2$ defects, whereas a Si device has on average only $10^4/cm^2$ defects. An increased number of defects leads to a faster degeneration and thus to a shorter lifetime of the component. Due to the high thermal conductivity, silicon carbide is the most suitable, but also the most expensive possible substrate for GaN power devices.

GaN belongs to the group III-V crystals that shape in a wurtzite structure, closely packed bilayers of metal and nitrogen atoms with a lattice constant of $a = 3.189$ Å and $c = 5.185$ Å. Forming two sub-lattices which can either have a metal-face polarity or a nitrogen face polarity depending on the growth direction which leads to a strong charge transfer between the very electronegative nitrogen atoms and the less electronegative metal atoms.

The crystal is a direct bandgap semiconductor with the conduction bands minimum located directly above the valence band maximum (figure 2.7). The bandgap energies varies with temperature [43]

Permanent spontaneous polarization P_{SP} in the crystal comes from to the polarity of the wurtzite structure and the other half from deviations from the ideal crystal. If the crystal surface consists of Gallium this corresponds to a +c polarization, for Nitride a -c polarization along the c axis, so the choice of growth gives the polarization along, or against the Surface of the substrate. The common $\frac{c}{a}$ ratio shows increasingly lower values for GaN compared to

Tab. 2.3.: Overview over the material parameters [12, 20].

Technology on:	**Si**	**SiC**	**GaN**
E_g $[eV]$	1.1	3.26	3.4
E_{br} $[10^6\,V/cm]$	0.3	2.0	3.3
μ $[cm^2/Vs]$	1350	700	2000
T_D $[eV]$	12.9	21.3	19.5
ρ $[g/cm^3]$	2.33	3.21	6.15

E_g Bandgap energy, E_{br} Breakdown field, μ electron mobility, T_D Displacement threshold energy, ρ Density

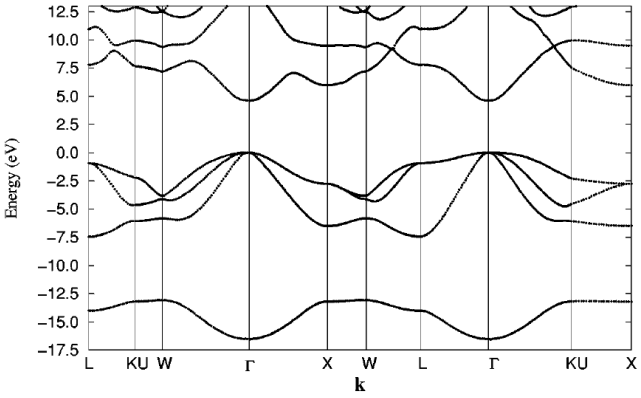

Fig. 2.7.: Band structure of a GaN crystal [44].

the ideal wurtzite [45]. This spontaneous polarization of the crystal structure evolves into the design of a HEMT.

2.3.1. High Electron Mobility Transistors

Despite the design also being possible for GaAs, then called modulation-doped Field-Effect Transistors, due to the subject of this work only the $AlGaN/GaN$ type will be further discussed.

To achieve good electrical properties the heterostructure is the essential part for providing the active region, based on the assembly of two materials with different bandgaps brought into contact, minimizing the scattering effect due to the absence of doping ions for higher carrier mobility. For GaN high electron mobility transistors (HEMT) this is an $AlGaN$ layer brought into contact with a GaN layer thereby forming a 2-dimensional electron gas at the boundary layer.

At the typical $AlGaN/GaN$-heterostructure the about 2.5% lattice mismatch between $AlGaN$ and GaN leads to a strain along the hexagonal c axis of the crystal and to deformation of the crystal causing a piezoelectric polarization P_{PZ} additional to the existing polarization of the crystal (see 2.3) [46]. Due to the tensile strain of the crystal the piezoelectric polarization is negative, meaning parallel to the spontaneous polarization and contrary to the electric field. In figure 2.8b the summation of the electric charge is shown with arrows while the $AlGaN$ and GaN layers are brought into contact (left to right). The total polarization of the crystal is the sum of both parts.

The lattice difference between the $AlGaN$ and GaN layer inducing positive charges change in polarization of the $AlGaN/GaN$-interface. While the accumulation of electrons from the polarization charge introduces a negative surface and leads to band bending [47], the induced

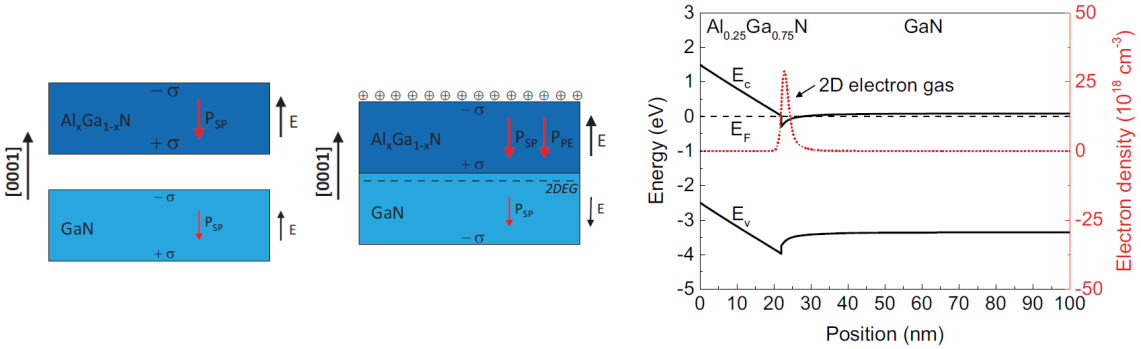

(a) AlGaN-GaN layers getting in contact **(b)** Bandstructure of the AlGaN-GaN interface

Fig. 2.8.: (a) Piezoelectric effect when contacting the different heterojunction layers. (b) Band structure of the $AlGaN/GaN$ heterojunction forming $2DEG$ [45].

positive charges at the surface are compensated by free electrons collected at the interface [46]. The induced piezoelectric surface charge density at the heterojunction is dense enough to form a triangle shaped potential well below Fermi level (2.8a) even without the need for a electron-supplying layer. Only two quantum states in this potential can be occupied so that the charge carrier within the GaN layer forms a two-dimensional electron gas ($2DEG$) [12]. Since the surface of the AlGaN layer contracts due to the lattice mismatch, negative polarization results at the surface and positive ions can accumulate. Therefore, a passivation layer above the AlGaN layer is necessary, for example made of SiN.

Important for the conductivity of the device is the field dependent mobility μ that can realistically reach values between $1600-1800\ \frac{cm^2}{V\,s}$ [48, 49]. It was shown that the electrons can have a high mobility of more than $2000\ \frac{cm^2}{V\,s}$ [48], resulting in a current density of up to $1\ \frac{A}{mm}$ and a very low resistance about $25\,m\Omega$ for $650\,V$ and $60\,A$. This results in significantly smaller loss and thus higher efficiency than with comparable components made of silicon [42]. The real carrier mobility however, is limited on one hand by temperature-dependent conditions, such as acoustic and polar optical phonon scattering and on the other hand by scattering at crystal properties like interface roughness, charged surface states through ionized impurities, impurity atoms, dislocations and alloy scattering [48].

Other possible heterostructures with gallium nitride exist, even so, AlGaN is the most common. GaN HEMTs can exhibit current collapse when operating at high voltages. One way to reduce gate collapse is to add a field plate over the gate (drain sided).

2.3.2. Technology for Normally-off GaN HEMT Devices

The components built as described above have the disadvantage of being normally-on devices. Without applied gate voltage the devices are forward biased, which means they conduct current at $v_{GS} = 0$. For most of the power applications it is necessary that the devices do not conduct when the circuit fails for safety reasons. Thus far, different approaches have been described to build a normally-off device from the normally-on component design [42].

(i) The injection of (Fluoride-) ions under the gate region [50]. This leads to a depletion of the channel region and thus to a positive threshold voltage. The main disadvantage of this technology is that it is unstable under electrical stress which leads to a shift of the threshold voltage and a higher drain leakage current.

(ii) An MIS-type gate stack [51] that minimizes the gate leakage. Through the gate stack the threshold voltages is raised above $1\,V$, but because of traps in between the boundary layer and the isolator, v_{th} is very instable and vulnerable to time dependent dielectric breakdown.

(iii) A cascode-structure with a high voltage normally-on GaN HEMT that holds the circuit voltage and a low voltage Si MOSFET that turns the circuit on or off in one package with the necessary relationship of

$$V_{DS(mx)}(Si - MOSFET) > |V_{th}(GaNHEMT)|$$

Advantages of this technology are a very stable threshold voltage, the use of normal Si-drivers and normally-on HEMTs are inexpensive and reliable. The complexity may count as a disadvantage [52].

(iv) The use of a p-type GaN or AlGaN layer in between the gate and the AlGaN barrier layer, as shown in figure 2.9, is the wide consensus for creating normally-off GaN HEMTs. This works like a PiN-diode by lifting the band diagram and leads to a complete depletion of the two-dimensional electron gas under the gate structure at a voltage of $V_{Gs} = 0\,V$ and thus shifts the threshold voltage $v_{th} > 0\,V$ [42, 53].

The threshold voltage shifts mainly dependent on the doping concentration of the p-layer, often using magnesium as the dopant. Ohmic-gate metal or Schottky-gates are possible over the p-layer.

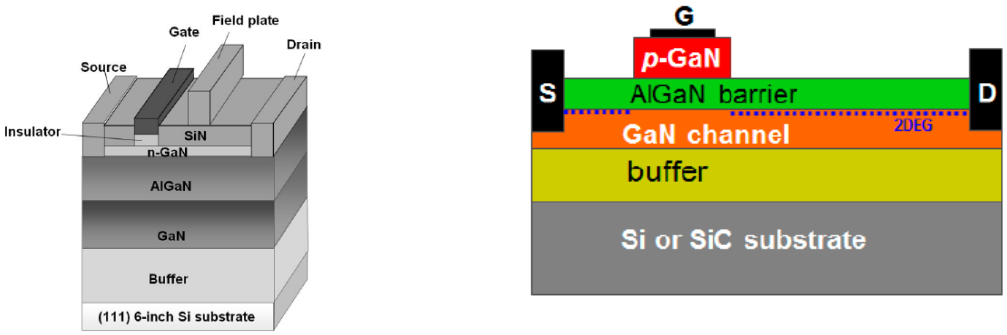

(a) MIS-HEMT structure **(b)** p-GaN Gate structure

Fig. 2.9.: Schematic structure of normally-off GaN High Electron Mobility Transistors. (a) MIS-HEMT structure [52] (b) p-GaN Gate structure [42].

Nevertheless, the known degenerative possibilities of a p-GaN gate are to be considered. For positive threshold voltages and positive gate voltages ($v_{th} > 4\,V$ and $v_G > 0\,V$), thus the device in ON-state, carrier trapping under the gate region has been reported. With the threshold voltage positive, holes are injected from the metal to the p-GaN layer and accumulate at the $p-GaN/AlGaN$ interface, leading to a temporary increase in the $2DEG$-density and shifting the threshold voltage negatively.
GaN-based MIS-HEMTs also show a positive threshold instability when operated with positive bias because of electron trapping in the insulator/AlGaN stack. [42]
With a high drain voltage bias during OFF-state operation punch-through breakdowns were seen. A non-optimal wafer production may enhance defects and a leakage within the passivation layer and a punch-through if the drain bias V_{DS} is high enough meaning the current flow within the GaN layer bulk, leading to the device breakdown [54]

2.3.3. Radiation Effects in Gallium nitride-HEMTs

Ionizing Effects in GaN HEMTs

Due to the lateral structure of the high electron mobility transistors and the missing dielectric beneath the gate, insensitivity to ionizing effects is expected. Indeed, radiation up to $1\,Mrad$ with ^{60}Co showed no significant TID effect such as a shift in drain and gate current (I_D, I_G), on-resistance (R_{on}) or the threshold voltage (V_{th}). All devices worked within their specifications after the radiation tests. Minor shifts of the threshold voltage were observed after the radiation, also at low dose rate testing with $10\,\frac{mRad(Si)}{sec}$ [21].
Compared to the tests performed by [17], the sensitivity seems to depend on the gate design. It appears that the Schottky-gate design responds to irradiation with a shift of threshold voltage V_{th}. The p-gate design seems to be more sensitive to low dose irradiation than other gate designs.
Calculated *NIEL* and *TID* rates for proton irradiation in GaN can be found in table 2.4

Displacement Damage in GaN HEMTs

The sensitivity of a crystal lattice for displacement damage depends significantly on the displacement energy of the crystal and therefore directly on the bonding strength of the crystalline elements. The larger T_D is, the more resistant the crystal becomes to radiation. To dislodge an atom from a GaN lattice the energy needed ($E_d(Ga) = 20.5\,eV$ and $E_d(N) = 10.8\,eV$) is significantly higher than for a silicon crystal [56]. It can also be observed that the degeneration of the GaN crystal first starts at two magnitudes higher fluence than in GaAs crystals due to the stronger bonding.
For heterostructures which specifically utilize the purity of the crystals, the most important effect is carrier removal in different regions of the structure (compare the section about displacement damage in 2.2.3), especially in the active region like the $2DEG$.
Irradiation of a GaN crystal with ions like p, C, or O showed no critical effects to the crystalline properties but irradiation with heavier ions like Fe lead to changes in the lattice

Tab. 2.4.: Calculated ionizing, non-ionizing energy losses and total ionizing dose for 10^{13} protons/cm^2 in GaN [34, 55]

Energy	**loss**	**2 MeV p**	**40 MeV p**	**100 MeV p**
IEL	$[\frac{keV}{ion}]$	105	12	6
NIEL	$[\frac{eV}{ion}]$	3	0.1	0.05
TID	[rad]	10^7	1.6×10^6	8×10^5

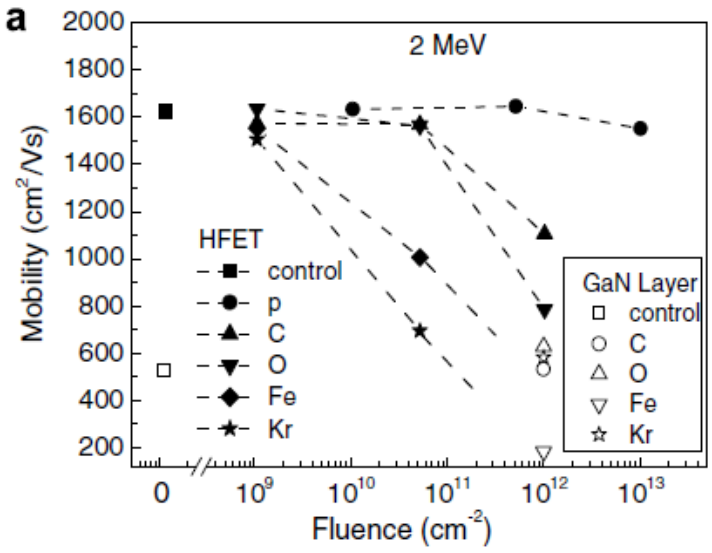

Fig. 2.10.: Carrier mobility decrease after irradiation with different ions in an GaN HFET transistor [57].

and the lattice-constant [57], [58]. In the same experiment not only a GaN crystal but also GaN HEMT structures were irradiated and probed afterwards. Like in the crystal, increasing ion mass leads to rising displacement damage and degrading of the drain current I_D. The drain current was lowered by 30% after radiation with Fe-ions and even 45% with Kr-ions as can be seen in Figure 2.10.

Often a change of the threshold voltage v_{th} can be observed. A shift to more positive values caused by negative charged traps in the AlGaN barrier or the GaN buffer and negative shifts caused by an increase of positive charge in the barrier region [34].

Although there is a basic qualitative understanding of the functional dependence of displacement effect damage, there are still large shortcomings in the complete understanding of radiation-induced defects in the micro structure of GaN. Also, how exactly the type of radiation affects the formation and stability of these micro structure defects remains to be investigated. The type of defect or traps formed by irradiation seems to depend significantly on the type and distribution of initial defects within the crystal.

Also, for GaN components, annealing effects were seen after irradiation, so that part of the device properties could recover. Electron traps in N-centers were healed at $800° C$ and deep traps in the gallium lattice even at room temperature. Larger doses or irradiation with neutrons led to more stable defects [34].

Single Event Effects in GaN HEMTs

It is important to note that GaN HEMTs data on single event effects is still very limited and most was measured on high frequency devices or power devices up to $300\,V$. As GaN HEMTs have no gate oxide, the classic failure mechanism gate rupture (SEGR), damage of the gate oxide, cannot occur. The lack of p-n junctions prevents the occurrence of parasitic transistors and thereby avalanche breakdowns. Operating under high frequency, a catastrophic failure has not been reported in the published literature so far, but under DC bias Single Event Burnouts were observed. Early tests of normally-off commercial GaN devices showed a wide variability in the test's outcome [16, 17, 18, 21, 56] which may be related to the difficulties in production of sufficiently pure wafers. Testing of high-reliability devices with heavy ions showed the worst beam angle is perpendicular to the surface and the Bragg peak targeted near the $2DEG$ [21]. Contrary to that testing of commercial $600\,V$ GaN HEMTs suggests a strong angle dependence of the incoming beam and also significant part to part variations [17, 18]. Particularly noteworthy is that after irradiation of the same device type the seen shifts in the threshold voltage V_{th} were measured both in positive, as well as in negative direction, but the most DUTs continued working (though out of specification) [18].
Further unreviewed results from this year, indicate that not only the sensitive volume around the gate region has an influence on the failure rate, but also the rotation of the device. The results of the experiments verified that SEE were observed under constant blocking voltage, but not under switching conditions. The angle of ion entry also had a significant influence. With an entry angle parallel to the two-dimensional electron gas channel, the necessary drain voltage V_{DS} for a SEE was reduced by up to 50 % in one of the outcomes [59]. The minimum fail voltage improves by at least 15% at a beam angle parallel to the gate-drain fingers, and decreases by approx. 25 % at a beam angle parallel to the electron gas channel [60]. The path length through the conduction channel is shorter for a particle arriving perpendicularly than for a particle arriving at an angle similar to parallel, allowing more energy to be deposited in the volume along this path length.
SEE sensitivity in Si and SiC devices are known to be dependent on the bias condition, the LET of the incoming particle, the angle of the incident particle and the target region within the devices. Experiments to date do not provide a fully clear picture of these influencing factors in GaN HEMTs but in recent years a general trend emerged:

(i) The SEE susceptibility is larger for higher voltage rated devices.

(ii) Further it indicates that the worst possible biasing for SEE is with DC blocking voltage applied, as no failure while high frequency-operating occurred, contrary to under operation with DC-voltage.

(iii) The occurrence of SEE is dependent on the LET, but ion species and penetration range play little to no role [61]. The voltage at which SEE occur decreases with increasing LET of the incoming particles, this might have to do with interactions in the $2DEG$ channel region.

Nevertheless, prior studies estimate the gate region of the GaN HEMTs is particularly sensitive to irradiation [17]. Despite there being no gate oxide, which could interfere directly with the incoming particles, the high local electric fields near the gate drain edge seem to be especially liable for SEE [62, 16].
An incoming particle traversing the drift region creates a large number of electron hole pairs, momentarily short circuiting the device. The minimum energy required for the electron-hole creation in gallium nitride is $7.8\,eV$, twice as high as the energy required in silicon. As a result, fewer electron-hole pairs are induced by a transient particle in the material. If the charges could be discharged quickly enough this would be only a nondestructive short circuit (SEU) or transient (SET) and a reset of the device possible. As the $2DEG$ channel provides electrons with a high mobility they get carried away quickly, but the holes cannot be conducted in large numbers and fast enough so that the short circuit leads to an irreversible burn out (SEB) of the devices structure.

3. Methodology

The majority of electronic components have an inherently low failure rate and continued function for years. For device manufacturers it is common practice to perform periodic reliability evaluations on their components but that means they would need to measure effects in the order of magnitude of one failure in 1200 years.
At the beginning of the investigation on cosmic ray induced failures in the 1980s and 1990s, components were brought, for example, to the high altitude research station at the Jungfraujoch (Grindelwald, Switzerland) at 3580m above sea level for accelerated tests.
With altitude, the number of cosmic particles increases, so that at the Jungfraujoch the radiation is higher than at sea level by a factor of ten [7]. Nevertheless, the reliability tests took months or years, which is an impractical time frame for system and device developments.
This tremendously long amount of time makes it necessary to perform reliability tests in an accelerated manner and under stress conditions to test reliability and operability under radiation conditions. The tools of choice today are tests at proton or neutron particle accelerators with higher particle flux which significantly reduce the time needed for tests.
With the passage of time, different testing parameters and methods have been developed to test for special radiation environments. These parameters and properties will be presented in the following subchapter, together with the standard to which the experiments for this work were adapted to investigate the relatively new *normally-off GaN HEMTs* for their radiation sensitivity mainly to terrestrial radiation, but some measurements also use heavy ions.
In the further subchapters follows a presentation of the experimental idea and the used setup and equipment for the measurements.

3.1. Parameters of SEE-Testing and Definitions

Although sample testing and the related statistical models are widely used, the validity of the results depends on how well the assumed failure function matches the actual function of the initial population and any assumptions about the acceleration factors. In the following, the most important parameters for single event effect measurements in electronic power devices are defined. These include the distribution functions applied, the descriptive factors of the particle beam, such as fluence, flux, the effective cross-section and reliability as well as the linear energy transfer.

3.1.1. Fluence, Particle Flux and Failure Rate

The fluence Φ is the total particle number per cross section area or particle flux integrated over time

$$\Phi = \frac{dN}{da} \qquad [\frac{particles}{cm^2}] \tag{3.1}$$

from the irradiation facilities normally given is the flux

$$\dot{\Phi} = \frac{d\Phi}{dt} \qquad [\frac{particles}{s\,cm^2}] \tag{3.2}$$

Under the term reliability the fraction of surviving devices (of a population) after a time t is given

$$R(t) \; = \; \frac{N_{surv}}{N_{initial}} \tag{3.3}$$

and therefore, number of failed devices

$$F(t) \; = \; 1 - R(t) \tag{3.4}$$

and the failure density function $f(t)$ is the derivative of $F(t)$. Although the derivative to f(t) is possible by various functions, previous work on reliability is best described by the log-normal function. [12].
Related to these dependencies is the failure rate $\lambda(t)$

$$\lambda(t) \; = \; \frac{f(t)}{R(t)} \tag{3.5}$$

Cross Section

The principle of cross section for single event effects is based on the cross section concept used in nuclear physics to describe the probability of nuclear reactions as a function of the incident energy [63]. But it does not correspond to it.
For the cross section used here, there are two processes: ionization in the semiconductor caused by nuclear reactions (protons and neutrons) and direct ionization along the particle track. Only the second process is directly angle-dependent, since the change in path length within the device leads to a different ionization. The probability of such an interaction is given by the interaction coefficient called cross section [64]. For a target entity and for a given interaction and a given energy, the cross section is given by

$$\sigma = \frac{N}{\Phi} \qquad [cm^2] \tag{3.6}$$

where N is the mean number per target entity of this special interaction and Φ the particle fluence.

3.1.2. Linear Energy Transfer

The Linear Energy Transfer (LET) is a quantity to give the energy loss and, with that the energy transfer from an incident particle to a given material via ionization. This is formulated in the *Bethe-Bloch* formula which gives the range in material as a function of initial energy as specific energy loss,

$$S = -\frac{dE}{dX} = \frac{4\pi e^4 z^2}{m_0 v^2} NB \tag{3.7}$$

with v and ez the velocity and charge of the initial particle, N and Z are the number density, shown in figure 2.3 for some particles in Si. According to this the Bragg curve gives the energy loss per distance [22]:

$$B = Z\,[ln(\frac{2m_0v^2}{I}) - ln(1 - \frac{v^2}{c^2}) - \frac{v^2}{c^2}]$$

For semiconductor reliability the energy transfer is often given for silicon properties $LET(Si)$ $[MeV\frac{cm^2}{mg}]$@*surface*.
Neutrons have no, and protons only a small direct contribution to ionization in material. Both particle types interact through collisions or nuclear reactions with the material and the excited secondary particles contribute significantly to the ionization. For example, an incoming $100\,MeV$ proton has an LET of only $LET_p(100\,MeV) \approx 0.0006\,MeV\frac{cm^2}{mg}$, but

Tab. 3.1.: Comparison of calculated LET in Si and GaN (LETs in $[MeV\frac{cm^2}{mg}]$). The ion values were calculated and communicated by the Facility.

Particle	**LET(Si)**	**LET(GaN)**	**Ratio**
$n\,(atmos.)$	$12^{\star}$	$10.6^{\star}$	0.89
$p\,(200\,MeV)$	$16^{\diamond}$	$13^{\diamond}$	0.81
$Xe\,(43.76\,MeV/n)$	27.79	23.5	0.85
$Xe\,(17.8\,MeV/n)$	44.46	35.6	0.80
$Pb\,(\,MeV/n)$	7.98	7.1	0.88

$\star$) Maximum LET of the secondary products produced due atmospheric like neutron distribution range between $0.01 - 12\,MeV\,\frac{cm^2}{mg}$ in Si [68, 20]

$\diamond$) Calculation of the maximum recoil LET from $200\,MeV$ protons found to be about $14\,MeV\,\frac{cm^2}{mg}$ in Si and $13\,MeV\,\frac{cm^2}{mg}$ in GaN [65].

the maximum recoil products of $LET(recoil) \approx 14\,MeV\frac{cm^2}{mg}$ in silicon [65].

In table 3.1 the linear energy transfers for different particles and energies in silicon and gallium nitride and their ratios are given. The LET-values in silicon for Xe- and Pb-ions were given by the facilities *GANIL* and *CERN*, the calculation of the effective LET for neutrons and protons is from [66] and [65]. The values of the LET in GaN were calculated with SRIM (SRIM-2013.00 [67]) according to the given beam values from the facilities, and the results shown in the figure 3.1

3.1.3. Distribution Functions

For the occurrence of a single event effect, the time and the previously received radiation dose do not play a role. The probability is constant over the time of irradiation therefore it is called a constant hazard rate.

As independent processes, single event effects can be described by a poison process.

Thereby the Poison distribution

$$P(X = x) = \frac{\lambda^x}{x!} \cdot e^{-\lambda} \tag{3.8}$$

describes the distribution of rarely occurring events with a constant probability distribution function

$$p = 1 - e^{-\lambda t} \tag{3.9}$$

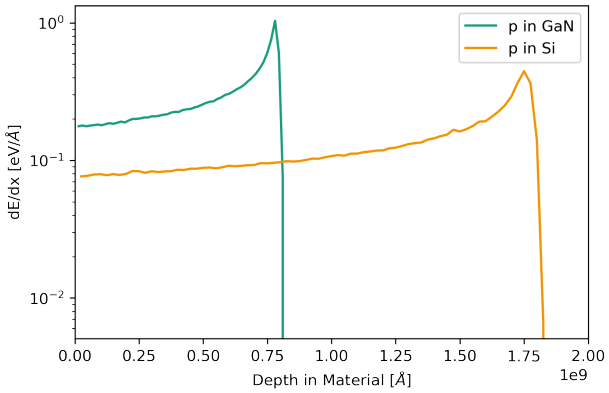

(a) 230 MeV protons

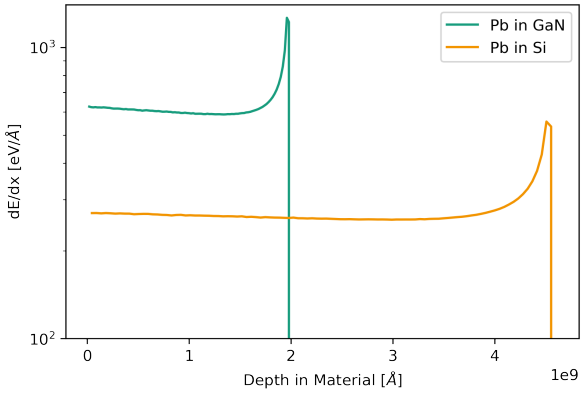

(b) 6 GeV/n Pb-ions

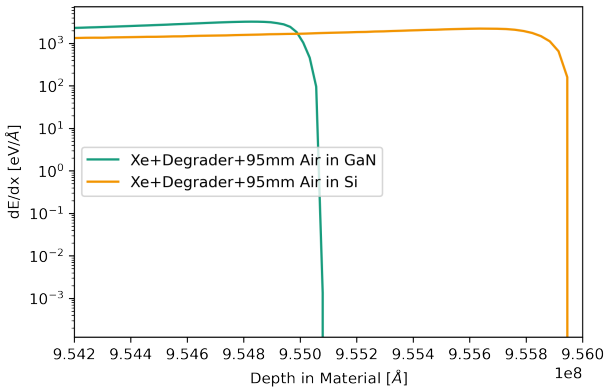

(c) 49.2 MeV/n Xe-ions with degrader + air gap

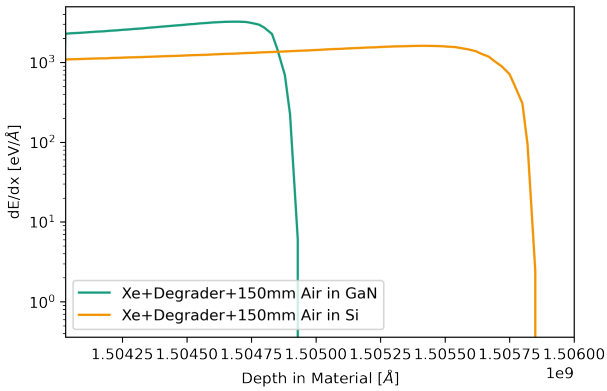

(d) 49.2 MeV/n Xe-ions with air gap

Fig. 3.1.: Plot of the calculated [67] direct ionization in GaN (green) and Si (orange) for different ions. For Xe-ions, the DUT starts at $9.54 \cdot 10^8$ Å (c) and $1.54 \cdot 10^9$ Å (d).

Cross Section Distributions

To describe the dependence of the sensitivity on the deposited energy, the cross section is analyzed against the LET of the incoming particle. This gives, as an integral curve, the relative fraction of the device which will fail at an energy greater than or equal to the threshold energy (LET_{th}).

Ideally, the process is described by a step function which jumps to the maximum cross section when the LET_{th} is reached, but in reality, a curve is measured which increases from the threshold and saturates to the maximum cross section. Both the exponential function and the log-normal function were used to describe single event upset data [69]. The exponential function is used in the following form

$$f(LET) = \sigma_0 \, e^{-k/(LET - LET_{th})} \tag{3.10}$$

also without a threshold value [70].

The approach that the single event effect is caused by a charge collection process in the transistor leads to the mathematical description using a log-normal distribution [71]. The normal distribution is used with the logarithm on the LET. With

$$z = \frac{ln(LET) - m}{\sqrt{2}\sigma}$$

and m = mean of the function ($ln(LET)$), σ the standard derivation, is the log-normal distribution

$$f(z) = \frac{1}{\sqrt{2\pi}\sigma} e^{z^2} \tag{3.11}$$

Another option is the use of a Weibull function, which depending on its four parameters, resembles a normal distribution or asymmetric distributions such as the exponential distribution. The distribution is named after the Swedish engineer and mathematician Waloddi Weibull:

$$F(LET) = \sigma_{sat} \left[1 - e^{-(\frac{LET - LET_{th}}{W})^S}\right] \tag{3.12}$$

with σ_{sat} the saturation cross section, LET_{th} the threshold LET at which SEE occurs, W as width parameter and S as shape parameter.

3.2. Testing Procedure

In order to determine the sensitivity of semiconductor devices to single event effects induced by radiation, it is necessary to be able to test the devices comprehensively and in a reasonable amount of time.
Depending on the radiation environment, for which the component should to be tested, there are several ways to implement such a test. One way to attain this is to parallel measurements and test many devices at once or to increase the particle flux on the device, using particle accelerators. Thereby, the particle type and its energy are the controllable factors.
Assumptions must be made about the predictive power of such a test, due to the limited possibilities for radiation ions and energies, since the radiation generated only gives a limited picture of the actual radiation environments.

3.2.1. Accelerated Tests with Radiation Sources

In order to be able to perform earthbound accelerated tests, especially if the devices are later to be used in space, monoenergetic, strongly accelerated heavy ions are used and the necessary charge transfer is ensured by using ions with a corresponding LET [72].
The various types of heavy ions can map a broad LET spectrum with the aid of individual energies. The Bragg peak should end in or, if not otherwise available the LET should be constant over the sensitive volume of the device. Table 3.1 shows relevant ion types and energies for this work as well as their LET in Si and GaN. It can be seen that heavier ions and higher energies lead to a smaller LET, but the smaller LET means a little change of energy transfer over the volume of a device.
The worst case particle condition for a semiconductor device is that, which deposits the most energy in the sensitive volume of the device. For all tests, in GaN or Si, it is therefore recommended to choose the particle energy in such a way that the particles can penetrate into the substrate, so that the LET varies little over the possible sensitive volume [61].
The maximum energy transfer occurs in the peak of the Bragg peak, which should therefore be in or near the sensitive volume. For silicon power MOSFETs a rough calculation of the layer thicknesses required to maintain the electric field gives a guide value for needed ion range of $150 - 300\,\mu m$ for Si MOSFETs rated $400 - 1000\,V$ [73]. As a result, a minimum energy is required for SEB testing to avoid underestimation of SEB. However, these values cannot simply be transferred to GaN HEMTs, which can withstand much larger fields due to the wider bandgap and can have much thinner layer thicknesses or even other building structures so that relatively low energy particles are able to fully penetrate the thin layers.

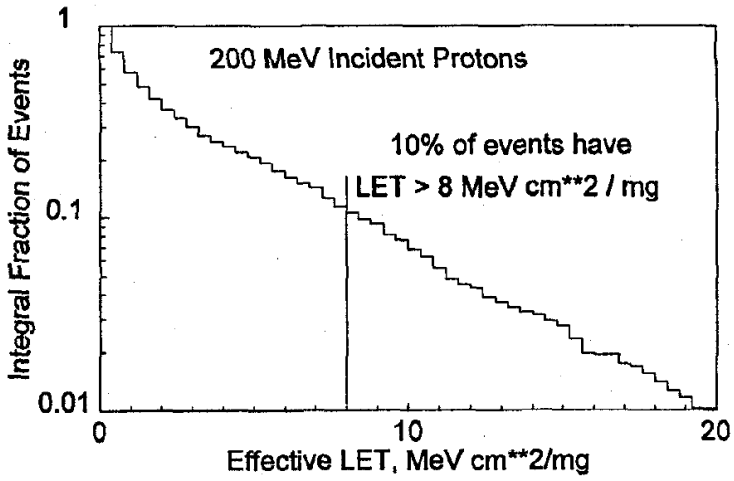

Fig. 3.2.: LET of the secondary products produced through proton interactions with silicon [79]

It should also be noted, that in general, the particles selected for irradiation with ions must not be shielded beforehand by the device package or other structures in the beam like the experiment board. In some cases, such as low energy heavy ion beams, it is necessary to decapsulate the device beforehand.

For terrestrial device applications, neutron irradiation is the most relevant. The natural neutron spectrum has a continuous energy up to GeV, but also slow neutrons (thermal up to $10\,MeV$) contribute to the single event cross sections and have the highest number in the spectrum (compare right part of figure 2.2). In order to cover this broad spectrum as good as possible, the preferred method is testing at a spallation neutron source. There are only a few spallation sources distributed around the world, such as the Los Alamos/WNR facility [74], the Tri-University Meson facility (TRIUMF) [75] or the ISIS neutron source [76], where the first can offer a maximum energy of $800\,MeV$ and no thermal neutrons, the second, a fraction of thermal neutrons but an upper energy of $500\,MeV$, and the last, one which is specified up to 0-$800\,MeV$ (see section 4.3.1 in the next chapter) [77, 76]. And the Research Center for Nuclear Physics (RCNP) of Osaka University [78] with 1-$300\,MeV$ neutrons.

As an alternative, monoenergetic neutron beams can be used. Low energies can be obtained by fission or fusion (D-T/D-D reaction section 4.3.2 in the next chapter) sources, where the effective cross-section curve must then be integrated over the full spectrum [77].

Until recently, the Svedberg Laboratory (TSL) has also been able to provide monoenergetic neutron beams as well as spallation neutrons.

Monoenergetic proton beams of different energies are also often used to perform tests for space and Earth applications. These are common, easy to obtain with a high particle flux

and can give a good representation especially for terrestrial applications within certain limits. As with neutrons, the main contribution to see is through the secondary products produced, which are similar for high energies. At low energies, however, they diverge strongly due to different nuclear reactions and probabilities.
In figure 3.2, the LET-distribution of the secondary products produced by an incoming $200\,MeV$ proton in silicon is shown.
The largest number of secondary products have an LET below $8\,\frac{MeV\,cm^2}{mg}$, but can go up to $16\,\frac{MeV\,cm^2}{mg}$ for single secondary products in Si and up to $13\,\frac{MeV\,cm^2}{mg}$ in GaN [79, 65].
The natural spectrum in the cosmic environment consists of a broad distribution of ion species and energies. Consequently, the accelerators available on Earth are inadequate in the representation of the complete spectrum.

3.2.2. Standards

For accelerated reliability tests on radiation effects in semiconductors over the years, different procedures were developed. They differ by type of application but specifically in their use for space, avionic or terrestrial applications. However, the existing standards are for silicon devices and established for planar-gate vertical structures [15]. So far, these standards and experiences have been extrapolated for other materials and construction forms, and only a year ago a guideline for testing GaN RF-HEMTS for space applications was announced [80]. Special definitions for SEE-testing can be found among others in the *ESCC 25 100-2* [11], *MIL-STD 750-1* [81], *EIA JESD57A* [9] or *JEDEC-JEP151* [10]. Most of them relate to proton and heavy ion testing, especially for space and near Earth orbit applications, and will not be discussed in greater detail in this work.

One standard especially for Earth bound applications and high power Si devices is the *JEDEC - Test Procedure for Measurement of Terrestrial Cosmic Ray Induced Destructive Effects in Power Semiconductor Devices - JEP151* from Global Standards for the Microelectronics Industry.
For the SEE test it calls for a monoenergetic proton/neutron beam or a spallation neutron source of at least $150\,MeV$, with the spallation source being preferred. The spallation spectrum should represent the neutron spectrum of terrestrial cosmic radiation from $10\,MeV$ to maximum energy of the spectrum.
For device testing the beam energy, diameter and angular spread must be considered and the beam flux variation across the different devices (or the component surface) has to be $\pm\,10\,\%$ or less. To obtain meaningful data, a fluence of at least $10^4 - 10^8$ particles per cm^2 should be reached, a sufficient number of components must be irradiated and the devices should

perform an electrical characterization beforehand. Depending on the setting, this can be up to 50 components, but at least 10 device errors should be achieved.
During the measurements failure detection, fluence to fail (time), applied voltage, position within the setup or other stressors have to be recorded for each device individually. It is recommended to use ESD protection and only calibrated measuring equipment.
For proton irradiation, the interaction with package material and (Cu-)backplanes must be considered and the overall energy in the sensitive volume should not fall below $150\,MeV$. Therefore, it is advised to stack the devices only in a single plane to the beam side for proton irradiation. According to this standard, the irradiation with monoenergetic proton beams over $150\,MeV$, in general, overestimate the failure rate, due to the low energy portion of the natural spectrum, which it is missing [10].
The purpose of this work was also to develop a reproducible test setup and procedure. The requirements from the above-mentioned standards were used as a guideline. The identification of the components and repeatable of the irradiation position were considered important, as well as the current and voltage to be measured individually for each component. The requirements for the radiation source should also correspond to the requirement that the complete sensitive volume of a component could be hit.

3.3. Experimental Idea and Setup

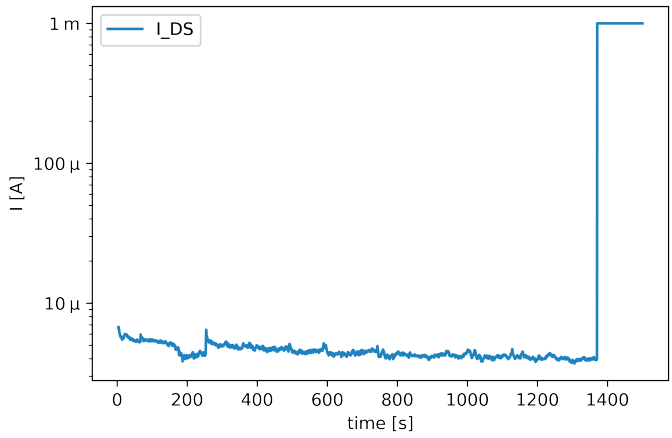

Fig. 3.3.: Example of a current waveform at an SEB event (this is the measured current waveform of the DUT 038 *Type A* at 850 V irradiated with the atmospheric like neutron spectrum.)

In order to get an overview of the SEE sensitivity of modern commercially available normally-off GaN HEMT power transistors and to possibly make a statement about the comparability of future measurements for terrestrial applications, different commercial device types were tested with several radiation sources.
Three normally-off GaN HEMTs device types with varying design and one comparable SiC MOSFET with 600 V operating voltage for high energy systems were bought and tested. The different devices are presented in detail in the next chapter under 4.1.
The typical signature of a SEE is a prompt and permanent rise in the drain (or/and gate) leakage current as shown exemplary in figure 3.3. To detect this effect, the currents and applied voltages at the selected devices are to be measured during the entire irradiation time looking for prompt current raises in the drain or and gate leakage current.
For this purpose, a DUT-board for device stacking and a relay-board were designed, which make it possible to control and measure each component individually. Depending on the beam diameter, between 3 and 27 components can be plugged onto the DUT board. For each component, there is a measurement circuit as shown in figure 3.5, which controls both gate and drain voltage (V_G and V_D) and continuously measures the leakage current between drain and source (I_{DS}) as well as the leakage current between gate and source (I_{GS}). A 1 $M\Omega$ resistor was inserted into the circuit to limit the leakage current in case of a component breakdown.
An additional relay board was used to control the selection of components for the experiment. The measured data from the selected DUTs were displayed and recorded.

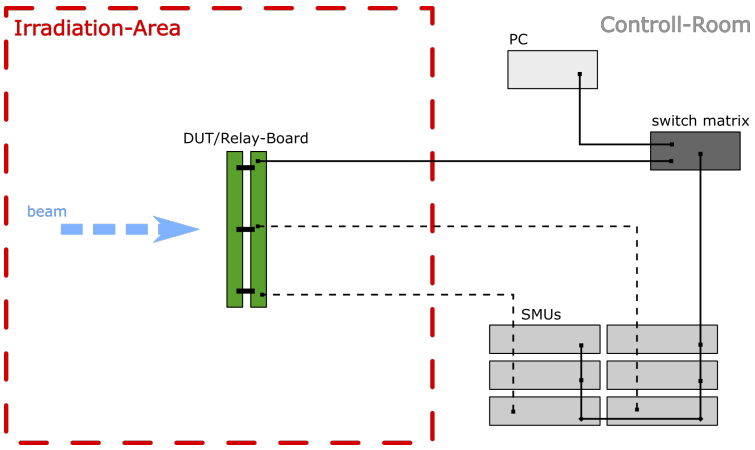

Fig. 3.4.: Graph of the general setup for the experimental measurements. The DUT holding board is stacked upon the relay board with the circuit. Both are located directly in the irradiation room, DUTs facing the beam. The control elements and power supplies are located outside the irradiation area and are controlled by a PC.

The DUT boards design varies from irradiation facility to radiation facility due to the different beam sizes but can hold at least 3 to 27 DUTs at a time. The average beam size was up to 9x9 cm^2, so that most of the time, 3 DUTs could be brought into the beam and measured simultaneously.

For the measurements, the devices were mounted on the DUT board and both the DUT board and the relay board were installed on a fixture that made it possible to move the entire board in x and y axes (in relation to the beam direction). At some of the facilities this was already provided, at others it was set up with the help of a micro-step-motor. The positioning of the board could be controlled from the control room, so that the components could be connected for the experiment, positioned in the beam window and then measured. After the completion of a run, the next components were selected via the relay board and positioned in the beam, reducing the need to open and enter the irradiation area. Figure 3.4 shows the layout of the general set up.

As the SEE error rate seems to be dependent on the drain stress and the stable applied blocking voltage seems to be the most vulnerable case for GaN HEMT power transistors [12, 15, 17], a permanent blocking voltage v_{DS} was applied and monitored during irradiation. To apply and measure v_{DS}, v_G, I_{DS} and I_G Source Measure Units (SMU) of the types *Keithley 2654A*, *Keithley 2410* and *Keithley 2400* were used and controlled by a personal computer using a Fraunhofer INT owned LabView program which displays and records the current data up to every microsecond. During the experiment the applied gate and drain voltage as well as the gate and drain leakage currents were monitored and recorded at least every millisecond during irradiation. The criteria for a single-event effect was defined as a

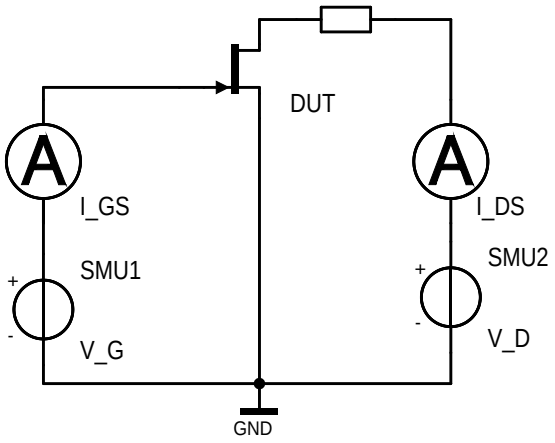

Fig. 3.5.: Measuring circuit diagram for the irradiation of the components.

sudden (less than one millisecond) increase in leakage current, as shown in figure 3.3. As compliance for the SEE detection $1\,mA$ was set. The occurring leakage current was limited to $1\,mA$ by a $1M\Omega$ resistance within the circuit. The DUT was then noted as failed and the measurement of this component was stopped.
Before irradiation, all components were soldered to sockets matching the irradiation board, serialized with numbers from 001 to 300 and tested for functionality to exclude previous damage and thereby effects on the results. Attention was paid to appropriate ESD protection, also during transport and mounting.
More detailed information to the set up regarding the different facilities and beams can be found in the next chapter under 4.2 and 4.3 for each measurement individually.
Since previous studies with $200\,V$ GaN HEMTs showed that most single event effects occurred above $10^6\ \frac{particle}{cm^2}$ [17, 61], the DUTs should be irradiated at least to $10^8\ \frac{particle}{cm^2}$ if no device breakdown occurs.

4. Measurements

This chapter describes the experiments performed. In the first part, the selected devices and their specifications are given. For this purpose, the device models were anonymized and assigned to the *Types A, B, C* and *D*.
In the rest of the chapter, the experiments and the facilities at which they took place are described. The division of the chapter is not based on the execution time of the experiments. First the ion-experiments are presented in more detail. This includes the measurements with Xenon-ions at the Grand Accélérateur National d'Ions Lourds *GANIL* (Caen, France), the Lead-ion measurements at CERN High energy AcceleRator Mixed field facility *CHARM* (Genf, Switzerland) and the measurements with protons at the National Center for Radiation Research in Oncology accelerator facility*OncoRay* (Dresden, Germany). Then, the experiments with neutrons at the ISIS Neutron and Muon Source (Oxfordshire, United Kingdom) and the monoenergetic neutrons at Fraunhofer INT (Euskirchen, Germany) are presented. The experiments took place in the following time periods: *GANIL* June 2018, *ISIS* September 2018, *CHARM* November 2018, *INT* December 2019/January 2020 and *OncoRay* September 2020.
The collected measurements and all data used for further analyses are provided in the appendix B

4.1. Device Under Test

The GaN HEMT technology with a normally-off condition already provided some commercial devices of the $600 - 650\,V$ class which demonstrate very low capacitance, gate charge and on-state resistance, which outperform Si-based MOSFETs [42]. Three such commercially available device types were chosen. All three devices have a lateral HEMT design, but three different approaches were used to accomplish the normally off state. In addition to the commercially available devices, $600\,V$ normally-off GaN HEMTs were provided for this work by the Ferdinand Braun Institute (Berlin). This is listed below under the name *FBH*. For these devices we were provided with the exact structure and layer thickness. Unfortunately, it was only possible to irradiate them with the atmospheric like neutron spectrum at ISIS, since the planned measurement, with single ions and micrometer resolution, could not take place due to the pandemic of 2020.
Table 4.2 lists the devices, their structural shape, the technology on which the normal-off state is based, the maximum rated drain voltage and the specified operating current. In addition, the last column for each component type indicates the experiments in which it was measured.
As described in chapter 3.3, all soldered devices were tested for integrity prior to measurements. This was done with the component test system from Keithley. The actual breakdown voltage was also measured on five devices of each type using the component tester. As expected, this was considerably higher than the rated maximum breakdown voltage specified by the manufacturers. The respective mean value of the measurement and the deviations are given in Table 4.1.

Tab. 4.1.: Mean value of the measured breakdown voltages on each of five non-irradiated components.

	Type A	**Type B**	**Type C**	**Type D**
$V_{DS}(measured)$	849 ± 76 V	800 ± 37 V	1412 ± 81 V	1004 ± 83 V

Tab. 4.2.: Chosen devices for the experiments, their key characteristics and the irradiation facility is listed.

Device	**Type**	**Technology**	$\mathbf{V}_{DS(max)}$	$\mathbf{I}_{DS(max)}$	**Test-site**
Type A	GaN HEMT	GaN on Si p-AlGaN layer	650 V	7.5 A	GANIL ISIS CERN INT OncoRay
Type B	GaN HEMT	GaN on Si gate injection	600 V	13 A	GANIL ISIS CERN INT OncoRay
Type C	GaN HEMT	Cascode-Structure MIS-type HEMT	600 V	9 A	ISIS CERN OncoRay
Type D	SiC MOSFET	MOSFET n-type	650 V	21 A	ISIS INT OncoRay
FBH	GaN HEMT		600 V		ISIS

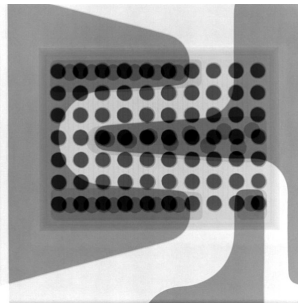

(a) X-Ray image from the die

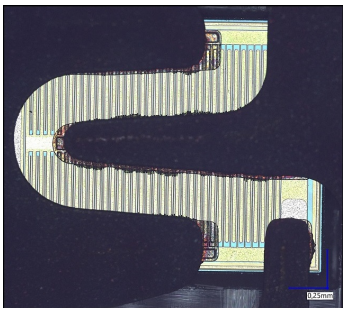

(b) Microscope image

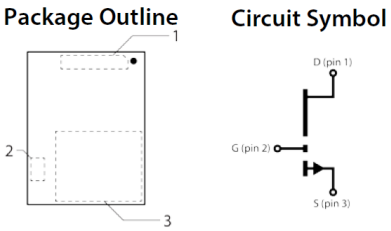

(c) Package and circuit symbol

Fig. 4.1.: (a) X-Ray image from the *Type A* die (b) Microscope image of the opened device. In the middle of the picture is the die, the gate connection on the bottom, the drain at the left and the source connection at the right. (c) Schematic package outline and circuit symbol [82].

Device Type A

The first device is a GaN HEMT grown on silicon with an p-layer Schottky-gate [83, 84]. The device is cooled by extensive bottom sided metal panels, which allows for a very flat design and low thermal resistance.

The devices are very small and strikingly flat, with not even a millimeter height. The underlying structure showed large circuit boards directly connected to the DUT, eliminating the need for bonding wires. The structure is stabilized by a type of fiberglass. In the X-ray image 4.1a the rectangular dimensions of the die can be seen, as well as the conductor boards pointing into the die.

It was possible to remove the package from one device using a plasma decapsulator. Figure 4.1b shows the microscope image of the opened device. The die is located in the center, the drain- and source plates can be seen at the top and bottom of the image, and the gate electrode at the left. The plates are directly connected to the package for cooling. The lateral die design and the flat conductor plates make the low height of the construction possible.

Figure 4.1c shows the package layout and the circuit symbol [82].

Type A Devices	
V_{DS}	$650\,V$
$I_{DS}(max)$	$7.5\,A$
$I_{DS}(leak)$	$0.5\,\mu A$
I_{GS}	$40\,\mu A$
V_{th}	$6\,V$
$R_{DS}(on)$	$200\,m\Omega$
Dimensions	$5.0 \times 6.6\,mm^2$
	$0.51\,mm$ height
die interface	$\approx 0.03 \pm 0.005\,cm^2$

Type B Devices	
V_{DS}	$600\,V$
$I_{DS}(max)$	$13\,A$
$I_{DS}(leak)$	$39\,\mu A$
I_{GS}	-1 μA
V_{th}	$10\,V$
$R_{DS}(on)$	$190\,m\Omega$
Dimensions	$8 \times 8\,mm^2$
	$1.25\,mm$ height
die interface	$\approx 0.04 \pm 0.004\,cm^2$

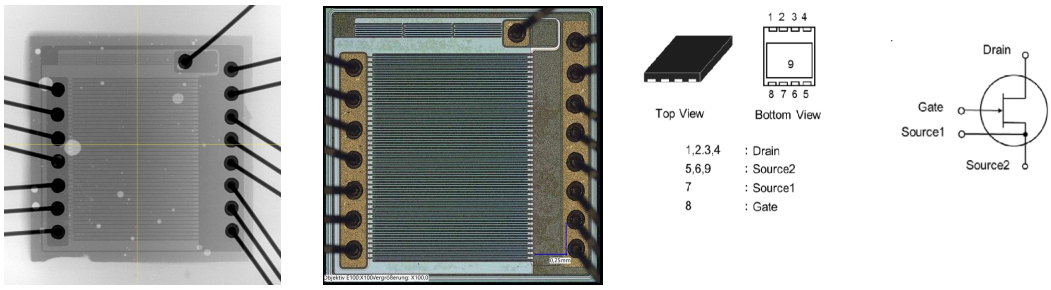

(a) X-Ray image of the device

(b) Microscope image of the opened device

(c) Package and circuitry

Fig. 4.2.: (a) X-ray image of the device *Type B*. (b) Microscope image of the opened device. The connection to the device contacts is made by bonding wires. The wires at the left of the picture go to the drain, the wire at the top right go to the gate and the wires at the right side go to the source. (c) Schematic package outline and circuitry [85].

Device Type B

This device is also a GAN HEMT grown on silicon. In order to achieve the normally-off state for his GaN HEMT devices the manufacture of device *Type B* developed a method to use hole-injection from a p-AlGaN layer under the gate to the AlGaN/GaN heterojunction [53, 85]. This also leads to a higher electron density in the channel and an increase of the drain current.

In the X-ray image of a classically bonded die can be seen 4.2a. The wires at the left of the picture go to the drain, the wire at the top right connect the gate and the wires at the right side go to the source.

The *Type B* DUT is slightly larger than the *Type A* device. It is about twice as high and the surface area is larger. It was also possible to remove the package of this device with a plasma decapsulator. A microscope image of the internal structures can be seen in figure 4.2b.

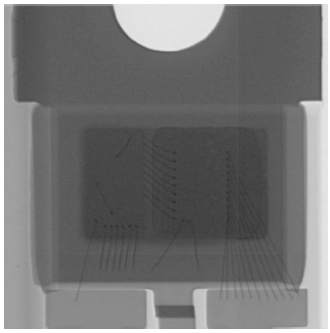

(a) X-Ray picture of *Type C* the device

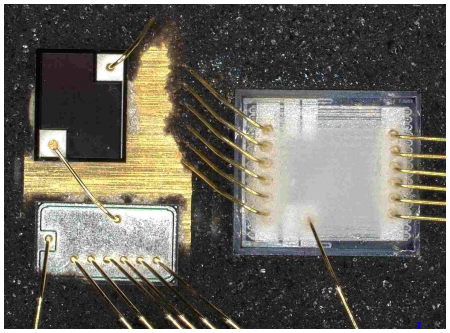

(b) Microscope image the device

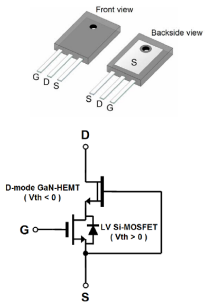

(c) Package and circuit of the *Type C* device

Fig. 4.3.: (a) X-ray image of the device. It can be seen that the dies are connected with bonding wires. The Si MOSFET is on the left, the GaN HEMT on the right [86]. (b) Microscope image of the opened DUT (c) Schematic package outline and circuit of the *Type C* Device [52].

Device Type C

The *Type C* GaN HEMT uses a completely different technology to achieve the normally-off condition for the devices contrary to *Type A* or *B*. The manufacturer uses his mass production MIS-type high voltage normally-on GaN HEMT in a cascode configuration with a low breakdown voltage Si MOSFET [52] as can be seen in the schematic circuit in figure 4.3c. Figure 4.3a shows an X-ray image of the device, in which the outlines of the other dies can be recognized. In microscope image 4.3b, the diode can be seen on the top left, the MOSFET on the bottom left and the GaN DUT on the right. The latter is covered with an additional isolating layer.
This device has a classic TO-package and has already been qualified by the manufacturer with regard to mechanical stress [86]. The DUT itself is only slightly larger than the *Type B* devices, but the height is about twice as thick. Due to the legs and the cooling fin, it is overall significantly larger than *Type A* or *Type B*. The manufacturer's data sheet states that this type of component is JESD-47 qualified [87].

Type C Devices	
V_{DS}	$600\,V$
$I_{DS}(max)$	$9\,A$
$I_{DS}(leak)$	$8\,\mu A$
I_{GS}	-100/100 nA
V_{th}	$9\,V$
$R_{DS}(on)$	$290\,m\Omega$
Dimensions	$10.2 \times 14.9\,mm^2$
	$4.5\,mm$ height
GaN-die interface	$\approx 0.04 \pm 0.008\,cm^2$
Si-die interface	$\approx 0.03 \pm 0.008\,cm^2$

Type D Devices	
V_{DS}	$650\,V$
$I_{DS}(max)$	$21\,A$
$I_{DS}(leak)$	$1\,\mu A$
I_{GS}	-100/100 nA
V_{th}	$9\,V$
$R_{DS}(on)$	$120\,m\Omega$
Dimensions	$21 \times 16\,mm^2$
	$5\,mm$ height
die interface	$\approx 0.03 \pm 0.009\,cm^2$

(a) Opened DUT

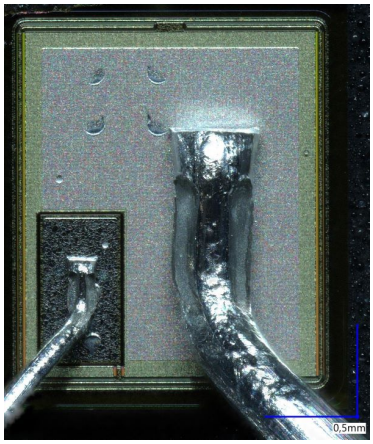

(b) die microscope image

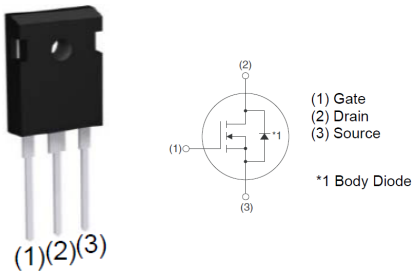

(c) package and symbol

Fig. 4.4.: (a) Picture of the opened DUT with the very small area share die. (b) Microscope image of the die. (b) Schematic package outline and DUT-symbol of the *Type D* device, taken from the data sheet [88].

Device Type D

In addition to the three GaN HEMT devices, a silicon carbide MOSFET with comparable properties was irradiated.
SiC MOSFETs have been on the market longer and the technology is reasonably well-known so the device was chosen to give a comparison baseline for measurements with different nucleons.
Immediately noticeable is the significantly larger package of the device. It contains a large surface area for cooling the die [88]. The photo 4.4a shows the opened DUT with the die inside. The size of the die compared to the cooling base is clearly visible.
Figure 4.4b shows a microscope image of the die.

Devices from the FBH

Kindly Dr. Oliver Hilt from the Leibniz Ferdinand Braun Institute (FBH, Berlin) [89, 83] provided ten power GaN HEMTs and detailed information about the structure of the devices. It was possible to irradiate these DUTs on the *ChipIR* at the ISIS neutron source (Rutherford laboratory Oxfordshire, UK) and discuss the results with Dr. Oliver Hilt.
The devices came with the die mounted and bonded to a microwave package. The design of the devices and the package can be seen in figure a. A photograph of the device shows the die and the bonding wires 4.5a.

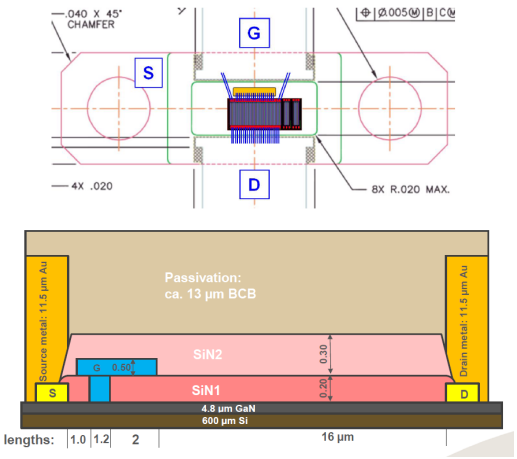

(a) Structure of the FBH devices

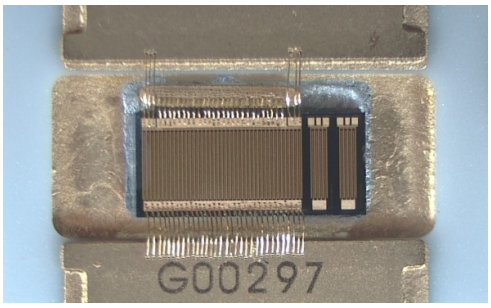

(b) Photograph of the device

Fig. 4.5.: (a) Schematic package outline and structure from the FBH devices. (b) Photograph of the DUTs [90].

FBH Devices	
V_{DS}	$600\,V$
$I_{DS}(max)$	$65\,A$
$I_{DS}(leak)$	$< 1\,\mu A$
V_{th}	$> 1\,V$
$R_{DS}(on)$	$65\,m\Omega$
Dimensions	$17.8 \times 20.3\,mm^2$
	$2.03\,mm$ height
die interface	$0.1012\,cm^2$

4.2. Heavy Ions and Proton Experiments

4.2.1. GANIL - Heavy Ions (high LET)

Ion	Xe
Energy	49 $\frac{MeV}{nucleon}$
Degrader	400 μm Al
LET Air	27.76 $\frac{MeV\,cm^2}{mg}$ (Si)
LET Al-Degrader	44.46 $\frac{MeV\,cm^2}{mg}$ (Si)
Beam size	49×4 cm^2
Beam intensity	$\varnothing$ 4.8 10^3 $\frac{Ions}{cm^2\,s}$
DUT	7 × Type A
	2 × Type B

The first tests that took place were performed at the G4-cave at the Grand Accélérateur National d'Ions Lourds (GANIL) in Caen. GANIL offers the irradiation of electric components with heavy ions over a wide LET range. The facility can provide selected heavy ion beams from Argon to Lead with a large kinetic energy per nucleon [91].
A high energy Xenon-beam with an energy of 49 $\frac{MeV}{nucleon}$ and an ion flux of 2-5·10^3 $\frac{Ions}{cm^2\,s}$ was used. The ion energy refers to a surface LET of 27.76 $\frac{MeV\,cm^2}{mg}$ in Si. The structure to be irradiated is placed onto a sample holder in front of the stainless steel beam exit window. Aluminum-degraders could be put between the beam exit window and the sample holder to vary the nucleon energy and therefore the LET up to 44.46 $\frac{MeV\,cm^2}{mg}$ (Si). The dosimetry was carried out by the GANIL-employee and the data were handed over to the experimenter. The deviations in beam homogeneity were less than ±10%.
The experiment was dated to an early state of the work and can be seen as a pretest for experiments to come. Only *Type A* and *Type B* devices were available for this experiment. Because of the high energy of the Xenon-ions TRIM [67] calculations showed a stopping range deeper than the thickness of the DUTs even with a Cu-plate, meaning there was no need for delidding the devices.
The test board could hold three devices at a time and were mounted to the sample holder. Alignment of the DUTs in the board to the beam exit were done with help of the laser system on site. After the failure of the three DUTs, the cave needed to be entered and the DUTs manually replaced. Two photographs of the experimental set up are shown in

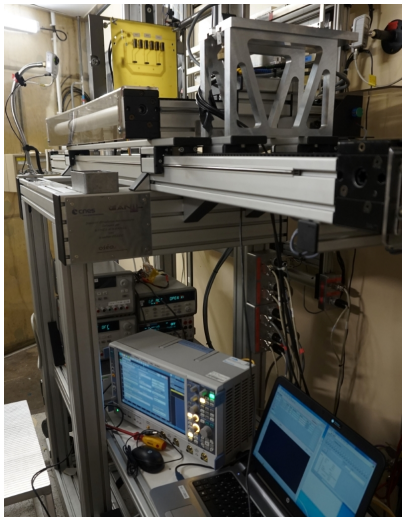

(a) Setup in the G4-Cave

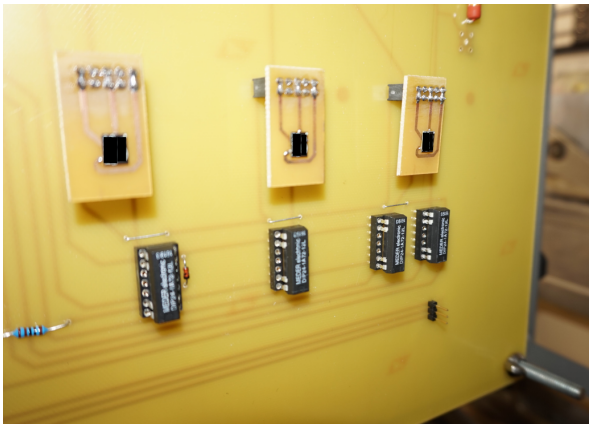

(b) test board

Fig. 4.6.: Photographs of the setup in the GANIL-Cave G4, June 2018. (a) the measurement board in front of the beam exit window is seen and underneath the SMUs and the laptop for data collection. (b) test board with DUTs mounted for irradiation

figure 4.6. Picture (a) shows the installed component board, with the measurement laptop and SMUs underneath. The viewing direction is to the back of the board, against the beam direction. Picture (b) shows the front side of the board with three mounted devices.
During the experiment the DUTs were operated in blocking voltage while irradiated and the leaking currents I_{DS} and I_{GS} were constantly measured and logged. If the leaking current rose out of the specification it was classified as a failure of the DUT. The failures that occurred during this experiment were full breakthroughs with the current rising up to $1\,mA$ before the SMU limited it off.
It was possible to irradiate seven DUTs of device *Type A* and two of devices *Type B* during a three hour period. In figure 4.7 the measured steps are shown. Starting the experiment with irradiation of DUT 1 at $V_{DS} = 600\,V$ and scanning the sensitive voltage range from below with DUT 2. Every point gives a measured voltage step and the x marks a failure of the devices, identifiable by the DUT number. If no failure occurred the devices were irradiated up to $10^6\,\frac{Ions}{cm^2}$.
To get information of the influence of applied gate voltage, DUTs 4, 5 and 6 were operated with the blocking voltage V_{DS} and a negative gate voltage of $V_{GS} = -10\,V$. DUTs 6 and 7 were also irradiated with the $400\,\mu m$ Al-degrader between beam exit window and device board to change the LET to $42.03\,\frac{MeV\,cm^2}{mg}$ (Si). All device failures were above $V_{DS} = 400\,V$ which is higher than 65% of the rated drain voltage.

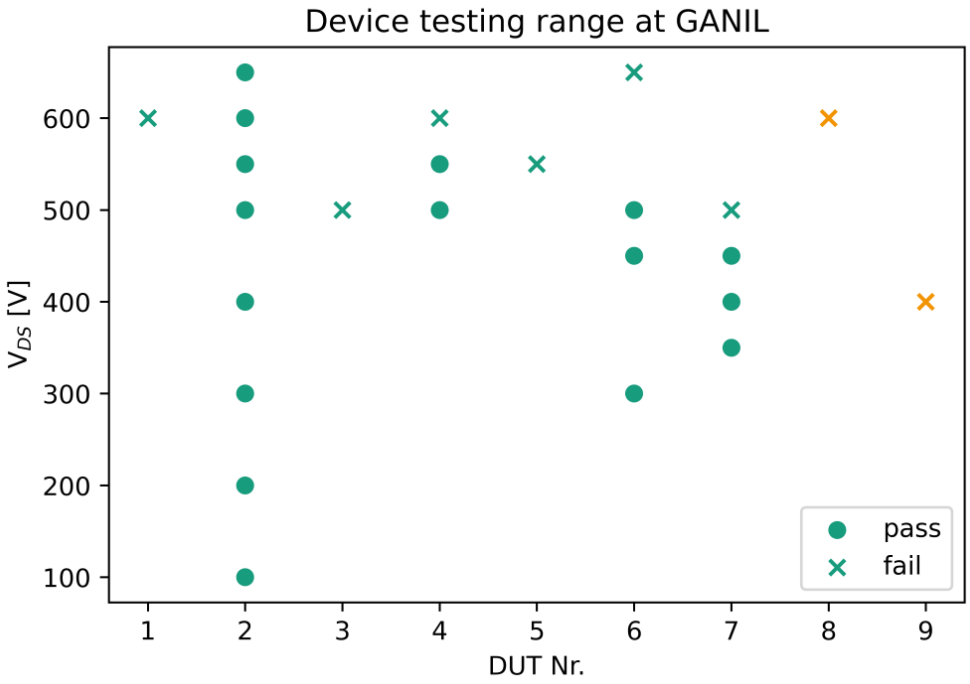

Fig. 4.7.: Testing range for the devices tested at GANIL. *Type A* green, *Type B* orange. DUTs 4, 5, and 6 were measured with a negative V_G.

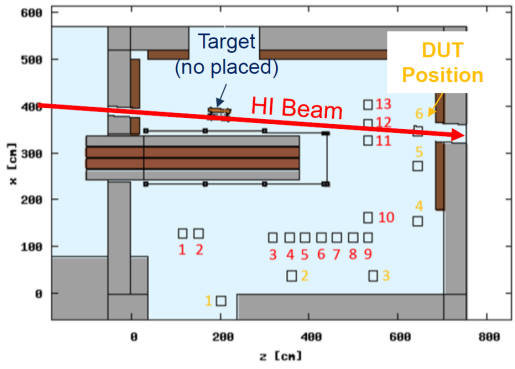

(a) Irradiation Cave of the CHARM facility at CERN

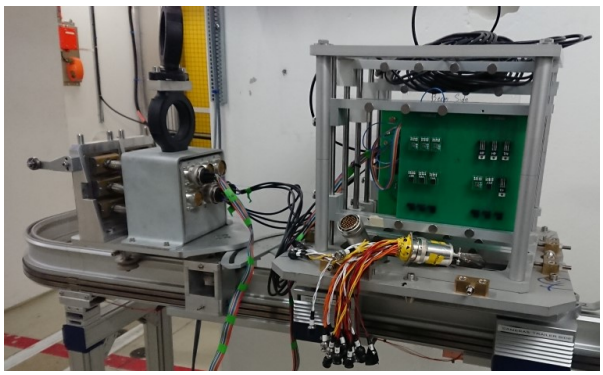

(b) Montrac robot for bringing the test setup into the cave

Fig. 4.8.: (a) Layout of the CHARM-Cave. The Montrac test position is numbered with a yellow six [92]. (b) Photograph of the Montrac mounting rack.

4.2.2. CHARM at CERN - Heavy Ions (low LET)

Ion	Pb
Energy	6 $\frac{GeV}{nucleon}$
LET	7.98 $\frac{MeV\,cm^2}{mg}$ (Si)
Beam size	10×10 cm^2
Beam intensity	106 $\frac{particles}{spill}$,
	spills 350 ms long
DUT	4 × Type A
	4 × Type B
	4 × Type C

The irradiation facility *CHARM* at CERN lays on the end of the T8 beamline on the Meyrin Side of CERN in Switzerland [93]. For the normal experimental Setup in this cave a 24 GeV proton beam is extracted from the PS-Accelerator and directed through the T8 beamline to the *CHARM*-Cave where it hits a target and produces a mean field of secondary radiation products [94],[92]. A layout of the *CHARM* cave can be seen in left figure 4.8a. Due to the high radiation field, it is not possible to enter the cave so the experimental setup has to be mounted on a transportation system (Montrac) and moved to the radiation position. Yellow numbers mark possible positions of the Montrac transportation system, and the possible irradiation positions. Red numbers are selectable shielding and Target marks a possible target to be brought into the beam.
Our experiment was an in-beam experiment in the *CHARM* cave with a high energy Pb-beam at about 6 GeV, so no target or shielding were used.
The beam enters the cave from the left side in the direction of the arrow. Every spill from the Proton Synchrotron (PS-accelerator) contains about 10^8 ions and lasts 48 seconds.
The device board was mounted onto the Montrac transportation system and could hold six Devices at a time. The Montrac with the mounted device board and DUTs is shown in figure 4.8b. Due to the high radiation field it took some time to enter the area and change the DUTs even with the Montrac moved as far out as possible. With that we could only irradiate two sets of six DUTs during the experiment. Each time three DUTs were in the beam window of about 10 x 10 cm^2 diameter and irradiated at the same time up to minimal $3 \cdot 10^8$ $\frac{Ions}{cm^2}$ (up to $9 \cdot 10^8$ $\frac{Ions}{cm^2}$), the deviations in beam homogeneity were less ±10%.
A graph with the measured voltage steps and failure events is given in figure 4.9. Each dot

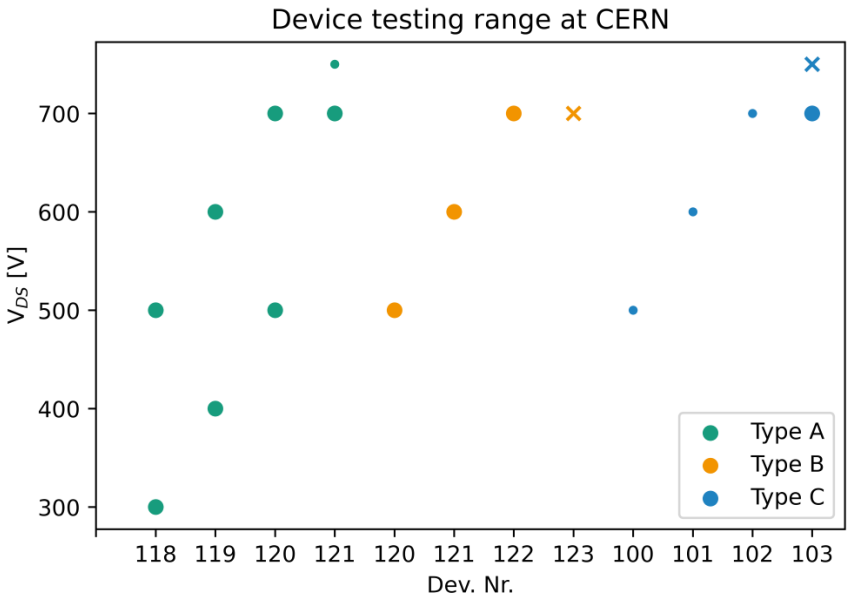

Fig. 4.9.: Plot of the testing Range for the different device types at the CHARM facility, *Type A* green, *Type B* orange and *Type C* blue. Points symbolize passed measurements, the smaller points an increase of the leakage currents I_{DS} and x a device failure during the measurement.

indicates a measurement step. The large dots represent functioning DUTs, the smaller dots devices with increased leakage current (I_{DS} or I_{GS}) and the crosses mark failed devices. The devices of *Type A* showed only some slow degeneration during the beam time and continued to work within their specifications. *Type B* worked like a detector for the beam as every incoming beam spill from the PS-accelerator was clearly marked by a temporary increased leakage current I_{DS} as shown in figure 4.10. Every peak in the plot correspond to an incoming ion spill of the PS accelerator. The DUTs of *Type C*, which showed little susceptibility for neutron irradiation, showed a fast increasing leakage current I_{DS} far out of the manufacturers specifications which speaks for an ongoing degeneration of the device.

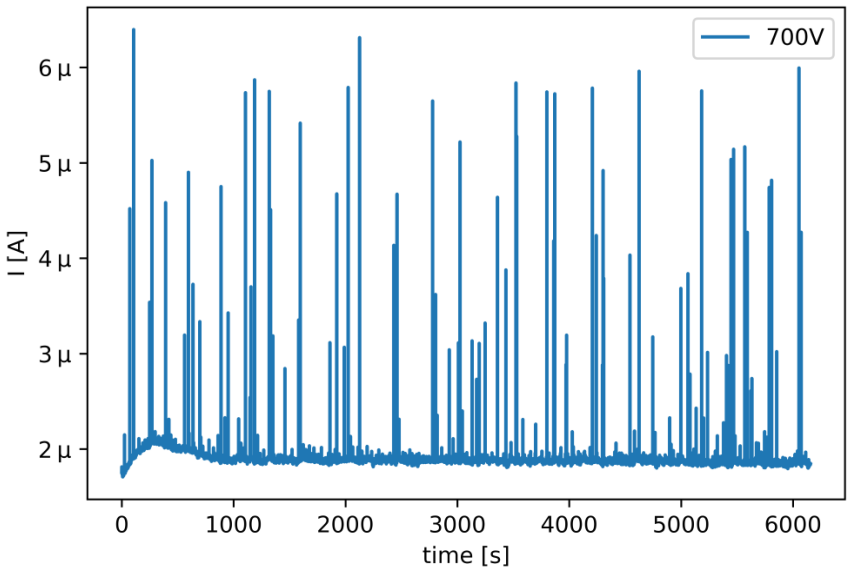

Fig. 4.10.: Plot of the measured *Type B* I_{DS} with V_{DS}=700 V applied at CHARM. Every peak correlates to an ion spill from the PS-accelerator.

(a) Irradiation cave **(b)** Layout of the Facility

Fig. 4.11.: Photographs from the experiment at the OncoRay, Dresden, (a) beamline and experimental setup. (b) schematic picture of the radiation area with the cyclotron (taken from [95]).

4.2.3. OncoRay - 200 MeV Protons

Ion	p
Energy	200 $\frac{MeV}{nucleon}$
LET	$0 \approx 16\ MeV\ \frac{cm^2}{mg}$ (Si)*
Beam size	$14 \times 14\ mm^2$
Beam intensity	$\varnothing$ 0.006-1.4 $\times 10^9\ \frac{p}{cm^2\,s}$
DUT	20 $\times$ Type A
	22 $\times$ Type B
	22 $\times$ Type C
	9 $\times$ Type D

*maximum LET-range [65]

OncoRay is the proton cyclotron accelerator of the National Center for Radiation Research in Oncology (NCRO) in Dresden, Germany [95]. The *OncoRay* Center enables scientists to do research parallel to providing treatment for patients. In order for this to be possible, a specific research radiation area is allocated as shown in picture 4.11b. Whenever the proton beam is not needed for therapeutic purposes, it is redirected to the experimental area.
The experiment was performed with a $200\,MeV$ proton beam. The beam size of $10\,x\,10\,mm$ diameter allows to irradiate one DUT at a time. The flux was variable as the cyclotron can provide a beam current from $5\,pA$ up to $1\,nA$ during the irradiation and thus a configurable flux.
An accurate dosimetry of size and homogeneity for the beam window was performed by the operators at the beginning of the experiment and repeated every day before the start of irradiation. The deviations of the beam homogeneity were less than $\pm 10\%$ and the dosimetry files given after the experiment.
The device board was mounted in front of the beam window and aligned with a laser system. A micro-step motor could move the test board in x-direction, so that ten devices could be mounted and irradiated before the need to enter the radiation cave again. The devices were also operated with V_{DS} applied, and the leakage I_{DS}, I_{GS} currents measured and logged.
It was possible to irradiate 73 DUTs, some up to $5{\cdot}10^{12}\ \frac{p}{cm^2}$ as seen in Fig. 4.12. Destructive failures could be seen in all device types.

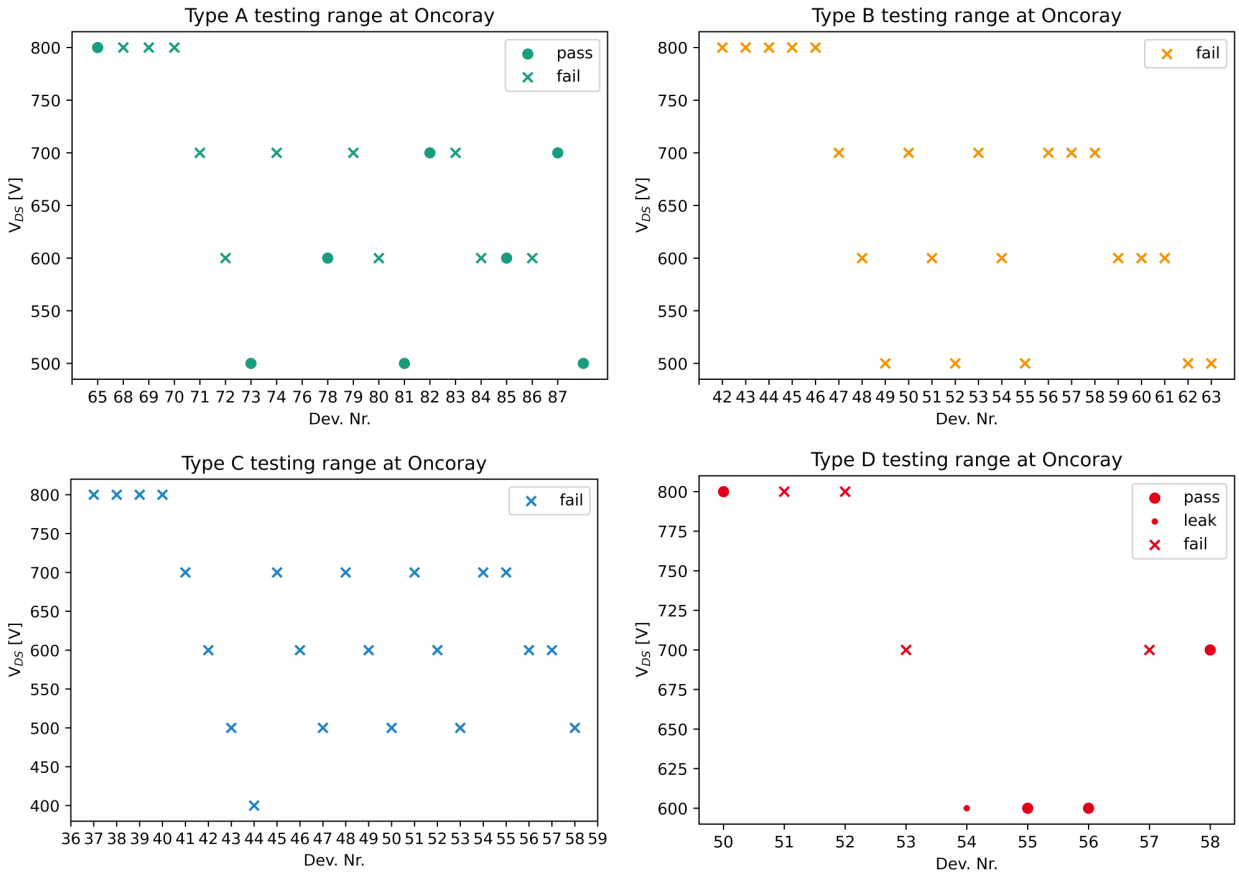

Fig. 4.12.: Plot of the testing range for the different device types at OncoRay. x marks a failure of the device at this irradiation step. The devices are identifiable due to the DUT number

4.3. Neutron Experiments

4.3.1. ChipIR at ISIS Neutron Source - Atmospheric Neutrons

Nucleon	n
Energy	0-800 $\frac{MeV}{nucleon}$
Beam size	7×7 cm^2
Beam intensity	$\varnothing\, 3.8 \times 10^6\, \frac{n}{cm^2\, s}$
DUT	21 × Type A
	20 × Type B
	12 × Type C
	14 × Type D
	10 × FBH

The ISIS neutron source at the Rutherford laboratory (Oxfordshire, UK), is the most atmospheric spectrum-like neutron source available in Europe at the time. An $800\, MeV$ Synchrotron proton beam interacts with a beryllium reflector target composite and produces neutrons from $0 - 800\, MeV$ with a flux up to $10^7\, \frac{n}{cm^2\, s}$ (integrated above $10\, MeV$) [96] at the irradiation cave *ChipIR* [97]. ChipIR has an independent shutter so that the beam can be opened and stopped individually while the accelerator is running, and is provided with a $70 \times 70\, mm^2$ diameter neutron beam.
Dosimetry was provided by the facility and was made available later. The beam inhomogeneity across the beam window was smaller than ±10%.
The radiation area is equipped with an x-y-z table so that the board can be moved from the control room. With that it was possible to mount 18 DUTs on the device board and irradiate (three at a time) before entering the radiation area again.
The experiment gave us the opportunity to test all four device types, 77 DUTs in 119 Runs, with different configurations. In addition, the devices of the Ferdinand Braun Institute (FBH) could be examined. In every run three DUTs were irradiated simultaneously, while each DUT was controlled individually and the currents I_{DS} and I_{GS} logged with three Keithley SMUs.
For the measurements, the devices were operated with the blocking voltage V_{DS} applied. The testing range and failure voltages are shown in figure 4.13 with one point per measuring step. The x's indicate a device failure.

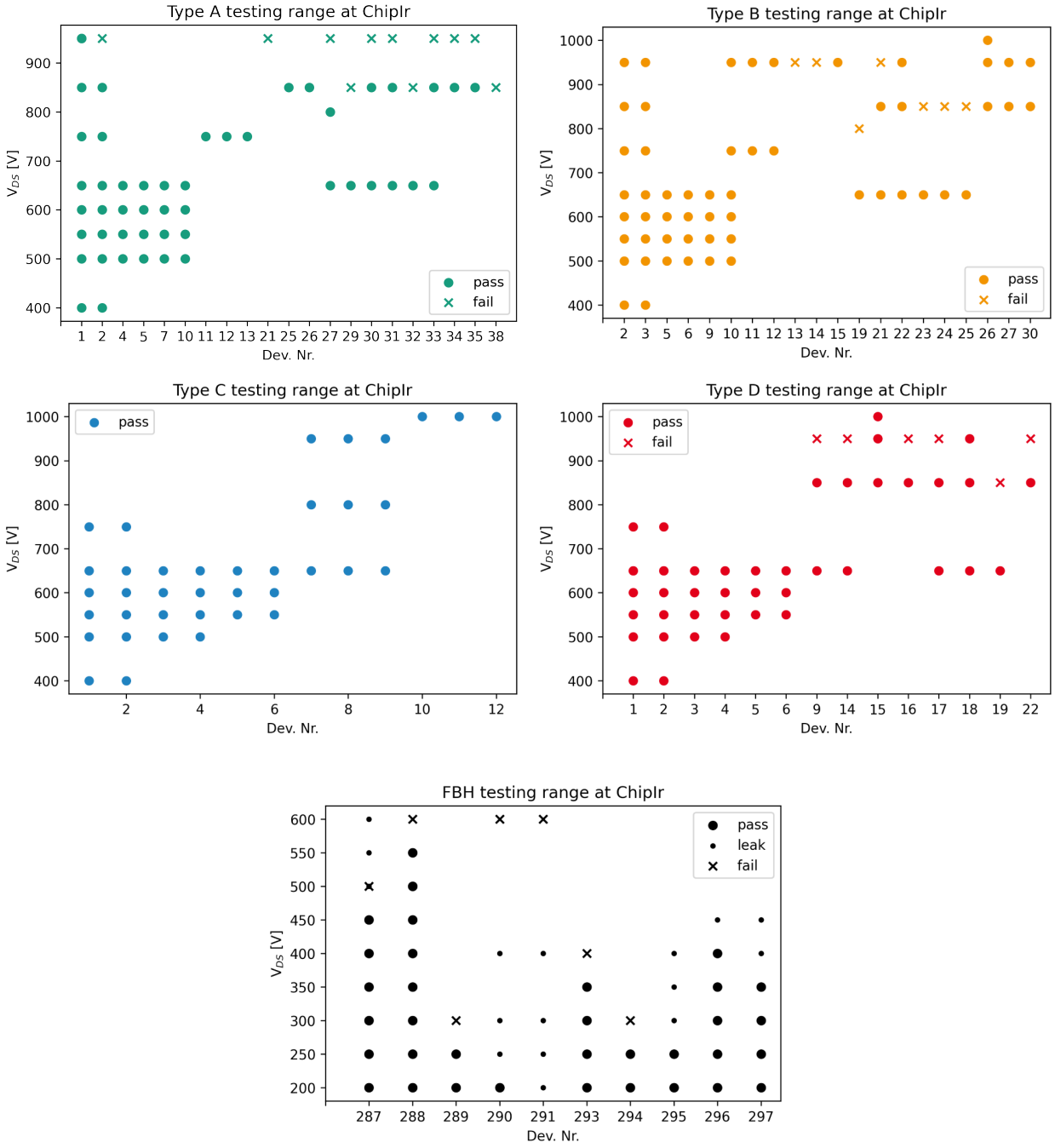

Fig. 4.13.: Testing range of the experiment at the ISIS neutron source. Every row gives the measured voltage steps for the DUT identifiable through the device number. Dots mark the passed measurements, and x the voltage at which a failure occurred. The smaller dots at the FBH devices show increased leakage currents.

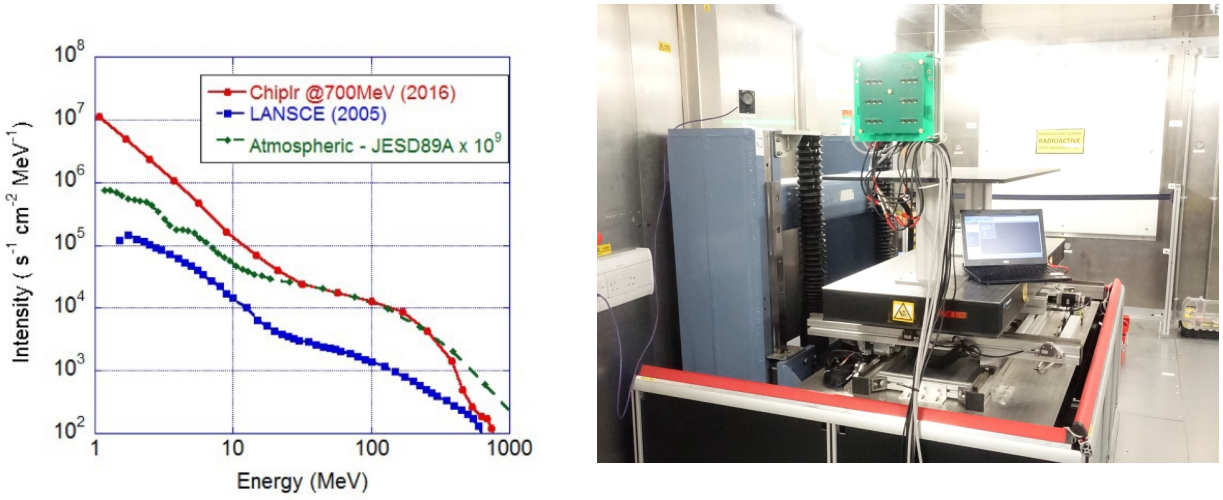

(a) Neutron-spectrum

(b) Irradiation cave

Fig. 4.14.: (a) The spectrum of ISIS-neutron source (green) compared to the atmospheric spectrum (green), and the spectrum receivable at LANSCE (blue) [76]. (b) Photograph of the irradiation cave and the experimental setup at *ChipIR*.

All of the commercial devices survived irradiation with the neutron spectrum within their specifications and above. The surviving DUTs were irradiated at least up to $2.2{\cdot}10^9 \frac{n}{cm^2}$. Device *Type C* showed no SEE at all. Even with a blocking voltage of V_{DS}=1000 V applied (the maximum voltage range of the SMUs) no destructive failure occurred. Only the FBH-devices showed breakthrough failures as low as $V_{DS} = 300\,V$, or a significant increase in leakage current was seen without the components being completely destroyed. This is indicated by a smaller dot in the lower part of graph 4.13.

4.3.2. Fraunhofer INT - 14 MeV Neutrons

Nucleon	n
Energy	$14\,\frac{MeV}{nucleon}$
Beam size	Point source
Beam intensity	$1.6 \times 10^6\,\frac{n}{cm^2\,s}$
DUT	11 × Type A
	11 × Type B
	2 × Type D

The measurements with monoenergetic neutrons took place at the Fraunhofer INT (Euskirchen, Germany) [98] December 2019, January 2020 and April 2023. A THERMO-Fischer D-711 accelerator produces neutrons with an energy of 14.1 MeV due to a D-T-Reaction. Accelerated deuterium ions hit the tritium target and produce helium and a fast neutron. Based upon the fact that the energy of the neutrons (14 MeV) is much larger than the kinetic energy of the deuterium ions (≈150 keV) the emission is nearly isotropic and the intensity falls off as $\frac{1}{r^2}$ with r being the distance from the tritium target.
The neutron fluence is monitored online during the irradiation with a calibrated uranium-238 fission chamber FC165/402 at a fixed distance of 1m from the source point. A second fission chamber is placed about 10 cm away from the target. Because the emission is nearly isotropic, the fluence at the distance r of the DUT is calculated according to following equation:

$$\Phi(r) = \Phi_{r_0} \cdot \frac{r_0^2}{r^2}$$

With $\Phi(r)$ as fluence at the distance r of the DUT, $r_0 = 1\,m$ the distance of the fission chamber and Φ_{r_0} the measured neutron fluence from the fission chamber.
To obtain an acceptable fluence, it was necessary to position the DUTs up to 7 cm close to the target. In order to maintain the necessary particle homogeneity at this distance, only two devices could be irradiated and measured at a time. The average fluence during the measurements was $1.6 \cdot 10^6\,\frac{n}{cm^2\,s}$ The devices were irradiated in the blocked state with V_{DS} applied, as well as the leakage currents I_{DS}, I_{GS} measured and recorded.
Since no single event effects were seen in the experiment at the *ChipIR* ISIS neutron source within the specifications of the devices, the experiment with 14 MeV neutrons was started with the lowest blocking voltage V_{DS} at which errors had occurred in the *ChipIR* experiment. The device *Type C* having shown no failures even with high voltages at the full atmospheric

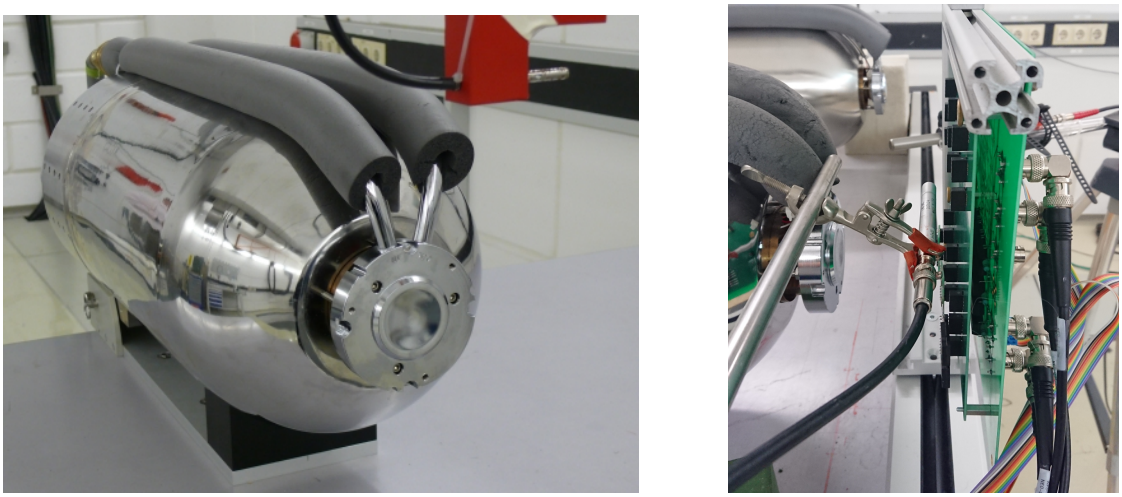

(a) Neutron generator **(b)** Test board

Fig. 4.15.: (a) Photograph of the neutron-generator. (b) Setup of the measuring board in front of the n-generator at Fraunhofer INT and a ionization chamber above the target.

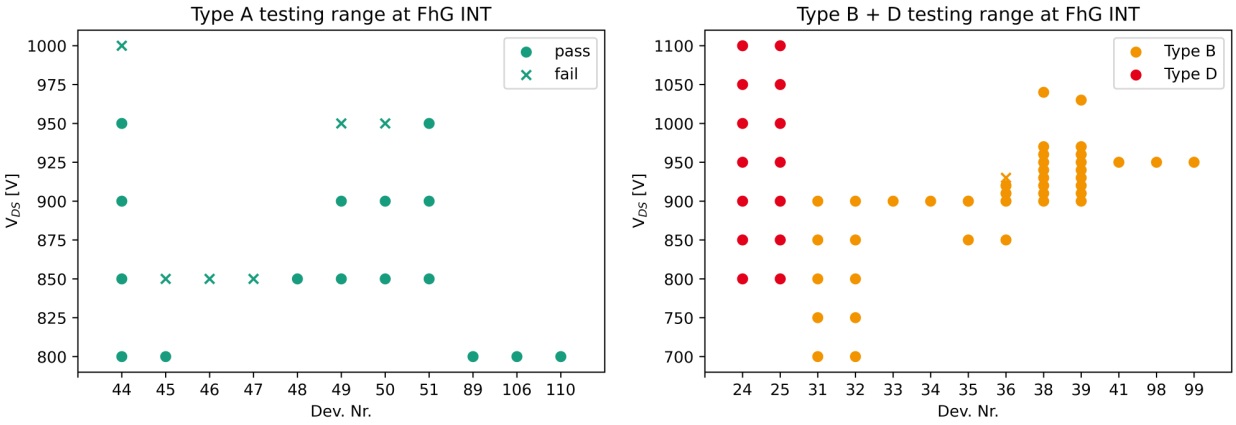

Fig. 4.16.: Plot of the testing Range for *Type A* and *B* devices at Fraunhofer INT. Of device *Type D* were only two DUTs, and no fails were registered.

neutron spectrum measurements, this device type was excluded from the experiment with $14\,MeV$ neutrons.

The lowest voltage where a SEE occurred during the experiment at Fraunhofer, was $850\,V$ for *Type A* DUTs. This voltage is beyond the given manufacturer specifications ($V_D = 650\,V$). *Type B* DUTs showed only one device failure, but this occurred promptly after switching on the device and cannot be clearly attributed to a radiation effect. This measurement was therefore excluded from further evaluations. With the *Type D* devices, no failure occurred up to $1100\,V$ blocking voltage and $4.1 \cdot 10^{10} \frac{n}{cm^2}$ so the measurements were stopped at this voltage. Figure 4.16 gives the testing range and fail voltages.

5. Results and Evaluation of the Experiments

From the measured values presented above, it is possible to develop a number of conclusions about the devices and the GaN-technology. As an initial overview, all device failures obtained in the experiments are summarized in table 5.1. For each particle sort the total number of measured DUTs per device type and voltage step is given as denominator and the number of measured device failures as numerator. In total 63 *Type A* device, 59 *Type B*, 38 *Type C* and 25 *Type D* were measured. In addition, 10 devices were provided by *FBH*, resulting in a total of 195 DUTs being irradiated.
Following this information, in the first part of this chapter, the measured values and results, like the device survival rate, the cross section and an upper limit for the safe operation voltage of the components are evaluated and presented. Also, the dependence of the error rate on the applied blocking voltage V_{DS} and fluence is investigated.
In the second part, the influence of the particle type as well as the particle energy on the cross section, are considered. In particular, the influence of the linear energy transfer is investigated. The results will be related to conclusions of previous publications and the relation between the LET and the single event effect susceptibility will be examined.
The comparability between proton and neutron measurements, including the measurement with monoenergetic $14\,MeV$ neutrons is considered separately. This includes the feasibility of evaluating single event effect tests for terrestrial applications in GaN with protons or $14\,MeV$ neutrons.
In the last section of this chapter, the influence of the device bias like the gate voltage V_{GS} on the error rate is investigated. Furthermore, the measurements are examined with respect to the error mechanism found by [19] and [61] in high frequency devices and normally off components which have a GaN HEMT structure.

Tab. 5.1.: Quantity of measured devices and device failures. Listed per irradiation particle type, component type and applied blocking voltage. Count of failures is given as numerator, and the total number of measured DUTs as denominator.

		Voltage [V]																
		100	200	300	350	400	450	500	550	600	650	700	750	800	850	900	950	1000
$n_{14\,MeV}$	Type A													0/5	3/8	0/4	2/4	1/1
	Type B											0/2	0/2	0/2	0/4	0/8	0/5	0/2
	Type D													0/2	0/2	0/2	0/2	0/2
n_{atmos}	Type A					0/2		0/6	0/6	0/6	0/12		0/5	0/1	3/12		8/9	
	Type B					0/2		0/6	0/6	0/6	0/12		0/5	1/1	3/10		3/13	0/1
	Type C					0/2		0/4	0/6	0/6	0/9		0/2	0/3			0/3	0/3
	Type D					0/2		0/4	0/6	0/6	0/11		0/2		1/8		5/7	0/1
	FBH		0/10	2/10	0/6	1/8	0/4	1/2	0/2	3/4								
Pb	Type A			0/1		0/1		0/2		0/1		0/2	0/1					
	Type B							0/1		0/1		1/2						
	Typbe C							0/1		0/1		0/2	1/1					
p	Type A							0/3		4/6		4/6		3/4				
	Type B							5/5		6/6		6/6		5/5				
	Type C					1/1		5/5		6/6		6/6		4/4				
	Type D									0/3		2/3		2/3				
Xe	Type A	0/1	0/1	0/2	0/1	0/2	0/2	2/5	1/3	2/3	1/2							
	Type B					1/1				1/1								

5.1. Experimental Results

The most straightforward results of the measurements are presented here first. These include the survival rate, the safe operating area of a device at which no single event effects were measured and the cross section of the single event effect measurements.

5.1.1. Device Survival Rate

Extensive experience and many studies on silicon transistors have shown that the electronic components are more sensitive to single event effects the greater the applied voltage becomes [15]. The higher applied electric field leads to stronger and faster avalanche events and thus a breakdown of the electronic device. Initial measurements with the then new device types indicate that this relationship also exists in gallium nitride high electron mobility transistors. The avalanche effect probably does not play a role in these devices due to the different device architecture, but the degeneration of the gate and the resulting initiated breakdown of the device likely does [17, 34].
Physically, the single event effect is a statistically independent effect from other failures and thus provides a constant hazard risk. The statistical probability that a particle will deposit enough energy to trigger a SEE does not depend on the time of incidence or the fluence the device has been exposed to before. Therefore, all measured devices of one type should be equally sensitive regardless of the previous fluence received, only the distribution changes in the sense that the overall number of devices under testing decreases. For the description of this type of failures, the Poisson process and the associated exponential function (3.9) represent an appropriate choice, with λ as the value for the steepness of the exponential distribution, which is expected to increase with increasing voltage. The applied blocking voltage is an additional stress which increases the sensitivity and should therefore lead to a faster decreasing distribution function.
For every device type the total number of measured DUTs per voltage step was normalized to one and the fraction of the remaining devices plotted against the fluence in order to investigate the relationship between blocking voltage V_{DS} and the survival rate for the experiments performed. An example of how to obtain these parameters can be found in the appendix B
The exponential function (5.1) has been fitted to the measuring points, the plots are shown in figure 5.1 sorted by device type. Uncertainty of measured values result from the uncertainty in the fluence acquisition and is less than 10 %, too small to be shown in the diagram.

$$f(\mathrm{f}) = e^{-\lambda \mathrm{f}} \tag{5.1}$$

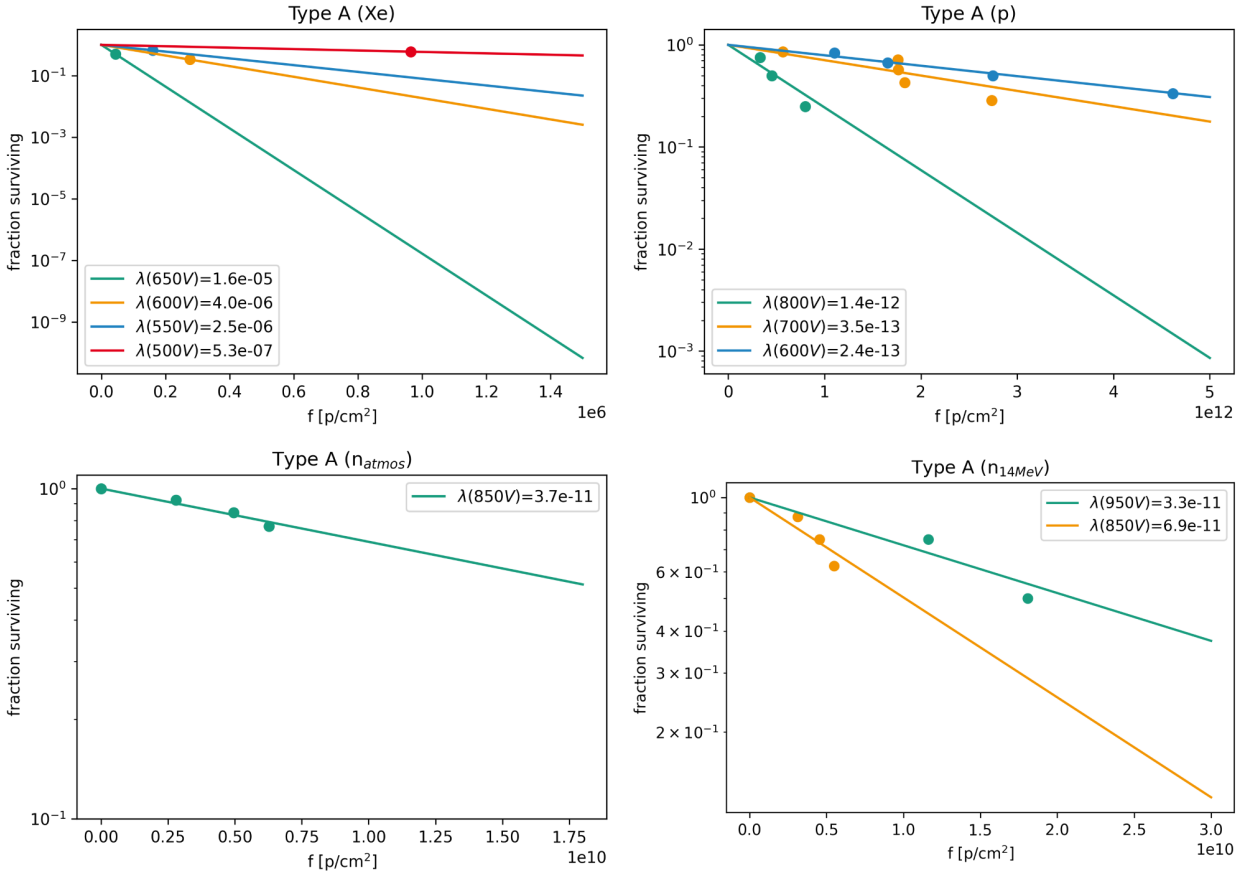

Fig. 5.1.: Fraction of the surviving *Type A* DUTs under different irradiation. The reliability of the fit corresponds to the number of measured failures and is therefore only of limited significance in the case of irradiation with Xe-ions (upper left) and 14 MeV neutrons (lower right).

The obtained λ-values, including the uncertainty, are given in table B.3. Since λ is a value for the steepness of the exponential distribution, the values are expected to increase with increasing voltage. The graphs and λ-values support the assumption that a larger applied blocking voltage leads to an increase in sensitivity also for laterally built GaN HEMT devices. Thus, the λ value increases with increasing applied blocking voltage. This is shown visually in figure 5.3, for which the λ values obtained are plotted against the applied voltage for device *Type A* as an example.

For the experiment with Pb-ions at *CHARM* (CERN) it was not possible to determine a dependency with the fluence due to the single DUT per device *Type A, B* and *C* measured per voltage step. Also, the measurement with Xe-ions in GANIL has so few measuring points for the devices that no, clear statistically, statement can be made and *Type A* is shown in figure 5.1 only for comparison. These measurements give us important information about the sensitivity of the devices depending on the applied field V_{DS} and the possibility to define

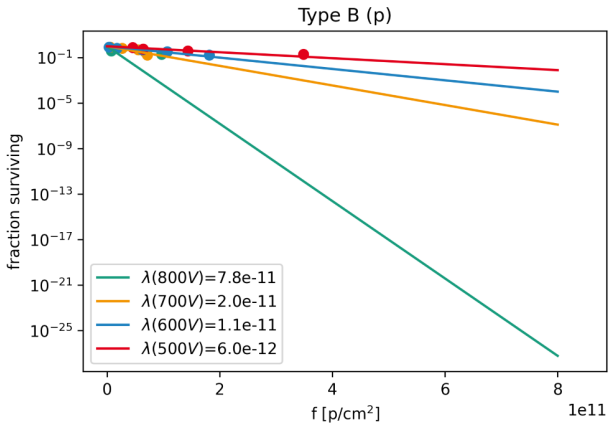

(a) *Type B* under proton irradiation

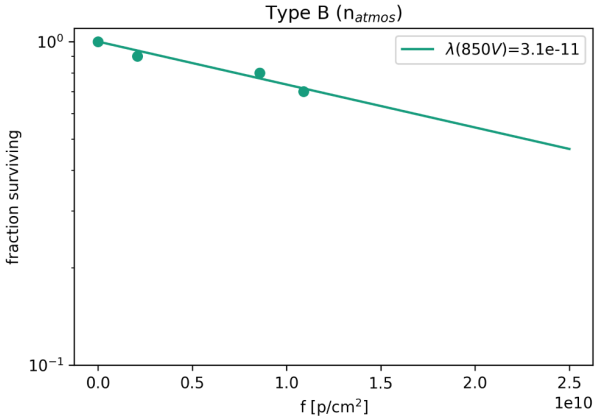

(b) *Type B* under n_{atmos} irradiation

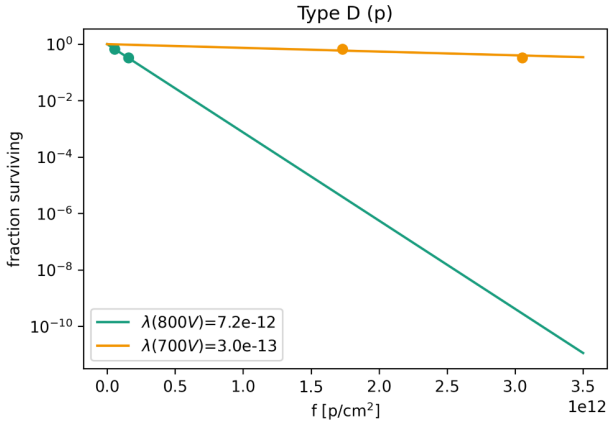

(c) *Type D* under proton irradiation

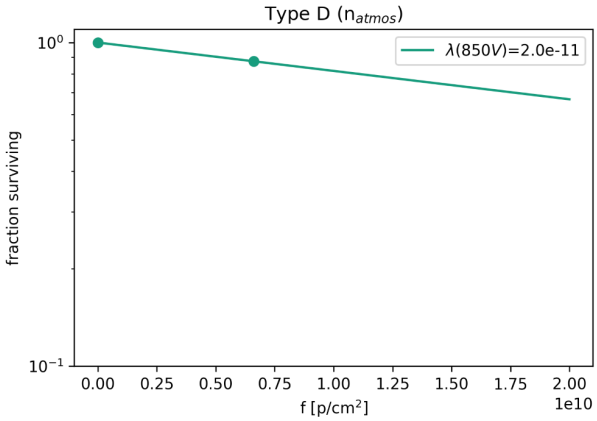

(d) *Type D* under n_{atmos} irradiation

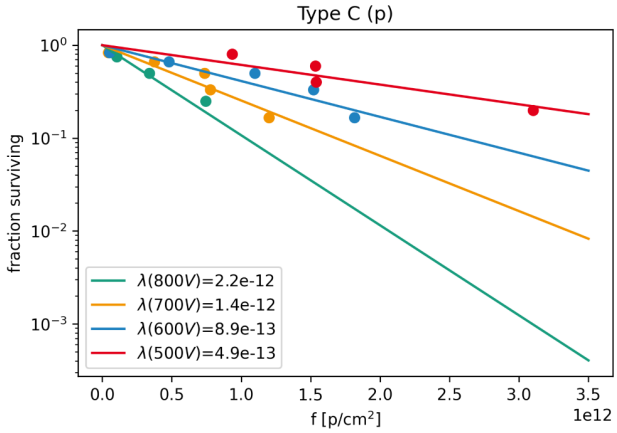

(e) *Type C* under proton irradiation

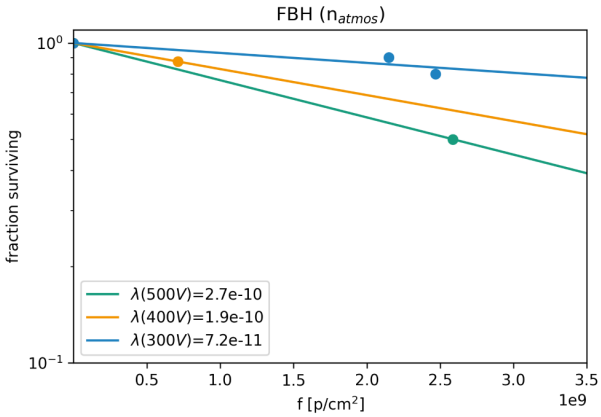

(f) *FBH* under neutron irradiation

Fig. 5.2.: Fraction of the surviving DUTs under different particle irradiation

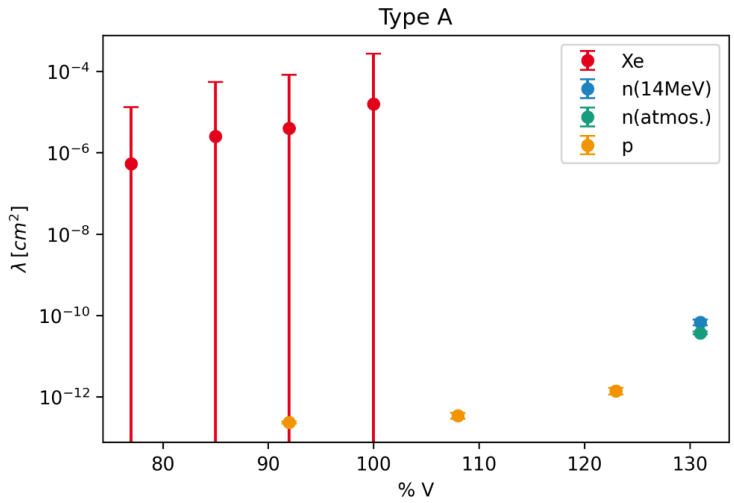

Fig. 5.3.: Plot of λ versus $\%V_{DS}$ for the components of *Type A*. As the voltage increases, λ increases and so does the device sensitivity for SEE.

a minimum voltage below which no SEE may occur (compare next section 5.1.2).
Two anomalies are to be named in the observation of the survival rate: First, it is noticeable that for the irradiation with $14\,MeV$ neutrons, the pattern of the survival rate did not develop as expected with increasing voltage. As can be seen in 5.1 the DUTs measured at $850\,V$ broke down earlier than the DUTs tested at $950\,V$. The devices, however, were also measured at $800\,V$ and $900\,V$, with no DUT breakdown (Figure 4.16). Since the average breakdown voltage of the *Type A* devices measured in advance was $850\,V$, it can be assumed that other effects contribute to the breakdown which are not related to the irradiation effects. In the further analysis, these measured values are therefore excluded. Also, for *Type B* devices, even above the average breakdown voltage, no failure could be measured with $14\,MeV$ neutrons.
Secondly, during the experiments with the atmospheric like spectrum at *ChipIR* (ISIS neutron source) for each device type (*Type A, Type B, Type D*), the survival rate at the highest measured voltage (compare graphic 4.13, the highest voltages only) shows flattening of the function with increasing fluence (figure A.1), always at the highest, individually measured voltage of the device type. It was verified that the beam current was constant for all measurements, there were no noticeable fluctuations in the recorded beam current, DUT currents or voltages. The breakdown measured were at different times on different days and the measurements were made by different people. Also, a degeneration of the DUTs over the operating time should not lead to a decrease of the failure rate. Since no statement on the accuracy of these data points, they are excluded from further analysis.

Tab. 5.2.: Smallest V_{DS} at which a device failure was measured, given in percent of the devices rated voltage. If the device type was measured but does not experience a failure, the maximum measured percent voltage is given in brackets.

Ion/Device	p	$n_{14\,MeV}$	n_{atmos}	Pb	Xe
Type A	92 %	131 %	131 %	[108 %]	77 %
Type B	83 %	[155 %]	133 %	117 %	67 %
Type C	67 %	-	[167 %]	125 %	-
Type D	108 %	[154 %]	131 %	-	

5.1.2. Safe Operating Area

For silicon transistors derating the devices, meaning operating them below their intended device maximum voltage rating, is considered protective against particle induced single event effects. The applied voltage and therefore the electric field in the device play a significant role in the sensitivity to radiation. For lower voltages the applied field is smaller compared to the material constants so that they can buffer the energies introduced without damaging the structure or gate of the device [15].

For devices, a so-called safe operating area (SOA) is defined with a given voltage V_{DS} under which no error from radiation should occur. As a condition for the determination of the SOA, an irradiation without failure of the device up to a fluence of $10^7 \frac{Ions}{cm^2}$ or $10^{11} \frac{protons}{cm^2}$ is advised [11]. From the experience, 60% of the nominal voltage is usually assumed a good boundary for the SOA and estimate to start the measurements.

To determine whether this approach with the SOA also applies to modern GaN HEMT devices, the smallest measured V_{DS} at which a device failure occurred was taken and compared with the rated voltage of the device. These are listed as a percentage of the nominal devices voltage in table 5.2.

The complete testing range for the devices are given at the experimental details in the figures 4.7, 4.9, 4.12, 4.13, 4.16 and the table 5.1. The lowest voltage at which a destructive breakdown occurred was for *Type B* and *C* at $400\,V$ with Xe-ions respectively protons, which corresponds to 66 % of their specifications. The fluence the DUTs received before failure occurred is six orders of magnitude higher with protons than with Xe-ions.

With the exception of the experiment in *GANIL* with Xe-ions, $10^7 \frac{particles}{cm^2}$ were obtained in all measurements. The minimum fluence of a particle type at which a breakdown was observed is given in the table 5.3. In these experiments the DUTs were irradiated up to at least $10^8 \frac{neutrons}{cm^2}$ and if no failure occurred up to $4 \cdot 10^{10} \frac{neutrons}{cm^2}$.

The assumption that devices do not experience failure by a single event effect below 60 %

Tab. 5.3.: Smallest measured fail fluence [$\frac{particle}{cm^2}$] for the voltage step from table 5.2 per particle kind and device type. If the device type was measured in the experiment but does not experience a failure, the maximum fluence is given in brackets. The uncertainty of the minimum failure fluence is given by the requirements for the beam, which demands a deviation of the fluence measurement of less than 10%

	Type A	**Type B**	**Type C**	**Type D**
p	1.7×10^{12}	4.6×10^{10}	7.1×10^{11}	1.7×10^{12}
$\mathbf{n_{14\,MeV}}$	3.1×10^{9}	$[1.2 \times 10^{8}]$	-	$[4.4 \times 10^{10}]$
$\mathbf{n_{atmos}}$	2.8×10^{9}	1.7×10^{10}	$[2.5 \times 10^{10}]$	6.6×10^{9}
Pb	$[6.7 \times 10^{9}]$	4.5×10^{9}	3.1×10^{8}	-
Xe	4.4×10^{4}	2.6×10^{4}	-	-

of their rated drain voltage can be confirmed within the experiments performed, for the heavy ion irradiation as well as for the neutron and proton irradiation. Especially for terrestrial applications, the experimental results indicate that all measured device types can be operated within their rated specifications. The lowest voltage at which a neutron failure was measured was 120% of the nominal V_{DS} of the DUT.

For the definition of such a safe operating voltage range, the specification of the target fluence is necessary to keep the data comparable. Within these experiments the lowest breakdown voltage during proton irradiation is above $V_{DS} > 600\,V = 100\%V_{DS}$ and necessary 10^9 particles per cm^2 (*Type B* device, all others were even higher). If this is compared with the maximum fluence required for space applications in the ESCC 25100 [11] of $10^7 \frac{Ion}{cm^2}$ there were failures obtained only with Xe-ions, i.e., the ions with the highest energy transfer of these experiments.

5.1.3. Cross Section

In the irradiation experiment with protons, failures could be detected at all measured voltage steps, even below the nominal voltage V_{DS}, while in the case of the measurement with neutrons, failures could only be detected beyond $V_{DS} > 800\,V$. However, the fluence at which these failures were detected is up to two orders of magnitude higher. The question arises whether failures also with neutrons could have been detected at lower voltage, if the fluence of up to $10^{12}\,\frac{n}{cm^2}$ would have been reached.

To compare the sensitivity at different voltages and different radiation types the cross section of a reaction (here a device failure) is considered. From the equation (3.6) the cross-section for radiation-induced SEE failures per cm^2 was calculated, differentiated by component type and applied drain stress [10, 11]:

$$\sigma = \frac{N}{\Phi} = \frac{N}{\Sigma_i n_i \Delta\phi_i} \tag{5.2}$$

Where N is the total number of failed devices, Φ the weighted fluence given by the sum over n_i the number of devices at the time of failure and $\Delta\phi_i$ the fluence at the time of failure. The occurrence of a SEE is statistically independent and for the number N the uncertainty can be determined with the χ^2 function for a required confidence level. From this the error for the cross section value is calculated as follows:

$$\begin{aligned} \Delta\sigma_{upper} &= \sqrt{\left(\frac{\chi^2_{\alpha/2}(2(N+1))}{2\Phi}\right)^2 + \left(\frac{N\cdot\Delta\Phi}{\Phi^2}\right)^2} \\ \Delta\sigma_{lower} &= \sqrt{\left(\frac{\chi^2_{\alpha/2}(2N)}{2\Phi}\right)^2 + \left(\frac{N\cdot\Delta\Phi}{\Phi^2}\right)^2} \end{aligned} \tag{5.3}$$

with $2\cdot N$ and $2\cdot(N+1)$ degrees of freedom and $\alpha = 5\,\%$ for a $95\,\%$ confidence level of the failure rate from the χ^2 function. For calculating the cross section, the uncertainty of the fluence $\Delta\phi_i$ was calculated as 10% of the measured value [10]. The calculation method for the $V_{DS} = 600\,V$ cross section of *Type A* devices is also shown as an example in the appendix in section B.

A plot of the cross sections received for the different irradiation particles, laid again the percentage of the maximum rated drain voltage V_{DS} per device type is shown in figure 5.4. In the graph the device *Type A* is shown as green dots, *Type B* as yellow triangles, *Type C* as blue stars and *Type D* as red squares. Only the filled measuring points give the absolute value of the cross section, since one or more SEE failures could be measured

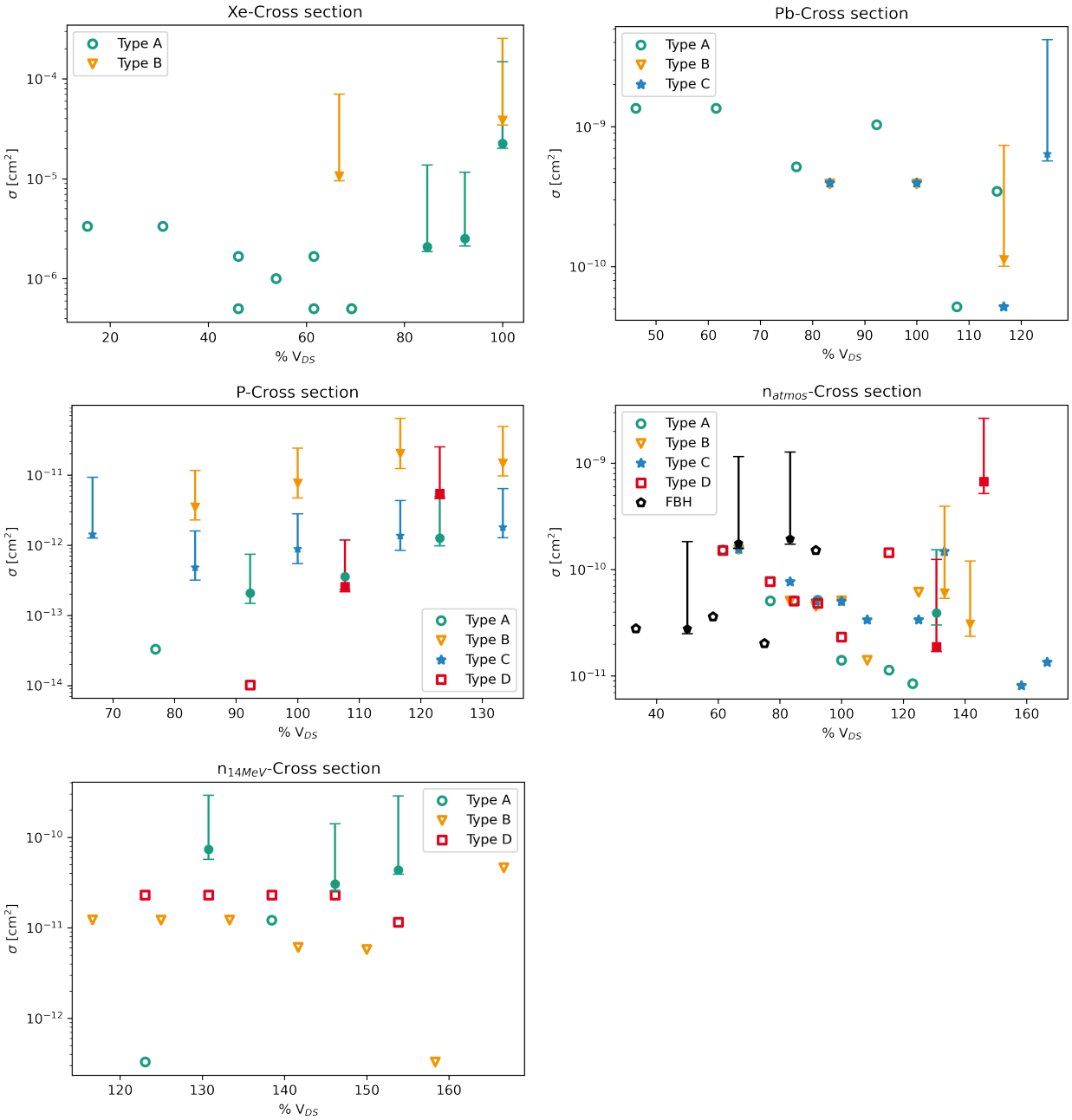

Fig. 5.4.: The results of the measurements at (right to left, top to bottom) GANIL, CHARM (CERN), OncoRay, ChipIR (ISIS) and FhG INT are plotted. The filled marker gives measured values of the cross section σ in cm^2 and the colorless marker indicate upper limits of the cross section.

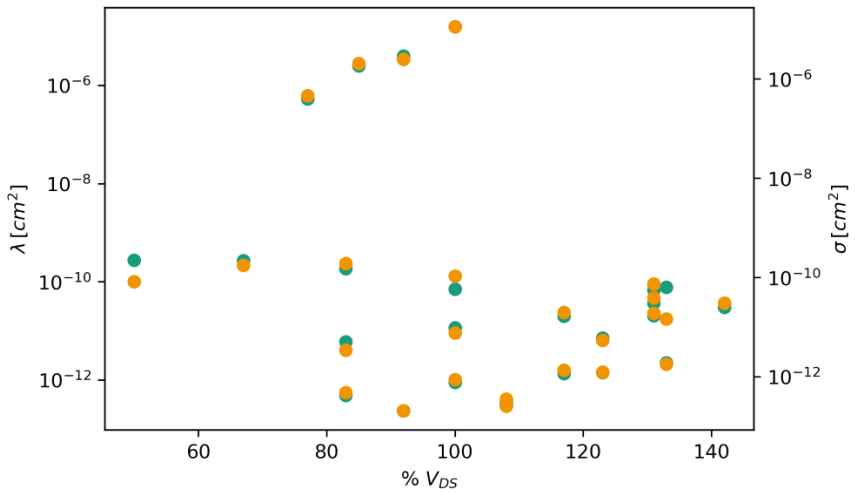

Fig. 5.5.: Plot of the calculated cross section σ $[cm^2]$ (yellow) and the fit value λ of the survival rate (green).

in these experimental steps. The unfilled measurement points show the upper limit of the cross section. To obtain the data for the upper cross section limit, an imaginary failure N=1 with the maximum fluence received was assumed and the cross section calculated. Their value depends only on the maximum fluence at which the experiment was stopped without a SEE measured.

The results of the experiment at *CHARM* (CERN) are shown in the figure at the top right. The upper limits are strongly scattered, because the differing irradiation time slots and the long time needed to enter the cave, so that the devices in the first runs were irradiated for less time (up to $4.8 \cdot 10^7 \frac{Ions}{cm^2}$) that in the second runs (up to $9.2 \cdot 10^8 \frac{Ions}{cm^2}$). Reasons for this were the given beam conditions.

One measured failure of a *Type B* device at $900\,V$ from the $14\,MeV$ neutron experiment was excluded from the data and the cross section calculation in the bottom of figure 5.4, but can be found for reference in figure A.2. The breakdown followed microseconds after switching the neutron generator on, so that the device failure could not without doubt traced back to the irradiation. Of three measured devices, only one device failed at all.

The maximum fluence is of great importance for the calculation of the cross section, as can be seen in the above example, also limits the comparison of the neutron and proton cross section. In the experiment under $200\,MeV$ proton irradiation, single event effects could also be measured below 100 % of the rated V_{DS}, but not with neutrons. However, the proton flux was considerable higher with up to $1.4 \cdot 10^9 \frac{p}{cm^2\,s}$ than that of the neutrons $3.8 \cdot 10^6 \frac{n}{cm^2\,s}$. It can be estimate that an imaginary line through the measuring points, for example of *Type A* shown in the left middle picture of figure 5.4, at $10^{-11} cm^2$ for protons will continue for higher voltages and merge into the measured cross section values with neutrons. Therefore, it is

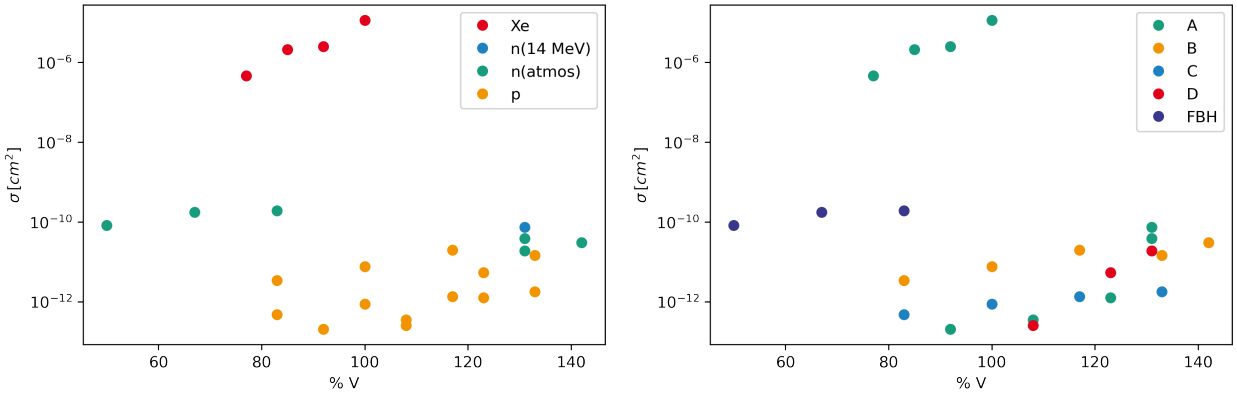

(a) sorted by facilities

(b) sorted by device type

Fig. 5.6.: Obtained cross section values sorted by facilities (a) and by device type (b). The values for the proton and neutron measurements in the right part of the graph (a) fit well with each other. The values of the Xe-ion measurements are significantly higher and the measured values of the FBH devices are not consistent with the devices *Type A-D*.

likely that if the neutron irradiation had been continued up to the same fluence/cm^2, device failures would also have occurred at lower voltages V_{DS}.

For measured failures the fit of the failure rate from 5.1.1 should correspond to the above calculated cross sections. Figure 5.5 compares the fitted λ values B.3 in green with the calculated cross section here in yellow. The data points agree well, confirming the expected distribution 3.9 function and density function 5.1 as well as the expected increasing progression to higher drain stresses.

Figure 5.6 shows the development of the cross section sorted by facilities (a) and sorted by device type (b). In the left picture sorted by facility (a), the difference of the cross section magnitude in dependence of the LET can be seen. The measured cross sections with the high LET ions Xe are up to two orders of magnitude higher than the cross sections for neutrons and protons. The difference becomes apparent if *Type A* is considered in the diagram on the right side (b). In this case, both the proton and the neutron cross sections are more than six orders of magnitude smaller than the Xe-cross sections.

The uncertainties have been intentionally omitted from the figures 5.5 and 5.6 in order to keep the graph clearer, but correspond to those shown in figure 5.4 and table B.3.

5.2. Evaluation of the Influence of the Radiation Types

5.2.1. Influence of the Linear Energy Transfer on the SEE Sensitivity

First heavy ion experiments with GaN HEMT devices indicated that the sensitivity of the devices depends on the linear energy transfer of the particles and not on the particle type itself [15]. In these studies, the dependence of the V_{DS} minimum at which failure occurred, called V_{SEE}, on the linear energy transfer was analyzed. The higher the linear energy transfer, the lower V_{SEE}, thus the more sensitive the component [18] should be. As a reaction between an incoming particle and the semiconductor crystal, the Coulomb interaction is significantly more likely than a nuclear reaction and therefore the possibility of ionization described by the LET is the main contribution when a particle interacts [12, 22].

In order to analyze this connection, the maximum ion-LET of the experiment has to be plotted against the minimum measured fail voltage V_{SEE} (table 5.2). For the ion experiments Xe and Pb the particle LET at the surface of the device are known (listed in table 3.1). These decrease when passing through different materials (DUT package, bonding wires, field plates, ...) before reaching the actual die, but with SRIM [67] simulations it could be ensured for the ion experiments that the introduced energy of the particle is large enough to reach the die, compare figure 3.1.

In experiments with neutrons and protons, however, it is difficult to determine an effective LET directly. The direct proton LET for $E(p) = 200\,MeV$ is smaller than one, approximately $0.0006\,MeV\frac{cm^2}{mg}$ [65], which is below the threshold energy required for a single event effect. Mainly the secondary products generated by the proton or neutron interaction with the semiconductor crystal trigger single event effects in the device. The resulting secondary products further contribute to ionization in the device along the particle track, with the LET generally increasing with increasing atomic number and initial energy. For the direct recoil products, a maximum secondary Z+1 can be achieved due to proton interactions. In silicon this is phosphorus and in gallium nitride this is germanium. The higher atomic number of the GaN lattice results in a different distribution of recoil products than in Si showing a peak around the elastic recoil for Ga ($Z = 31$) and N ($Z = 7$) in gallium nitride crystals and Si ($Z = 14$) for silicon crystals.

The LET distribution of secondary products has been calculated in various publications for different energies [65, 66, 99]. In figure 5.7 calculated LET-distributions of the secondary particles are shown for proton, an atmospheric neutron spectrum irradiation in GaN crystals as well as for different neutron energies, including spallation spectra, in Si crystals.

For interactions between $200\,MeV$ proton and GaN, the maximum LET of the secondary products produced is $13\,MeV\frac{cm^2}{mg}$ and peaks about $4\,MeV\frac{cm^2}{mg}$ (turquoise line)[65].

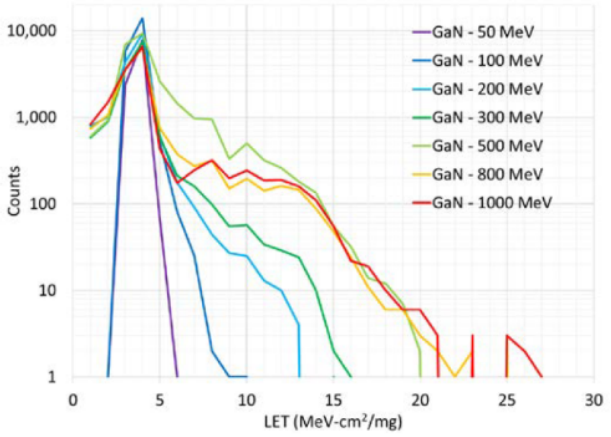

(a) Protons in GaN crystal

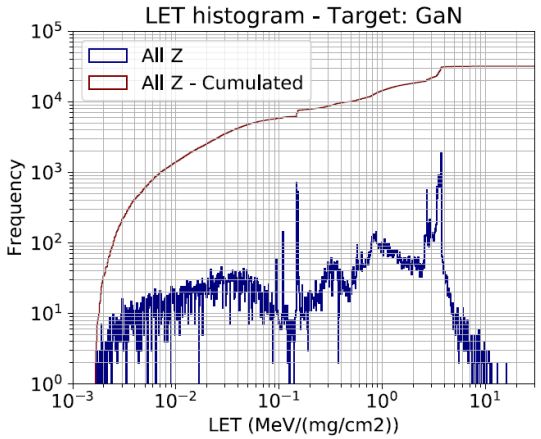

(b) Neutron spectrum in GaN crystal

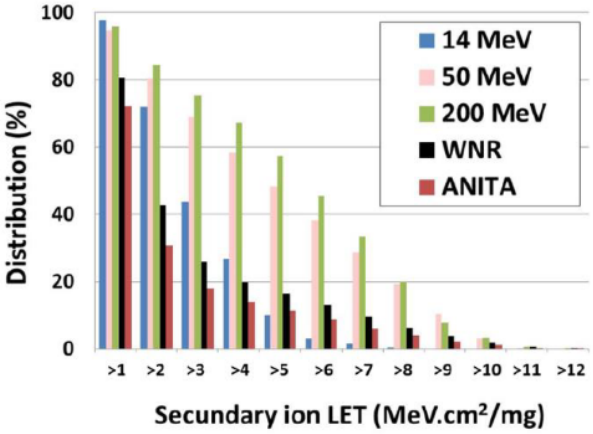

(c) Neutrons different energies in Si crystal

Fig. 5.7.: Calculated LET distribution secondary products for protons and neutrons different energies. (a) incident protons with different energies in GaN [65]. (b) Incident atmospheric like neutron spectrum in GaN [66]. (c) Incident different neutron energies in Si [99].

With the atmospherically distributed neutrons, the peak is at about 2.7 $MeV\frac{cm^2}{mg}$ and maximum 12 $MeV\frac{cm^2}{mg}$ [66]. And 14 MeV-neutrons gives a LET peak of the secondary products less than 1 $MeV\frac{cm^2}{mg}$ and decreases to higher LET values. The maximum transferred LET is here at about 9 $MeV\frac{cm^2}{mg}$ [99].

The actual distribution within a device depends not only on the material of the semiconductor crystal, but also on the surrounding materials, which differ from manufacturer to manufacturer and no precise information is available which is a limitation in terms of comparability. Despite this it can be estimated from the given distributions that only less than 10% of the reaction products have a LET of 7 $MeV\frac{cm^2}{mg}$ or higher, but the proportion beyond the peaks cannot be neglected and also have a significant contribution to the amount of recoil products and thus statistically also to the single event effects.

The estimation of an effective LET, which is at about 10% probability of occurrence,

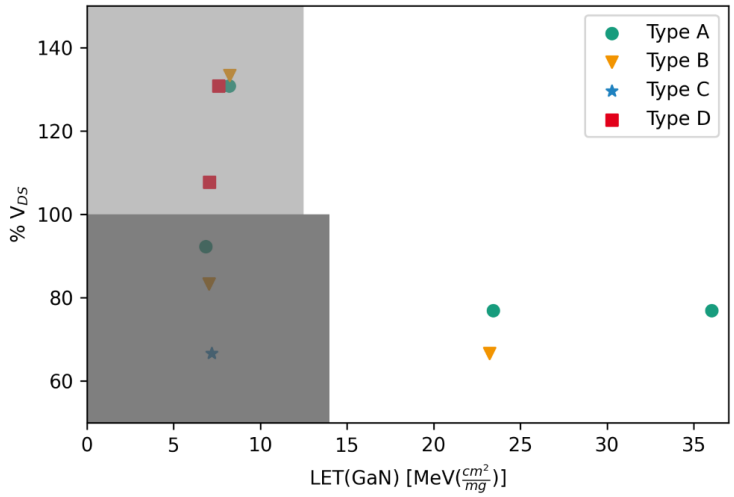

Fig. 5.8.: Smallest measured V_{DS} at which a SEE occurred in percent of the device rated Voltage plotted against the particle LET. The shaded areas indicate the LET range of the secondary products for neutrons (light gray) and protons (dark gray).

was used for further consideration. These were estimated with $LET(n_{atmos})$=7.9 $MeV\frac{cm^2}{mg}$, $LET(n_{14_{MeV}})$=8 $MeV\frac{cm^2}{mg}$ and $LET(p)$=7 $MeV\frac{cm^2}{mg}$.

In figure 5.8 the LET in gallium nitride versus minimum fail voltage V_{SEE} is plotted. The data from the measurements is shown as filled markers as *Type A* (green, point), *Type B* (yellow, triangle), *Type C* (blue, star) and *Type D* (red, square). In order to take the wide LET distribution for protons and neutrons into account and still obtain an estimate of the sensitivity as a function of the LET, the possible LET range is shaded in dark gray for the proton LET, and gray for the neutron LET.

For the values there is also an uncertainty in the voltage applied by the SMU which is to small too be reproduced in this graph in terms of magnitude. Due to the similar interactions of protons and neutrons with GaN, especially with high energy particles, it can be assumed that in the experiment with neutrons also smaller V_{SEE} values could have been reached, if the irradiation had been accomplished up to higher fluences per device. For the proton measurements $10^{12}\frac{p}{cm^2}$ have been reached, with neutrons only $10^{10}\frac{n}{cm^2}$ maximum. It can be expected that the points above 100% in the left part of figure 5.8 would have approached the lower ones. However, the correlation between LET and fail voltage can also be established in the data from these experiments in the sense that the maximum drain voltage, which can be safely applied, reduces, apparently exponentially, with increasing LET. The higher the ionization introduced by a particle, the smaller the applied field in the device could be in order to have more buffer available for the introduced energy.

Another way to characterize the LET dependence on SEE sensitivity of a device is over the measured cross section. The sensitive volume of a device is determined on the basis of the

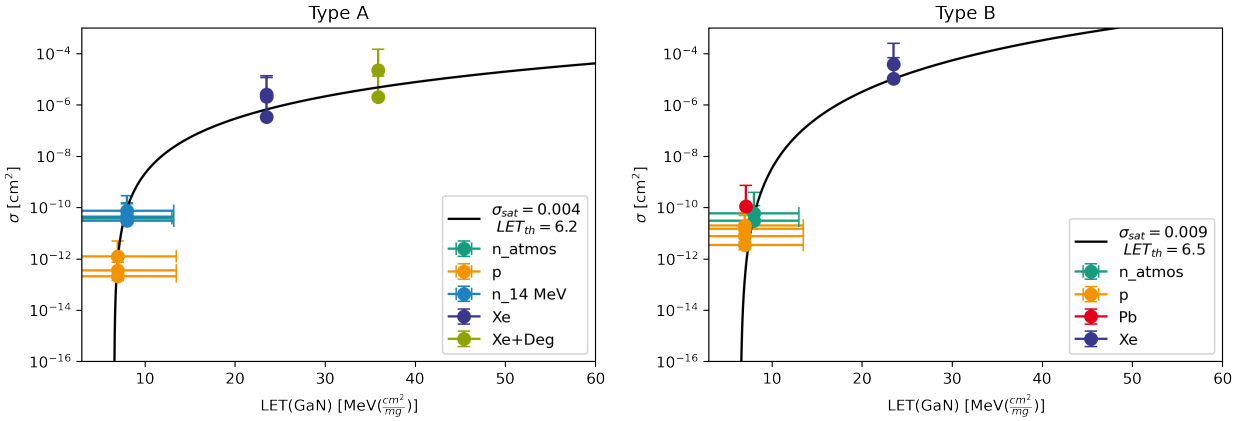

Fig. 5.9.: Plot of the measured cross sections against the LET of the incident particle. A four parameter Weibull curve is fitted to the measured values, which gives the saturation cross section σ_{sat} and the threshold LET_{th}.

measured cross sections and known LET values from realized experiments and fitted with a four parameter Weibull function. The function gives the saturation of the effective cross section and the threshold LET as parameter of the fit.

$$F(LET) = \sigma_{sat}(1 - e^{-(\frac{LET - LET_{th}}{W})^S}) \tag{5.4}$$

where LET_{th} is the device specific reaction threshold, W is the width parameter and S is the shape parameter. This function is with σ_{sat} normalized to the limiting cross section of the device [63].

To obtain the best possible information from the function for the presumed behavior of the device, it is necessary to measure both the saturation cross-section and the threshold LET directly and with each additional value the prediction reliability improves. It was not possible to measure the saturation cross section directly, as only ions with the maximum LET of 36 $MeV\frac{cm^2}{mg}(GaN)$ were available. However, the measurement at *CHARM* (CERN) set a plausible threshold LET of 7 $MeV\frac{cm^2}{mg}(GaN)$ at the DUT surface up to a drain voltage of 700 V.

Figure 5.9 shows the measured cross sections, plotted against the LET and fitted with the Weibull-function (5.4).

Averaging the function fit over all voltage steps increases the inaccuracy of the fit, in addition to the uncertainty of the cross section and the LET values. The parameters σ_{sat}, LET_{th}, W and S are listed in table 5.4.

The received results are within the expected range for the saturation cross section and the threshold LET. σ_{sat} can be used to estimate the maximum expected cross section and the LET_{th} gives us an indication of the minimum energy required to trigger a SEE. The

Tab. 5.4.: Parameters obtained for the four parameter Weibull-function on the measured cross section, and for comparison the die size as maximum sensitive area (the other fit parameters W and S are listed in the appendix in table B.2)

Type	$\sigma_{sat}[cm^2]$	LET_{th}	die surface $[cm^2]$
Type A	$(4.71 \pm 6.6) \cdot 10^{-3}$	6.17 ± 6	0.03 ± 0.005
Type B	$(9.06 \pm 1.4) \cdot 10^{-3}$	6.50 ± 9	0.04 ± 0.004

maximum measured cross section for *Type A* devices was $(2.3 \pm 0.2) \cdot 10^{-5}\, cm^2$ and for *Type B* devices $(3.8 \pm 0.4) \cdot 10^{-5}\, cm^2$ in this work, both below the assumed maximum from the fit. The fact that the saturation cross section is by a factor of two to four smaller than the absolute physical dimension of the die is due to the fact that normally only a part of the device is sensitive to single event effects. For example, the structures at gate, source or drain. The LET_{th} resulting from the fit matches the experience during the experiments. Within the measurements at *CHARM* (CERN) with high-energy lead ions and an LET of under $7.1\, MeV\frac{cm^2}{mg}(GaN)$ (table 3.1), no SEE could be measured for these two device types. From the saturation of the Weibull-curve it can be assume that above an LET of approximately $70\, MeV\frac{cm^2}{mg}$ the SEE rate will probably no longer increase with the energy.

5.2.2. Comparison between Proton and Neutron Irradiation

For terrestrial applications, the atmospheric spectrum is crucial and thus the interaction with neutrons predominates. To test devices for their sensitivity to terrestrial neutrons, a spallation source is the first choice. Due to the similarity of neutron creation to the process in the atmosphere, the spectrum is almost similar in distribution and can also reach several hundred MeV energy [28]. But access to a spallation sources is generally limited by the small number of facilities. Different approaches have been taken in the past to circumvent the bottleneck of irradiation possibilities and to obtain the failure rate for terrestrial applications through other types of irradiation. One of the most promising approaches is irradiation with monoenergetic neutrons or protons instead of the neutron spectrum.

The *JEDEC-JEP 151* standard defines as a substitute for atmospheric like neutron tests measurements with $150\,MeV$ or higher energy protons. With that the statement is made that this overestimates the error rate for Si devices [10]. The use of high-energy protons is derived from the interaction similarity for high-energy protons and neutrons with matter, and that high energy neutrons have main contribution to the single event rate in devices in contrast to low-energy neutrons. However below around $50\,MeV$ nucleon energy, the interaction between neutrons and protons is no longer comparable, since the Coulomb interaction dominates for the protons.

Alternatively, the uses of monoenergetic $14\,MeV$ neutrons to determine the SEE rate have been studied since the early 2000s. For small technologies such as SRAMs and specific single event effects, like SEUs, they have proven to be a suitable substitute for testing with a spallation source. [99]. Single event burnouts were also observed under $14\,MeV$ neutron irradiation, but the measured cross section did not match the cross section of the spallation source. In the observed measurements, the difference became up to two orders of magnitude larger with the derating V_{DS} of the device [100].

In order to realize a comparable cross section with other nuclides, the depositable energy must be similar. Since neutrons do not interact via charge interactions, the main contribution comes from direct collisions and nuclear reactions. Suitable substitute nuclides should therefore have a similar interaction spectrum, therefore protons and monoenergetic neutrons are of interest. Several publications have simulated the possible secondary product for protons and neutrons both in Si and GaN crystals [6, 20, 28, 65, 66, 79, 99]. In particular, the secondary products produced and their energy distribution were investigated. The found atomic number distribution of secondary products and abundance for interactions between protons and GaN, neutrons with an atmospheric like energy distribution and GaN as well as neutrons of different energies with Si are shown in figure 5.10.

The interaction between protons of different energies in GaN can be seen in the upper left

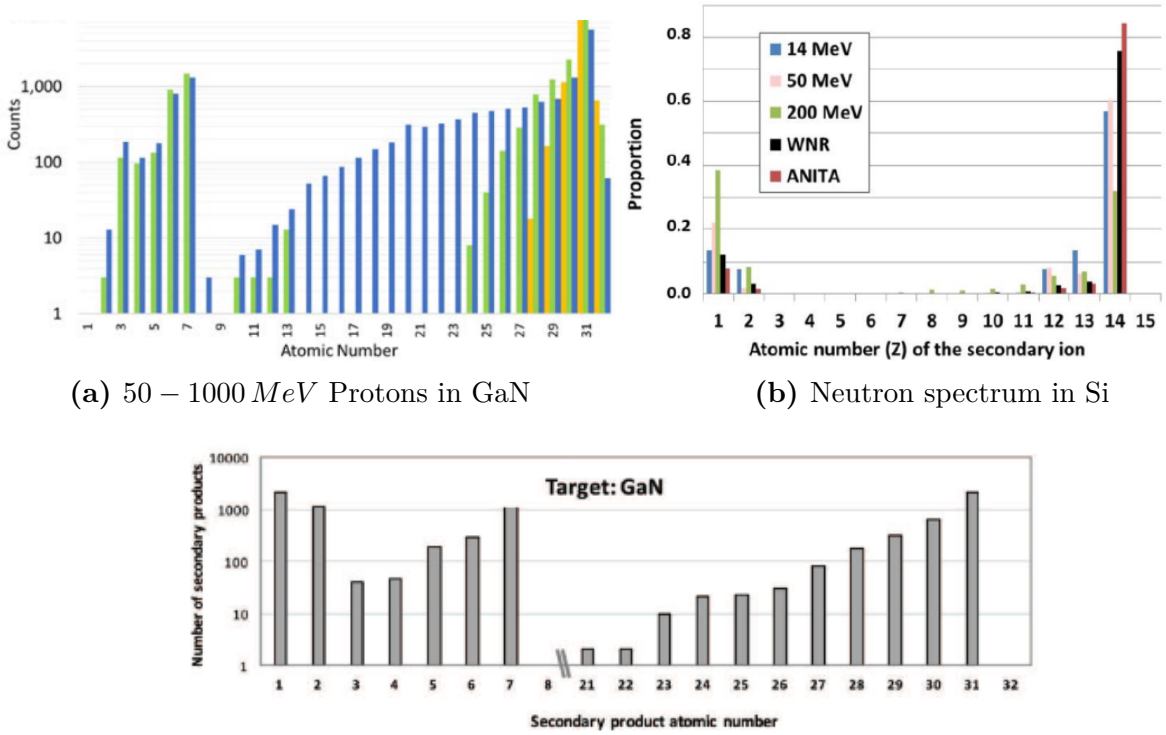

(a) $50 - 1000\,MeV$ Protons in GaN

(b) Neutron spectrum in Si

(c) Neutron Spectrum in GaN

Fig. 5.10.: Secondary particles produced by (a) $50\,MeV$ (yellow), $200\,MeV$ (green) and $1000\,MeV$ (blue) protons in an AlGaN/GaN stack [65]. (b) neutrons with different energies in Si [99] (c) atmospheric like neutron spectrum in GaN [68].

panel. Yellow refers to $50\,MeV$, green to $200\,MeV$ and blue to $1000\,MeV$ protons [65]. At the right panel, neutron interaction has been simulated in Si for different neutron energies, including $14\,MeV$ neutrons, monoenergetic neutrons and spallation neutrons from the *WNR at LANSCE* (USA) [74] and *ANITA at TSL* (Sweden) [101] facilities [99]. The lower part of the figure shows the secondary products produced by interactions between GaN and neutrons with an atmospheric like energy distribution [68]. Comparing the resulting secondary products, an alike distribution between neutron and proton excitation can be observed. Excited crystal nuclei (Ga ($Z = 31$) and N ($Z = 7$), as well as Si ($Z = 14$)) have the largest share, followed by the nucleons deuterium, tritium ($Z = 1$) and alpha particles ($Z = 2$), the rest is distributed among other nuclides around the crystal atoms. Comparing the neutron simulations between Si and GaN (5.10 upper right and lower panel), the ratio of the produced recoil atoms to the nuclides has shifted towards $Z = 1$ and $Z = 2$ due to a larger cross section for $^{14}N(n,p)^{14}C$ and $^{14}N(n,\alpha)^{11}B$ reactions in GaN [20].

The additional recoil products shown at the proton interactions (figure 5.10a) between $Z = 10 - 13$ are distributed around Al ($Z = 13$), from an AlGaN layer in HEMT devices which was not included in the simulation of the neutrons. Due to the otherwise similar

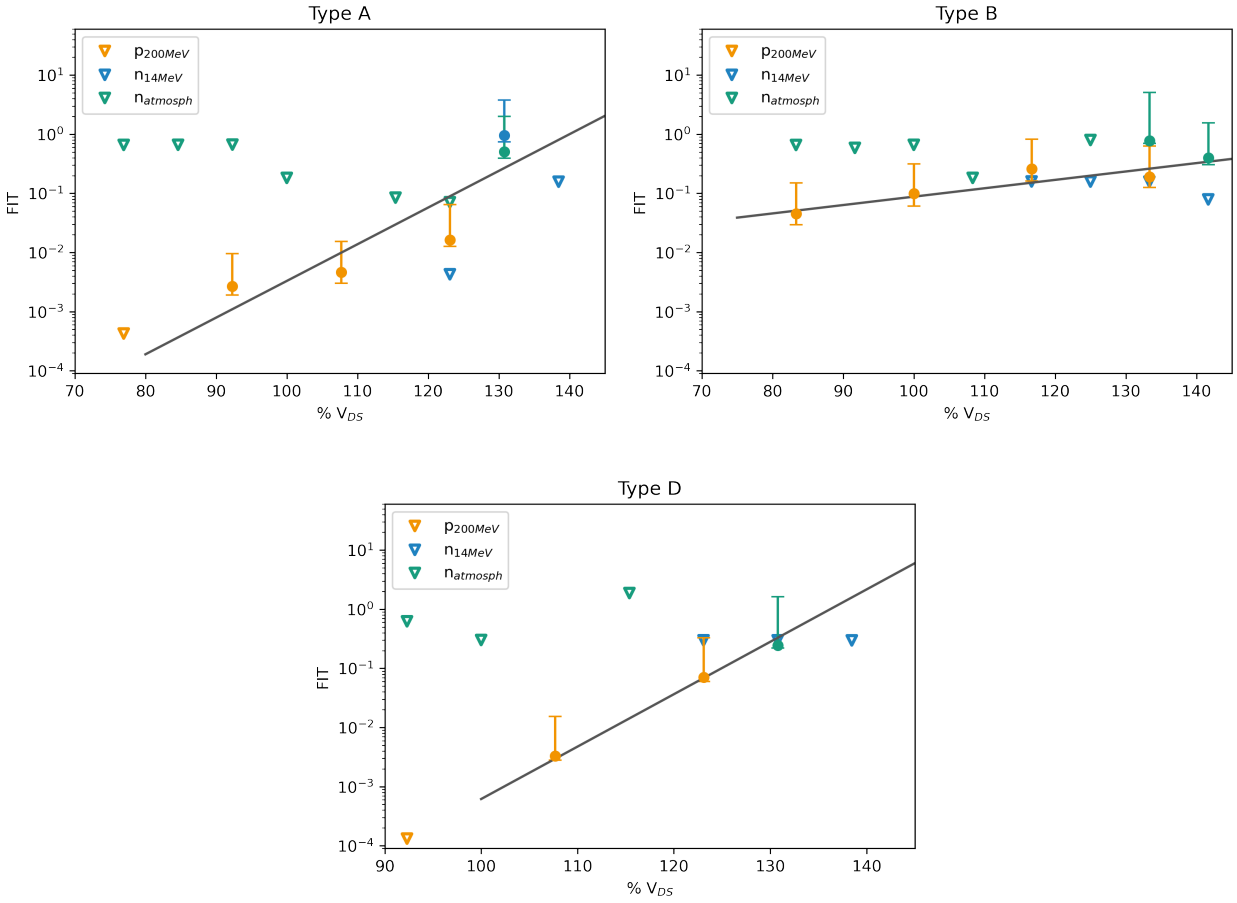

Fig. 5.11.: Logarithmic plotted Failure In Time rate from the neutron and proton experiments shown for each device type separately. *Type C* is excluded, as device failures were only seen in the proton experiment. An exponential function was plotted as an optical guideline.

distribution of the secondary products and thus of the depositable energy, experiments should be carried out to determine whether the failure rate can be derived with sufficient certainty from 14 MeV neutron or high energy proton experiments.

For terrestrial applications, the breakdown rate is most of the time given as Failure In Time (FIT). In the case of radiation damage, it is proportional to the cross section, normalized to the normalized to the average number of cosmic neutrons at sea level in New York. The FIT rate gives the number of failures after 10^9 operating hours, this means an average lifetime of about 120000 years before a SEE in the device occurs. Average reliability FIT rates for silicon power devices lay between 0.01 and 10 FIT [12]. The Failure In Time rate corresponding to terrestrial applications follows from

$$\lambda_{CR} = \lambda \cdot \Phi_{NY} \tag{5.5}$$

with Φ_{NY} refers to the neutron flux from terrestrial cosmic radiation at sea level in New York. The uncertainty interval error bar is estimated like for the cross section via the χ^2-function for the number of measured failures and the uncertainty for determining the fluence [10].
The data points obtained with equation (5.5) were plotted against the applied drain voltage V_{DS} for each device type and are shown in figure 5.11. Filled points with error bars represent actual measured FIT values, triangles without filling indicate measured upper limits of the data. The data of the proton measurements are shown in yellow, those of the $14\,MeV$ neutron irradiation in blue and the results of the measurements with the spallation neutron spectrum in green.
Due to the low failure rate with neutrons below $850\,V$ and the distinct intensity of the proton interaction, only two overlapping cross section values for *Type A*, one for *Type B* an none for *Type D* devices could be acquired. The *Type C* device show no failures under neutron irradiation up to $1000\,V$ and a fluence of about $10^{10}\,\frac{n}{cm^2}$. As a visual aid, an exponential function was plotted in the graph, which has no direct physical meaning in connection with the processes taking place within the device, but only represents the increasing sensitivity with increasing the stress V_{DS}.
It should be emphasized that the cross section of $200\,MeV$ proton irradiation tends to underestimate the expected neutron cross section and not overestimate it as expected for silicon devices in *JEDEC-JEP 151* [10].

5.3. Other Configuration Effects

5.3.1. Failure Mechanism

Two different possible current patterns after a SEE have been described in recent publications. Both were evident in the response of the gate and drain leakage current I_{DS}, I_{GS}. The different current forms indicate two different mechanisms that lead to failure. The simultaneous increase in drain and gate leakage current (I_{DS} and I_{GS}) was observed, and second an increase in drain leakage current but a decrease in gate leakage current. These two different current characteristics were first described in 2013 for high-frequency normally-on GaN HEMTs up to $300\,V$ [19], and some years later also for $600\,V$ normally-off devices of the p-layer gate design [61].

In the first case, a short circuit occurs between the drain and the silicon substrate of the device along the particle path. This is evidenced by the decrease in gate leakage current I_{GS}. An ionized conductive path is formed from the drain through the GaN layers to the substrate. Examination of the devices showed that the GaN-, buffer- and Si-layers were damaged. For this to happen, a particle must presumably arrive perpendicular to the device surface [61].

Within the second observed effect I_{GS} remained the same or increased and in addition the ohmic behavior of the devices changed. In the gate area, a burnout mark could be seen for non-enclosed components. These facts indicate that a short circuit between source and drain has occurred and the gate-channel junction has been destroyed [61]. For particles arriving parallel to the surface of the device, this failure mechanism was more frequently observed in the former studies.

During the experiments for this work, both failure mechanisms were observed for the *Type A*, *Type B* and *FBH* devices. In all experiments and for all device types, the setup was with the particle beam aligned perpendicular to the DUT surface.

Tab. 5.5.: Overview of the percentage appearance of the error mechanisms. *Sou* stands for the short circuit between drain and source, *sub* for the short circuit between drain and substrate of the device.

	Type A		Type B		Type C		FBH	
	sou	sub	sou	sub	sou	sub	sou	sub
Xe	100 %		100 %					
p($200\,MeV$)	18 %	82 %	68 %	32 %	91 %	9 %		
n_{atmos}	20 %	80 %	100 %				75 %	25 %
n($14\,MeV$)	67 %	33 %						

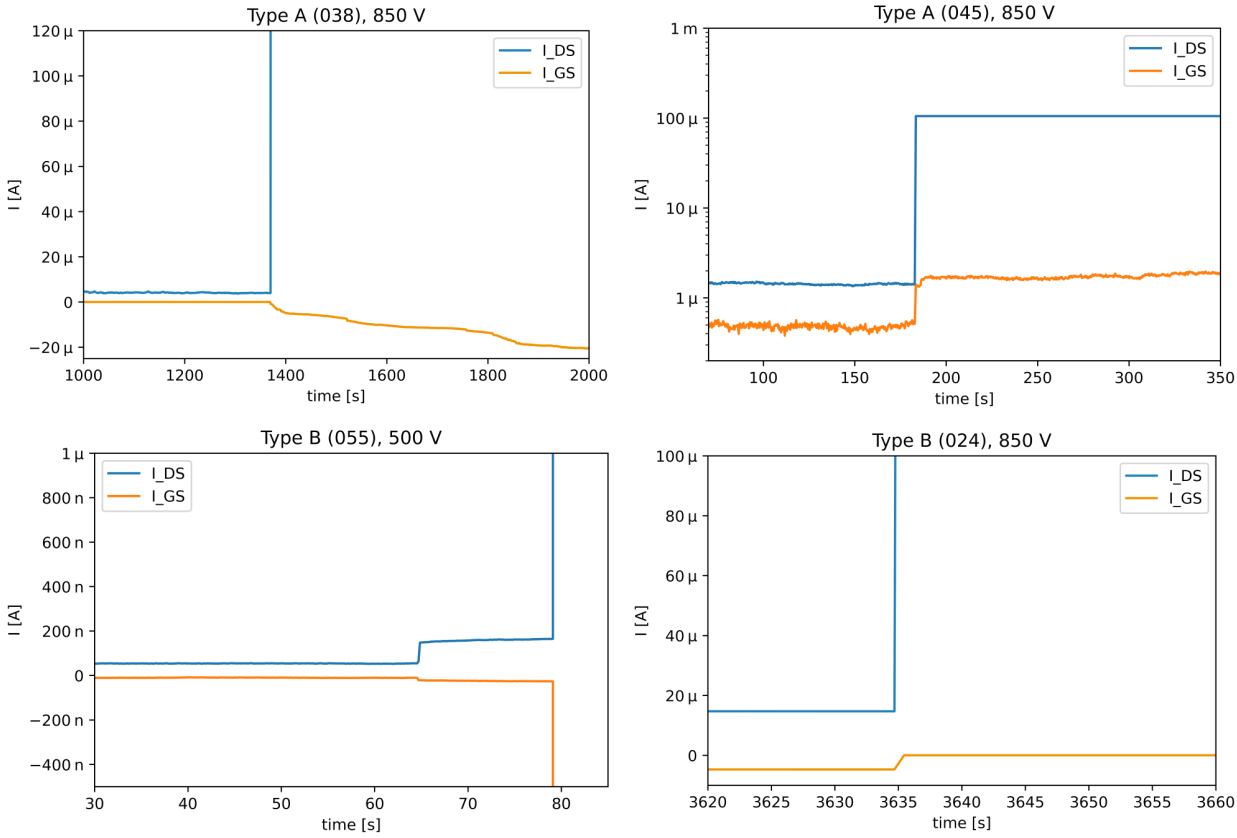

Fig. 5.12.: Plot of drain (blue) and gate (orange) leakage currents at the time of a destructive failure in *Type A* and *Type B* devices, measured with spallation neutrons at ChipIR.

A difference in the frequency with which the error mechanisms occur depending on the irradiation source can be observed. The current characteristics I_{DS} and I_{GS} of four DUTs (*Type A*: DUT 38 and DUT 45, *Type B*: DUT 24 and DUT 55) are shown in figure 5.12 as an example and the percentage of the failure mechanism occurrence per type and irradiation source is listed in table 5.5.

Under irradiation with Xe-ions at *GANIL* in 100% of the measurements the gate leakage current was constant for both gallium nitride devices and stayed level after the SEE.

For *Type B*, I_{GS} was also constant or increasing under neutron irradiation (14 MeV neutrons as well as with the neutron spectrum) in 100% of the measured failures. Only under high energy proton irradiation this device type showed the shortage between drain and substrate. In contrast the measured *Type A* devices in the experiment at *ChipIR* I_{GS} was only 20% increasing but 80% decreasing after SEE and the measurement with protons showed the inverted ratio of error mechanisms. Contrary with the monoenergetic 14 MeV neutrons a greater proportion of source-drain short circuits were detected.

For the FBH devices which were irradiated with neutrons of the spallation source at *ChipIR* only, both leakage paths could be detected during the irradiation. After the experiment, the

devices were analyzed microscopically and electrically by the FBH and the results discussed [90]. The devices for which the I_{GS} had also increased showed a degeneration of the p-gate, which supports the theory of a short circuit between drain and source[83].

5.3.2. Gate Voltage

In silicon MOSFETs, a strong negative biased gate is known to be the worst case test scenario for single event effect testing [61, 15]. Reason for this is that in that case the gate oxide is already stressed due to the large field such that the sensitivity for single event gate rupture (SEGR) increases. Since the gallium nitride high electron mobility transistors are lateral devices and do not have a gate oxide, the influence of the gate voltage at the single event effect sensitivity is not clear.
In order to investigate the influence of the gate stress, the devices were irradiated with the same drain voltage up to the same target fluence both with unbiased gate and with negative biased gate during the first experiments carried out, at *GANIL* with Xe-ions and at *ChipIR* with spallation neutrons. The voltages applied to the gate were based on the manufacturer's recommendations and reaches from -18 to $-4\,V$. The applied gate voltages are listed in table 5.6.
The measured cross section from these setup biases is shown in figure 5.13, where the data acquired with unbiased gate are plotted in color and the data acquired with negative biased gate are plotted in gray. The cross section is shown as filled data points and the measured upper limits as unfilled data points if no error occurred. The data below $600\,V$ are from the *GANIL* Xe-ion measurement and the data above $600\,V$ are from the *ChipIR* measurement with neutrons.

Tab. 5.6.: Applied gate voltage V_G for the biased measurements. The voltages are based on the manufacturer's recommendations.

Device	**Voltage**
Type A	$-10\,V$
Type B	$-10\,V$
Type C	$-18\,V$
Type D	$-4\,V$

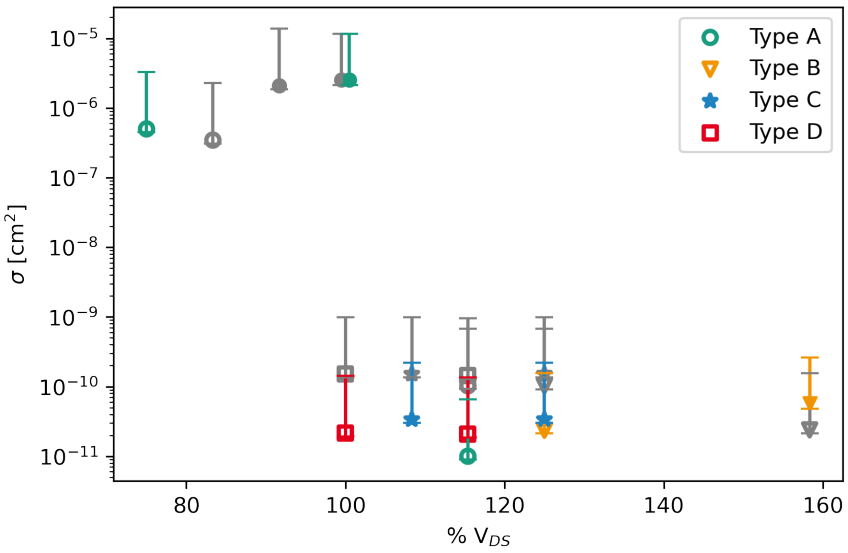

Fig. 5.13.: Plot of the measured cross section data with unbiased gate ($V_{GS} = 0$: colored) and negative gate bias ($V_{GS} < 0$: gray). Data from the experiments with Xe-ions ($600\,V$ and below) and spallation neutrons ($600\,V$ and above) are shown. The filled data points denote measured failures, unfilled data points denote an upper limit of the cross section.

A small difference between the data points from the biased and unbiased measurements can be observed. With the neutron irradiation (lower cross sections), the measured results with a negatively biased gate (gray) tend to be slightly higher than those with an unbiased gate (colored). With the Xe-ion irradiation (higher cross sections) they are slightly lower. It should be noted that most of these values are to be regarded as upper limit values (unfilled markers). Within the error limits, which mainly result from the small number of items, there is therefore no significant difference between the failure rate with biased or unbiased gate.

6. Discussion and Outlook

In this work, the radiation sensitivity in normally off gallium nitride high electron mobility transistors rated up to $650\,V$ was investigated. The focus was on neutron-induced effects from terrestrial radiation environments.
To set the foundations the first part of the thesis addresses the basics of the technology, radiation effects in electronic devices in general and the specific features of the unusual lateral structure and functionality of the GaN HEMT in particular. As types of components have only been on the market since the early 2010s for lower voltages and for higher drain voltages years later, the radiation sensitivity of these devices has yet been investigated in a few studies. The different radiation effects of particles in matter were discussed and radiation environments were described in chapter 2.
In the following, the variety of possible test procedures for Si devices and the corresponding standards were briefly described, as well as the advantages and disadvantages of irradiation tests possibilities. These were adapted for terrestrial application with wide bandgap devices and an approach for radiation tests and the experimental set up was planned.
For the experiments, more than 190 DUTs of three different, freely available GaN normally off transistors were bought to investigate them under equal experimental conditions in different accelerator facilities in order to obtain a large number of comparable experiments. In addition, SiC MOSFETs were measured with this experimental setup to compare the technology.
Based on varying circumstances, it was not always possible to measure all device types at the same facilities or at the same (voltage-) conditions. Due to ordering issues, only two component types (*Type A*, *Type B*) were available for the first experiment in *GANIL*. It also became clear very quickly how differently the various technologies reacted to the irradiation, so that the *Type C* devices failures could only be measured with charged particles. However, the experimental setup and measured parameters were maintained for all experiments.
It was possible to run measurements of the devices at five different facilities with the chosen experimental set up. In chronological order these were Xe-ions at *GANIL* (France), atmospherically distributed spallation neutrons at *ChipIR* ISIS (United Kingdom), Pb-ions at *CHARM* in CERN (Switzerland), $14\,MeV$ neutrons at Fraunhofer INT (Germany) and $200\,MeV$ protons at *OncoRay* (Germany).

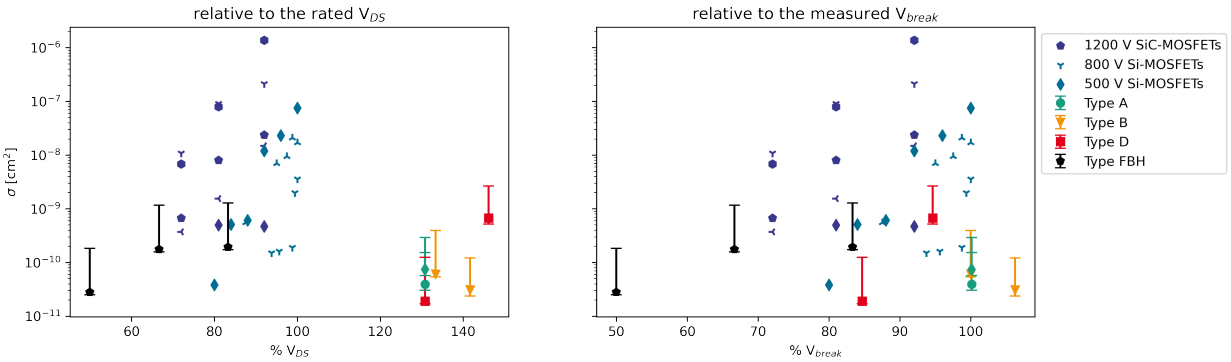

Fig. 6.1.: Cross section-results from the neutron experiments realized, compared to the results for SiC MOSFETs ($1200\,V$) irradiated also with neutrons at ChipIR from [102] in violet, different point-shapes stand for different DUTs, and Si MOSFETs from [103] where the blue crosses stand for $800\,V$ rated DUTs and the blue diamonds for $500\,V$ rated DUTs. The normalization to the measured breakdown voltage (table 4.1) relativizes the voltage dependence but not the effective cross section.

As first outcome the survival rate results of the devices in this work largely meet expectations. The found variations can be explained by the small statistical number of failed devices. It would have been preferable to be able to measure the same number of failures in all irradiation steps, but the sometimes very long irradiation time per measured failure and the fact that a maximum of three DUTs could be irradiated at the same time made this impossible.

The measured single event effects were all above 60 % of the rated drain voltage and at fluences above $4.4 \cdot 10^4$ ions/cm^2 for ions and $3 \cdot 10^9$ particles/cm^2 for protons or neutrons. For irradiation with neutrons, the SOA was over 130 % rated V_{DS}. This emphasizes the effect that a large applied field enhances the SEE sensitivity and that the response increases with increasing drain voltage.

The measured cross sections range between $2 \times 10^{-13}\,cm^2$ (protons) and $4 \times 10^{-5}\,cm^2$ (Xe-ions), respectively between 3×10^{-3} and 5×10^5 FIT at higher drain stresses and thus appear significantly more robust than comparable Si or SiC components. The left part of figure 6.1 shows the neutron-induced device failures measured in this work plotted against the normalized drain voltage. For comparison, the measured values of several different commercial SiC MOSFETs rated for $1200\,V$ (from [102]) are shown in purple. Each marker shape represents a device model. These SiC MOSFETs were irradiated at the same facility with the same neutron spectrum as in this work. Also shown in blue are Si MOSFETs (from [103]), which were irradiated with neutrons from fission reactions as well as monoenergetic $3\,MeV$ neutrons and were rated for $500 - 800\,V$. This figure reveals that the cross sections of the GaN HEMTs are on average below those of Si and SiC MOSFETs, and also that the commercial GaN devices showed failures only at drain voltages well above the rated voltage.

Tab. 6.1.: Smallest V_{DS} at which a device failure was measured, given in percent of the devices rated voltage (gray) and percent of the devices measured breakdown voltage (black).

Ion/	**p**		**$n_{14\,MeV}$**		**n_{atmos}**		**Pb**		**Xe**	
Device	$V(r)$	$V(m)$	$V(r)$	$V(m)$	$V(r)$	$V(m)$	$V(r)$	$V(m)$	$V(r)$	$V(m)$
Type A	92 %	71 %	131 %	100 %	131 %	100 %	[108 %]	[82 %]	77 %	59 %
Type B	83 %	63 %	[155 %]	[116 %]	133 %	100 %	117 %	88 %	67 %	50 %
Type C	67 %	28 %	-	-	[167 %]	[70 %]	125 %	53 %	-	-
Type D	108 %	70 %	[154 %]	[100 %]	131 %	[80 %]	-	-	-	-

The large bandgap and the field stability of the crystal are arguments for less sensitivity towards radiation, on the other hand, the lattice structure of the gallium nitride crystal has more atoms than a simple Si crystal and thus more potential for interactions and secondary products. In the paper [20], a more than one and a half times higher interaction rate was simulated. The secondary products generated bring further possibilities for ionization into the crystal, so that the advantage of the wider bandgap may be canceled out.

In the experiments with neutrons, no breakdowns within the device specifications could be measured. The lowest voltage a SEE was measured due to neutrons was at more than 120% of the designated drain voltage. Nevertheless, gallium nitride is relatively new to transistor development and a difficult material for wafer fabrication, there have been problems with impurities within the wafer material [83, 45]. It can therefore be assumed that the manufacturers provide a large safety margin in the specification of their commercial devices in order to avoid possible technological problems. Si MOSFETs, for example, a well-established technology, are therefore rated much closer to the technology limits. In the prior measurements before the irradiation, the breakdown voltage of the three GaN device types was beyond $900\,V$ without irradiation. Therefore, the evaluation of the sensitivity change due down rating must be viewed with caution, since it appears that the manufacturers have already implemented this. In order to avoid this bias, the data from the experiments were normalized to the measured, type-specific, breakdown voltage and given in table 6.1. This significantly relativizes the difference in the 'Safe Operating Area' compared to Si device failure rates.

For the Failure In Time rate, and thus also for the proportional cross section, compared with other FIT data from the literature [104, 105] in figure 6.2 the failure rates of GaN and Si/SiC devices converge, the GaN data stays below the lower middle range and are thus comparatively more stable for terrestrial SEE.

The dependence of the minimal Voltage on which a SEE occurs on the LET postulated by [18] and [15] can be confirmed by the measurements in chapter 5.2.1. The higher the energy

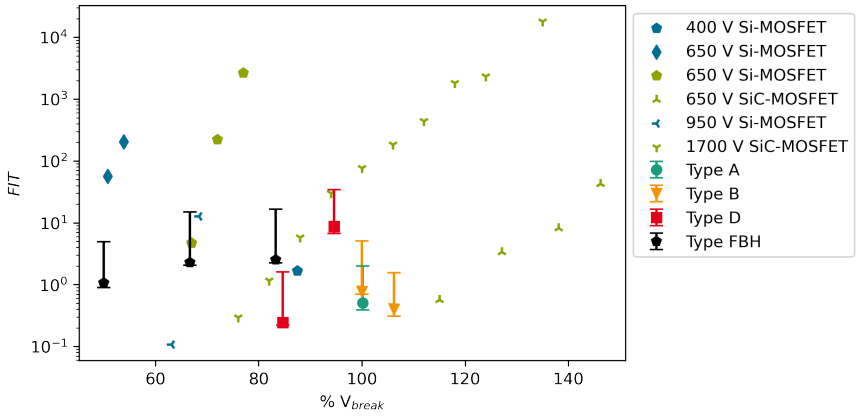

Fig. 6.2.: Experimental results relative to the measured breakdown voltage in comparison with 650 V Si MOSFETs (green pentagram), 1700 V and 600 V SiC MOSFETs measured with an neutron spectrum (green) from [104] and Si MOSFETs (blue) [105] measured at ChipIR.

introduced by the incident particle into the device structure, the lower the external applied field can be to prevent the breakdown. In three out of five experiments the incident particles have only a very small direct LET, their interaction probability with the target material and possible secondary product generation can be used to estimate a relative LET depending on the secondary products and their energy distribution using the recently published simulations of [99, 20, 65].

To simplify the practicability of radiation tests for terrestrial applications and reduce necessity of spallation sources, protons with an energy above 150 MeV have been required so far [10]. Also, the use of 14 MeV neutrons has been proposed, with the argument that the SEE rates can be correctly estimated using these replacement particles. Although the above-mentioned simulations show a similar distribution of secondary particles, no overlapping measured values could be obtained in this work, so that it is not possible to make a conclusive statement about those. The assumption from [10] that with high energy protons the effective cross section is overestimated is not supported for GaN devices by the measured values. In this work (chapter 5.2.2), the effective cross section of the protons in the only overlapping voltage range at 800 V is between $10^{-11}\,cm^2$ and $10^{-12}\,cm^2$ and that of the neutron measurement is between $10^{-10}\,cm^2$ and $10^{-11}\,cm^2$. At lower voltages, only upper limit values were measured with neutrons, which depend solely on the applied fluence. The reason for that was the available measurement time. Considering figure 6.3 (repeated presentation of figure 5.11), in which only actually derived FIT-values are shown, it looks as if it is possible to extrapolate from the SEE rates of one particle to the SEE rates of the other particle type within certain margins of error. However, in order to be able to evaluate this completely, further measurements have to be made in which the targeted voltage range overlaps.

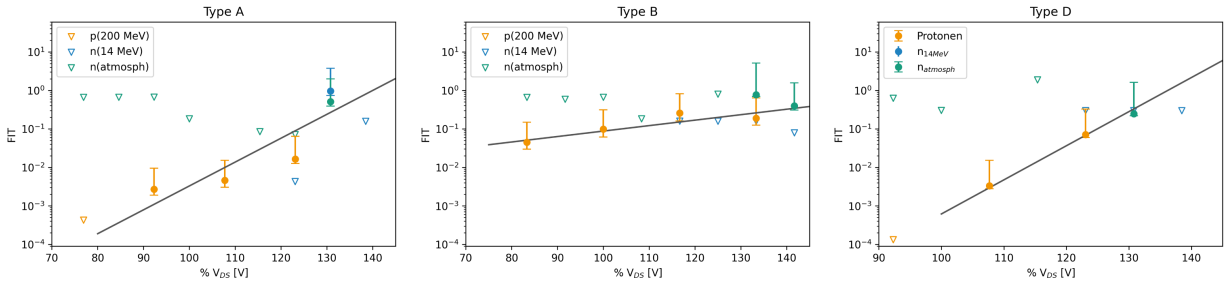

Fig. 6.3.: Logarithmic plotted FIT-rate from the neutron and proton experiments shown for each device type separately. An exponential function was plotted as an optical guideline (repetition of figure 5.11).

Not only particle type-dependent behavior of GaN HEMT devices was investigated, but also device design-specific properties were considered. Since GaN high electron mobility transistors are lateral devices and do not have a gate oxide, the influence of the gate voltage at the SEE sensitivity was not clear. Previous studies stated that the gate voltage should not have influence on the SEE rate [61]. In the first two experiments for this work at *GANIL* and *ChipIR*, the devices were operated both with unbiased and with negatively biased gate. No difference in the failure rate of the devices was found, from which it can be carefully concluded that it makes no difference whether the device gate is pretensioned or not when a particle hit.

During the measurements for this work, two failure mechanisms were observed. The current characteristics I_{DS} and I_{GS} corresponds to the error mechanisms proposed by [61] of a short circuit between drain and source, i.e. a destruction of the blocked gate, and a conduction path between drain and substrate. Noticeable was the difference between ion and neutron irradiation in devices of similar design (*Type A* and *Type B*). Upon ion irradiation, the devices both exhibited the failure mode of a conduction path to the substrate, which is plausible for a high-energy particle entering the device perpendicular to the DUT surface. When irradiated with neutrons, however, device *Type B* continued to show the short circuit between drain and substrate as the cause of failure, while *Type A* showed 90% of the measured events conductivity between drain and source as failure mode. This suggests qualitatively that the two device types differ in the gate material or the overlying field plate, with component A being more sensitive to scattering in this area. Initial studies cite this region as the most sensitive to SEE [62, 83, 106]. Whether the gate material or the shape and material of the field plate is the critical element remains to be clarified, as heavy elements such as tungsten or gold are used to shape the electric field at the gate. This leads to heavy excited recoils which can have a high energy input into the material. To investigate exactly this question, two beam times at the micro-probe of GSI (Darmstadt, Germany) were planned for March 2020. There, the device could have been scanned micrometer by micrometer and ion by ion.

For this experiment, the Ferdinand Braun Institute had provided extra DUTs with a known structure and individual drain-gate-source structures. Unfortunately, this experiment had to be canceled at the last moment due to the lockdown.
In summary, the GaN HEMT COTS devices studied in this work are one half to one order of magnitude less sensitive, meaning have lower cross sections, than comparable Si and SiC devices found in literature. The effect of the wider bandgap in comparison with the Si devices seems to be only partially compensated by the higher interaction number with the lattice atoms.
The approach of deducing sensitivity to terrestrial radiation from monoenergetic protons over $200\,MeV$ seems promising, but needs further research. The devices would have to work closer to their capabilities to achieve comparability and enough failures for sufficient statistics in an acceptable time. Devices should be specifically tested again at only one voltage close to the breakdown limit with all three irradiation options and at least 10 parts and ideally more than three failures should be detected for each type of irradiation. This should provide better comparability with the aim of obtaining a fluence realization for the different nucleons and energies, if applicable. The same irradiation setup should be repeated under different irradiation angles, including parallel to the channel. For the irradiation in this work, the setup was always chosen with the gate plate facing the beam, as this was previously assumed to be the most sensible structure. However, it would also be necessary to investigate the effect of irradiation parallel to the electron gas channel.

Bibliography

[1] R. A. Millikan and G. H. Cameron, *High Altitude Tests on the Geographical, Directional, and Spectral Distribution of Cosmic Rays*, Physical Review **31** (1928).

[2] *IBM experiments in soft fails in computer electronics: (1978-1994)*, IBM Journal of Research and Development (1996).

[3] A. C. Strickland, *Annals of the International Years of the Quiet Sun*, **7** (1970).

[4] T. C. May and M. H. Woods, *Alpha-particle-induced Soft Errors in Dynamic Memories*, IEEE Transactions on Electron Devices **26** (1979).

[5] W. A. Kolasinski and et al., *Simulation of Cosmic-Ray Induced Soft Errors and Latchup in Integrated-Circuit Computer Memories*, IEEE Transactions on Nuclear Science **26**, 5087 (1979).

[6] J. F. Ziegler, *Terrestrial Cosmic Rays*, IBM Journal of Research and Development **40** (1998).

[7] M. Jimenez, *Cosmic Ray Failures of Power Semiconductor Devices*, ABB Semiconductors Native Post (2019).

[8] L. M. Geppert and et al., *Ion Microbeam probing of Sense Amplifiers to analyze Single Event Upsets in a CMOS DRAM*, IEEE Journal of Solid-State Circuits **26** (1991).

[9] JEDEC, *JESD57A - Test Procedures for the Measurement of Single-Event Effects in Semiconductor Devices from Heavy Ion Irradiation*, 2017.

[10] JEDEC, *JEP151 - Test Procedure for the Measurement of Terrestrial Cosmic Ray Induced Destructive Effects in Power Semiconductor Devices*, 12.2015.

[11] ESCC, *Basic Specification No. 25100: Single Event Effects Test Method and Guidelines*, 2014.

[12] A. Johnston, *Reliability and radiation effects in compound semiconductors*, World Scientific, 2010, ISBN: 978-981-4277-10-5.

[13] J. F. Ziegler and H. Puchner, *SER - History, Trends and Challenges: A Guide for Designing with Memory ICs*, Cypresse, 2004.

[14] H. Kabza and et al., *Cosmic Radiation as a Cause for Power Device Failure and Possible Countermeasures*, Symposium on Power Semiconductor Devices & IC's (1994).

[15] Jean-Marie Lauenstein, *Wide Bandgap Power- SiC, GaN - Radiation Reliability*, NSREC Short Course Notebook (2020).

[16] S. Bazzoli and et al., *SEE Sensitivity of a COTS GaN Transistor and Silicon MOSFETs*, 9th European Conference on Radiation and Its Effects on Components and Systems (2007).

[17] L. Scheick, *Determination of Single-Event Effect Application Requirements for Enhancement Mode Gallium Nitride HEMTs for Use in Power Distribution Circuits*, IEEE Transactions on Nuclear Science **61** (2014).

[18] L. Scheick, *Recent Gallium Nitride Power HEMT Single-Event Testing Results*, IEEE Radiation Effects Data Workshop (2016).

[19] M. Rostewitz and et al., *Single Event Effect Analysis on DC and RF Operated AlGaN/GaN HEMTs*, IEEE Transactions on Nuclear Science **60** (2013).

[20] J.-L. Autran and D. Munteanu, *Atmospheric Neutron Radiation Response of III–V Binary Compound Semiconductors*, IEEE Transactions on Nuclear Science **67** (2020).

[21] A. Lidow and et al., *Single-Event and Radiation Effect on Enhancement Mode Gallium Nitride FETs*, IEEE Nuclear and Plasma Sciences Society (2014).

[22] G. F. Knoll, *Radiation detection and measurement*, Wiley, New York, 3. edition, 2000, ISBN: 9780471073383.

[23] W. Demtröder, *Experimentalphysik 3: Atome, Moleküle und Festkörper 4. Aufl. 2010*, Springer-Lehrbuch, Berlin, 2010, ISBN: 9783642039119.

[24] F. Thuselt, *Physik der Halbleiterbauelemente: Einführendes Lehrbuch für Ingenieure und Physiker*, Springer, Berlin, 2005, ISBN: 3540223169.

[25] R. J. Trew, *SiC and GaN Transistors - is there one Winner for Microwave Power Applications?*, Proceedings of the IEEE **90** (2002).

[26] D. Meschede, *Gerthsen Physik 23., überarbeite Auflage*, Springer, Berlin, 2006, ISBN: 9783540299738.

[27] Bergmann and Schäfer, *Sterne und Weltraum: 2te, stark erw. und aktualisierte Aufl.*, Walter de Gruyter, Berlin, 2002, ISBN: 9783110221596.

[28] J.-L. Autran, *Soft Errors: From Particles to Circuits*, Taylor & Francis Group, Baton Rouge, 2015, ISBN: 9781466590847.

[29] Daniel Gomez Toro, *Temporal Filtering with Soft Error Detection and Correction Technique for Radiation Hardening Based on a C-Element and BICS*, Dissertation, Universite de Bretagne Occidentale, Bretagne, 12.12.2014.

[30] Manfred Krammer, *Wechselwirkung von Teilchen/Strahlung mit Materie: Detektoren in der Hochenergiephysik*, Sommersemester 2005, Institut für Hochenergiephysik der ÖAW, Wien.

[31] H. H. K. Tang, *Nuclear Physics of Cosmic Ray Interaction with Semiconductor Materials: Particle-induced Soft Errors from a Physicist's Perspective*, IBM Journal of Research and Development **40** (1996).

[32] C. Bussolati and et al., *Energy for Electron-Hole Pair Generation in Silicon by Electrons and a Particles*, Physical Review (1964).

[33] Abram, *Wechselwirkungen zwischen Strahlung und Materie*, www.bcp.fu-berlin.de/chemie-/chemie/forschung/InorgChem/agabram/pdf/radiochemie/04_radiodeutsch.pdf, Strahlenschutzurs 2012, last visited 2022-04-2022, FU Berlin.

[34] S. J. Pearton and et al., *Review - Ionizing Radiation Damage Effects on GaN Devices*, ECS Journal of Solid State Science and Technology **5** (2016).

[35] V. A. J. van Lint and et al., *Energy Dependence of Displacement Effects in Semiconductors*, IEEE Transactions on Nuclear Science **19** (1972).

[36] O. L. Curtis and et al., *Effect of Irradiation on the Hole Lifetime of N –Type Germanium*, Journal of Applied Physics **28** (1957).

[37] J. R. Srour and et al., *Review of Displacement Damage Effects in Silicon Devices*, IEEE Transactions on Nuclear Science **50** (2003).

[38] T. A. Fischer, *Heavy-Ion-Induced Gate-Rupture in Power MOSFETs*, IEEE Transactions on Nuclear Science **34** (1987).

[39] S. Kuboyama and et al., *Improved Model for Single-Event Burnout Mechanism*, IEEE Transactions on Nuclear Science **51** (2004).

[40] D. R. Ball and et al., *Ion-Induced Energy Pulse Mechanism for Single-Event Burnout in High-Voltage SiC Power MOSFETs and Junction Barrier Schottky Diodes*, IEEE Transactions on Nuclear Science **67** (2020).

[41] N. Herbecq and et al., *1900 V, 1.6 mOhm cm^2 AlN/GaN-on-Si Power Devices realized by local Substrate removal*, Applied Physics Express (2014).

[42] M. Meneghini and et al., *Technology and Reliability of Normally-Off GaN HEMTs with p-Type Gate*, mdpi Energies **10** (2017).

[43] Y. P. Varshni, *Temperature Dependence of the Energy Gap in Semiconductors*, Physica (1967).

[44] I. N. Remediakis and E. Kaxiras, *Band-Structure calculations for Semiconductors within generalized-Density-functional Theory*, Physical Review B (1999).

[45] B.-J. Godejohann, *GaN-based high electron mobility transistors with high Al-content barriers*, Dissertation, Freiburg, 2017.

[46] L. Hsu and W. Walukiewicz, *Effects of Piezoelectric Field on Defect Formation, Charge Transfer, and Electron Transport at GaN/AlxGa1−xN Interfaces*, Applied Physics Letters (1998).

[47] J. P. Ibbetson and et al., *Polarization Effects, Surface States, and the Source of Electrons in AlGaN/GaN Heterostructure Field Effect Transistors*, Applied Physics Letters (2000).

[48] J.-T. Chen and et al., *Room-Temperature Mobility above 2200 cm^2 /V · s of two-dimensional electron gas in a sharp-interface AlGaN/GaN heterostructure*, Applied Physics Letters (2015).

[49] O. Ambacher and et al., *Pyroelectric Properties of Al(In)GaN/GaN Hetero- and Quantum Well Structures*, Journal of Physics: Condensed Matter (2002).

[50] C. Ma and et al., *On-State Critical Gate Overdrive Voltage for Fluorine-Implanted Enhancement-mode AlGaN/GaN High Electron Mobility Transistors*, Journal of Applied Physics **110** (2011).

[51] T.-L. Wu and et al., *The Impact of the Gate Dielectric Quality in developing Au-free D-mode and E-mode recessed Gate AlGaN/GaN Transistors on a 200mm Si substrate*, Symposium on Power Semiconductor Devices & IC's (2015).

[52] T. Hirose and et al., *Dynamic Performances of GaN-HEMT on Si in Cascode Configuration*, IEEE Applied Power Electronics Conference and Exposition (2014).

[53] Y. Uemoto and et al., *Gate Injection Transistor (GIT)—A Normally-Off AlGaN/GaN Power Transistor Using Conductivity Modulation*, IEEE Transactions on Nuclear Science **54** (2007).

[54] M. Meneghini and et al., *Electrical and Electroluminescence Characteristics of AlGaN/GaN High Electron Mobility Transistors Operated in Sustainable Breakdown Conditions*, Japanese Journal of Applied Physics **52** (2013).

[55] B. D. Weaver and et al., *Displacement Damage Effects in AlGaN/GaN High Electron Mobility Transistors*, IEEE Transactions on Nuclear Science **59** (2012).

[56] A. Ionascut-Nedelcescu and et al., *Radiation Hardness of Gallium Nitride*, IEEE Transactions on Nuclear Science **49** (2002).

[57] G. Sonia and et al., *2 MeV Ion Irradiation Effects on AlGaN/GaN HFET Devices*, Solid-State Electronics **52** (2008).

[58] S. M. Khanna and et al., *2 MeV Proton Radiation Damage Studies of Gallium Nitride Films through low Temperature Photoluminescence Spectroscopy Measurements*, IEEE Transactions on Nuclear Science **47** (2000).

[59] S. J. B. and et al., *Worst Case Heavy Ion Testing Conditions for Normally-Off GaN-Based High Electron Mobility Transistor: 23th European Conference on Radiation and Its Effects on Components and Systems (RADECS)*, 23th European Conference on Radiation and Its Effects on Components and Systems (RADECS), 2023.

[60] S. Morand, *Status on OSIP Studies on COTS Power GaN Heavy Ion Effects evaluation for Space, 2023-06-30*, https://indico.esa.int/event/444/contributions/7790/attachments/5325/8536/fpd_osip_GaN_rev4.pdf, last visited 2023-12-05.

[61] E. Mizuta and et al., *Single-Event Damage Observed in GaN-on-Si HEMTs for Power Control Applications*, IEEE Transactions on Nuclear Science **65** (2018).

[62] M. Zerarka and et al., *TCAD Simulation of the Single Event Effects in Normally-off GaN Transistors after Heavy Ion Radiation*, IEEE Transactions on Nuclear Science **64** (2017).

[63] E. Petersen, *Single Event Effects in Aerospace: 1. Aufl.*, Wiley-IEEE Press, 2011, ISBN: 0470767499.

[64] Stephen M. Seltzer, *Fundamental Quantities and Units for Ionizing Radiation*, ICRU Report **85** (2011).

[65] J. M. Osheroff and et al., *LET and Range Characteristics of Proton Recoil Ions in Gallium Nitride (GaN)*, IEEE Transactions on Nuclear Science **68** (2021).

[66] D. Munteanu and J. L. Autran, *Terrestrial neutron-induced Single Events in GaN*, Microelectronics Reliability **100-101** (2019).

[67] James Ziegler, *SRIM & TRIM: SRIM-2013*, http://srim.org/.

[68] D. Munteanu and J.-L. Autran, editors, *Susceptibility of Group-IV and III-V Semiconductor-Based Electronics to Atmospheric Neutrons Explored by Geant4 Numerical Simulations*, Numerical Simulations in Engineering and Science, 2018.

[69] E. C. Smith and M. Shoga, *Double Upsets from glancing Collisions: a simple Model verified with flight data (SRAM)*, IEEE Transactions on Nuclear Science **39** (1992).

[70] L. D. Edmonds, *SEU Cross Sections Derived from a Diffusion Analysis*, IEEE Transactions on Nuclear Science **43** (1996).

[71] E. Petersen, *Cross Section Measurements and Upset Rate Calculations*, IEEE Transactions on Nuclear Science **43** (1996).

[72] R. Velazco and et al., editors, *Radiation Effects on Embedded Systems*, Springer, Dordrecht, 2007.

[73] V. Ferlet-Cavrois and et al., *Charge Collection in Power MOSFETs for SEB Characterisation—Evidence of Energy Effects*, IEEE Transactions on Nuclear Science **57** (2010).

[74] Weapons Neutron Research Facility at LANSCE, https://lansce.lanl.gov/facilities/wnr/index.php, last visited 2022-05-24.

[75] Canada's particle accelerator centre TRIUMF, https://www.triumf.ca/, last visited 2022-03-04.

[76] C. Cazzaniga and C. D. Frost, *Progress of the Scientific Commissioning of a fast neutron beamline for Chip Irradiation*, Journal of Physics: Conference Series (2018).

[77] C. Dyer and et al., *Neutron-Induced Single Event Effects Testing Across a Wide Range of Energies and Facilities and Implications for Standards*, IEEE Transactions on Nuclear Science **53** (2006).

[78] Research Center for Nuclear Physics, Osaka University, https://www.rcnp.osaka-u.ac.jp/Divisions/np1-a/RCF/RCNPCF-WNt.html, last visited 2023-01-07.

[79] P. M. O'Neill and et al., *Risk Assessment for Heavy Ions of Parts Tested with Protons*, IEEE Transactions on Nuclear Science **44** (1997).

[80] J. Scarpulla, *Guidelines for Space Qualification of GaN HEMTs and MMICs*, IEEE International Reliability Physics Symposium , 1 (2021).

[81] Department of Defence United States of America, *Test method standard environmental test methods for semiconductor devices: MIL-STD-750-1A*, 2016.

[82] GaN Systems Inc., *GS66502B: Rev 180213*, https://gansystems.com, last visited 2022-02-28.

[83] Dr. Oliver Hilt, *Nachbesprechung zur Bestrahlung der FBH Bauteile an der ISIS Neutronenquelle*, persönliches Gespräch 26.11.2019.

[84] X. Wang and et al., *Degradation Behavior and Mechanism of GaN HEMTs With P-Type Gate in the Third Quadrant Under Repetitive Surge Current Stress*, IEEE Transactions on Electron Devices (2022).

[85] Panasonic Semiconductor Solutions Co., *PGA26E19BA Product Overview: FLY000075_EN*, https://industry.panasonic.eu/, last visited 2022-02-28.

[86] Ronald Barr, *Qualification Report TPH320XPS and TPH320XPD Rev 5*, (2015).

[87] Transphorm Inc., *Datasheet TPH3202P*, https://www.transphormusa.com, last visited 2022-02-28.

[88] ROHM Co., *SCT3120AL: SiC Power Devices Rev. C 2017*, https://www.rohm.com, last visited 2022-02-28.

[89] Website of the Ferdinand-Braun-Institut, https://www.fbh-berlin.de, last visited 2022-03-04.

[90] Oliver Hilt, *10 GaN-Schalttransistoren für Bestrahlungsexperimente vom Fraunhofer INT*, 2018-09-17.

[91] Grand Accélérateur National d'Ions Lourds, https://www.ganil-spiral2.eu, last visited 2022-03-04.

[92] P. Fernandez-Martinez and et al., *SEE Tests With Ultra Energetic Xe Ion Beam in the CHARM Facility at CERN*, IEEE Transactions on Nuclear Science (2019).

[93] CHARM - Mixed fields at CERN, https://kt.cern/technologies/charm-mixed-fields, last visited 2022-03-04.

[94] R. Garcia-Alia and et al., *Ultraenergetic Heavy-Ion Beams in the CERN Accelerator Complex for Radiation Effects Testing*, IEEE Transactions on Nuclear Science (2019).

[95] OncoRay National Center for Radiation Research, https://www.oncoray.de, last visited 2022-03-04.

[96] C. D. Frost and et al., *A new dedicated neutron facility for accelerated SEE testing at the ISIS facility*, IEEE International Reliability Physics Symposium (2009).

[97] *ChipIr at ISIS Neutron and Muon Source*, https://www.isis.stfc.ac.uk/Pages/ChipIR.aspx, last visited 2022-03-04.

[98] *Website of Fraunhofer INT*, https://www.int.fraunhofer.de, last visited 2022-03-04.

[99] C. Weulersse and et al., *Preliminary Guidelines and Predictions for 14 MeV Neutron SEE Testing*, IEEE Transactions on Nuclear Science , 1 (2017).

[100] Andrea Coronetti, *D4.1 – Evaluation report of 14-MeV neutron test methodology: 721624 RADSAGA ITN Deliverable report*, 2019-06-30.

[101] *Irradiation @ IFA-TSL (The Svedberg laboratory)*, https://www.tsl.uu.se/about-tsl/irradiation/, last visited 23.05.2022.

[102] C. Martinella and et al., *Impact of Terrestrial Neutrons on the Reliability of SiC VD-MOSFET Technologies*, IEEE Transactions on Nuclear Science **68** (2021).

[103] A. Hands and et al., *Single Event Effects in Power MOSFETs and SRAMs Due to 3 MeV, 14 MeV and Fission Neutrons*, IEEE Transactions on Nuclear Science **58** (2011).

[104] C. Felgemacher and et al., *Cosmic Radiation Ruggedness of Si and SiC Power Semiconductors*, International Symposium on Power Semiconductor Devices and ICs **28** (2016).

[105] F. Principato and et al., *Accelerated Tests on Si and SiC Power Transistors with Thermal, Fast and Ultra-Fast Neutrons*, mdpi Sensors **20** (2020).

[106] M. Zerarka and O. Crepel, *Radiation robustness of normally-off GaN/HEMT power transistors (COTS)*, Microelectronics Reliability **88-90** (2018).

[107] Microsoft Corporation, *Microsoft Excel*, https://office.microsoft.com/excel, 2018.

A. Additional Figures

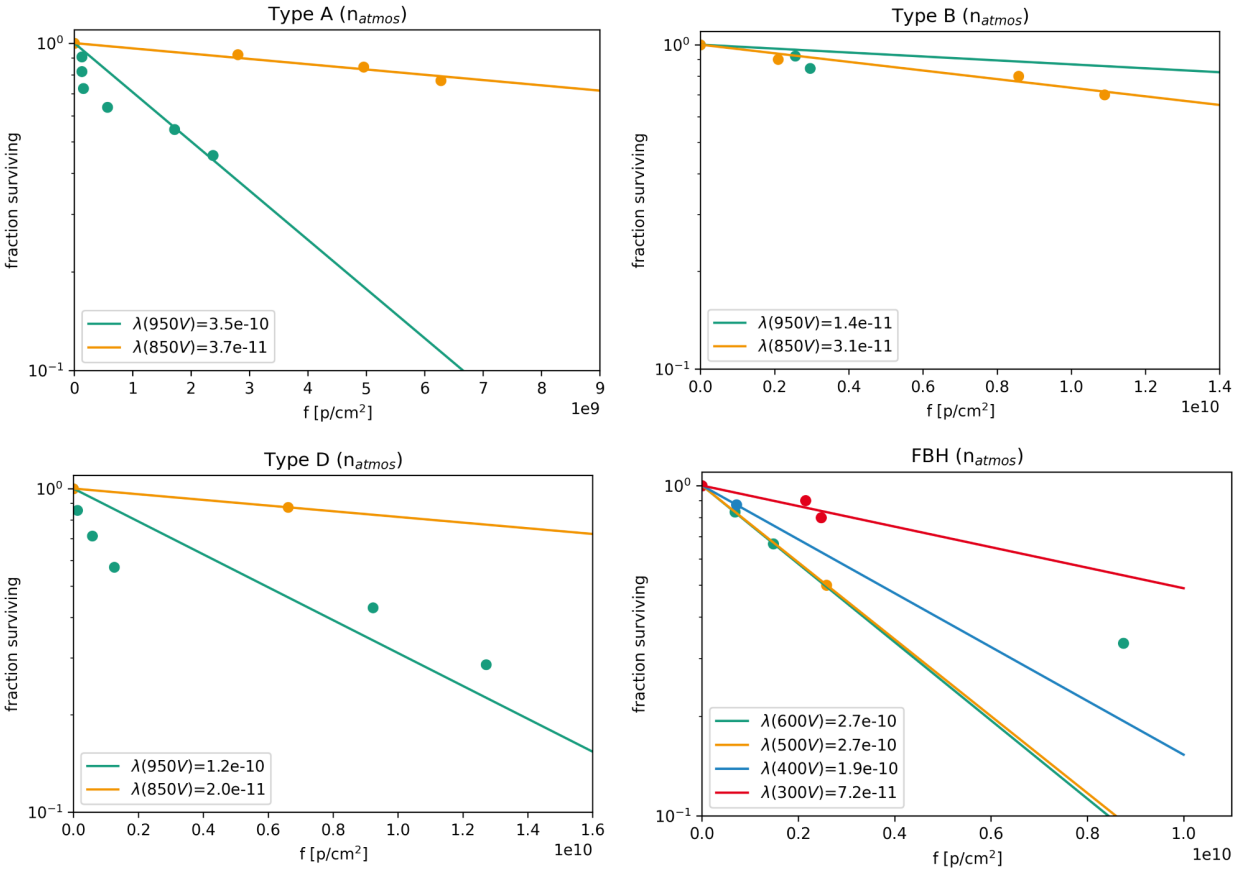

Fig. A.1.: Fraction of the surviving DUTs during the neutron irradiation at ChipIR. In the measurements with the highest drain voltages, a bend in the curve can be seen at higher fluence for each component type. This should mean that at the same drain voltage, the sensitivity decreases with the fluence.
One could assume that the first failures are triggered by the physical stress nearby the breakdown voltage and not by the radiation and thus overestimate the sensitivity. However, there is no method to distinguish this with certainty. Therefore, this voltage was excluded from further investigations.

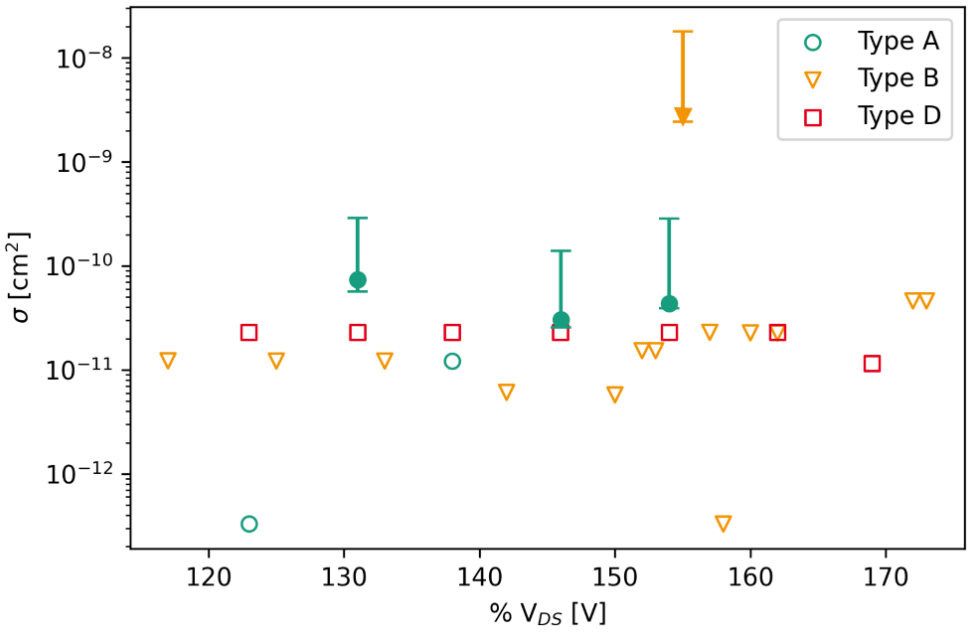

Fig. A.2.: The result of the measurements with $14\,MeV$ neutrons at FhG INT is plotted. The filled marker gives measured values of the cross section σ in cm^2 and the colorless marker indicate upper limits of the σ. The single *Type B* device failure, which is omitted from graph 5.4, is shown here at $155\,\%V$.

B. Fit Values and Calculations Examples

Calculation Examples

Survival Rate

Exemplary calculation for the survival rate using the *Type A* device exposed to proton irradiation at $600\,V$ drain voltage V_{DS}. Data from the log file C.9:

Date	Run	beam on	Type	Dev Nr.	V_{DS} [V]	Status	f [p/cm^2]
24.09.2020	25	12:32	Type A	72	600	fail	$2.75 \cdot 10^{12}$
	33	14:31	Type A	76	600	pass	$1.01 \cdot 10^{13}$
	42	16:16	Type A	79	600	fail	$1.10 \cdot 10^{12}$
25.09.2020	69	14:52	Type A	83	600	fail	$4.62 \cdot 10^{12}$
	70	15:18	Type A	85	600	fail	$1.65 \cdot 10^{12}$
	71	15:25	Type A	84	600	pass	$9.82 \cdot 10^{12}$

From this it follows that six DUTs were measured, four of which failed and two of which did not fail. Sort the breakdowns by fluence

Tab. B.1.: Values for the exemplary calculation sorted according to fluence

Type	Dev Nr.	V_{DS} [V]	Status	f [p/cm^2]
Type A	79	600	fail	$1.10 \cdot 10^{12}$
Type A	85	600	fail	$1.65 \cdot 10^{12}$
Type A	72	600	fail	$2.75 \cdot 10^{12}$
Type A	83	600	fail	$4.62 \cdot 10^{12}$

Add the total number of remaining devices n_i after the fail-fluence is reached and normalized to one

Type	n_i	fraction	Status	f [p/cm^2]
Type A	5	$5/6 = 0.83$	fail	$1.10 \cdot 10^{12}$
Type A	4	$4/6 = 0.66$	fail	$1.65 \cdot 10^{12}$
Type A	3	$3/6 = 0.5$	fail	$2.75 \cdot 10^{12}$
Type A	2	$2/6 = 0.33$	fail	$4.62 \cdot 10^{12}$

plot *fraction* against the *fluence* (dots) and fit the function 5.1 to the measured values using the optimize package of scipy-python (line).

$$f(\mathrm{f}) = e^{-\lambda \mathrm{f}}$$

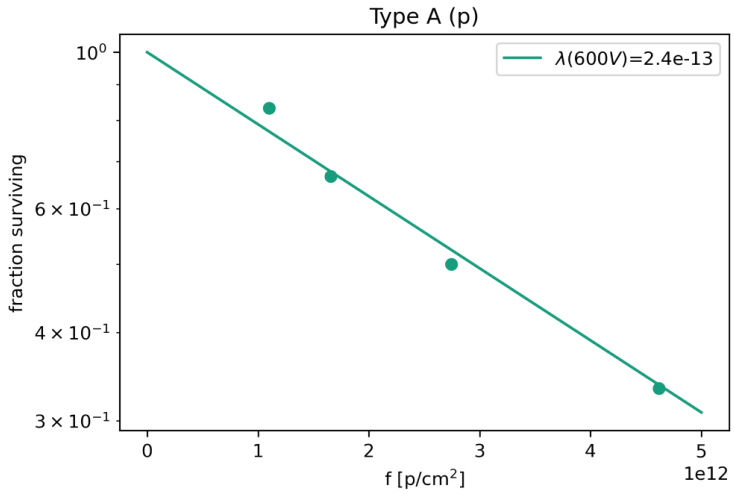

Fig. B.1.: Example Survival Rate, *Type A*, protons, 600 *V*

Cross Section

To calculate the cross section, all devices of one type measured at the same drain voltage are taken for each type of irradiation. In the example *Type A* components at $600\,V$ under proton irradiation.

Take the measured values from the failed devices (see above table B.1)

Type	**Dev Nr.**	$\mathbf{V}_{DS}$ **[V]**	**Status**	**f [p/cm^2]**
Type A	79	600	fail	$1.10 \cdot 10^{12}$
Type A	85	600	fail	$1.65 \cdot 10^{12}$
Type A	72	600	fail	$2.75 \cdot 10^{12}$
Type A	83	600	fail	$4.62 \cdot 10^{12}$

Calculate the difference to the next smaller fluence $\Delta\phi_i$:

Type	**Dev Nr.**	$\mathbf{V}_{DS}$ **[V]**	**Status**	**f [p/cm^2]**	$\mathbf{n_i}$	$\Delta\phi_i/cm^2$
Type A	79	600	fail	$1.10 \cdot 10^{12}$	6	$1.10 \cdot 10^{12}$
Type A	85	600	fail	$1.65 \cdot 10^{12}$	5	$5.53 \cdot 10^{11}$
Type A	72	600	fail	$2.75 \cdot 10^{12}$	4	$1.09 \cdot 10^{12}$
Type A	83	600	fail	$4.62 \cdot 10^{12}$	3	$3.49 \cdot 10^{11}$

With function 5.2, N = total number of fails and n_i number of remaining parts, follows

$$\sigma = \frac{N}{\Phi} = \frac{N}{\Sigma_i n_i \Delta\phi_i} = \frac{4}{1.94 \cdot 10^{13}}\,cm^2 = 2.07 \cdot 10^{-13}\,cm^2$$

The uncertainty intervals are calculated as in equation 5.3 [11, 10] with $\alpha = 5\%$ and the χ^2-function calculated for $N = 4$ with [107]

$$\Delta\sigma_{upper} = \sqrt{\left(\frac{\chi^2_{\alpha/2}(2(N+1))}{2\Phi}\right)^2 + \left(\frac{N\cdot\Delta\Phi}{\Phi^2}\right)^2}\, cm^2$$

$$= \sqrt{\left(\frac{1}{2}\frac{20.48}{1.94\cdot 10^{13}}\right)^2 + \left(\frac{4\cdot 1.94\cdot 10^{12}}{(1.94\cdot 10^{13})^2}\right)^2}\, cm^2$$

$$\Delta\sigma_{upper} = 5.28\cdot 10^{-13}\, cm^2$$

$$\Delta\sigma_{lower} = \sqrt{\left(\frac{\chi^2_{\alpha/2}(2N)}{2\Phi}\right)^2 + \left(\frac{N\cdot\Delta\Phi}{\Phi^2}\right)^2}\, cm^2$$

$$= \sqrt{\left(\frac{1}{2}\frac{2.18}{1.94\cdot 10^{13}}\right)^2 + \left(\frac{4\cdot 1.94\cdot 10^{12}}{(1.94\cdot 10^{13})^2}\right)^2}\, cm^2$$

$$\Delta\sigma_{lower} = 5.98\cdot 10^{-14}\, cm^2$$

Weibull Fit Values

Tab. B.2.: All parameters obtained for the four parameter Weibull-function on the measured cross section, and for comparison the die size as maximum sensitive area

Type	σ_{sat}	LET_{th}	W	S	die surface
Type A	$(4.71 \pm 6.6)\cdot 10^{-3}$	6.17 ± 6	352 ± 142	3.4 ± 5	$0.03 \pm 0.005\ cm^2$
Type B	$(9.06 \pm 1.4)\cdot 10^{-3}$	6.50 ± 9	101 ± 429	3.8 ± 5	$0.04 \pm 0.004\ cm^2$

Survival Rate Fit Values

Tab. B.3.: Fit values for the exponential function of the survival rate $f(\mathrm{f}) = e^{-\lambda \mathrm{f}}$, and calculated cross section values

Facility	**Type**	$\mathbf{V_{DS}}$ [V]	λ	$\sigma\,[cm^2]$
GANIL	A	650	$(1.6 \pm 0.3) 10^{-5}$	$(1.1 \pm 6.3) 10^{-5}$
GANIL	A	600	$(4.0 \pm 2.6) 10^{-6}$	$(2.5 \pm 9.1) 10^{-6}$
GANIL	A	550	$(2.5 \pm 2.3) 10^{-6}$	$(2.1 \pm 0.1) 10^{-6}$
GANIL	A	500	$(5.3 \pm 1.2) 10^{-7}$	$(4.6 \pm 16.6) 10^{-7}$
INT	A	950	$(3.3 \pm 0.7) 10^{-11}$	$(3.0 \pm 11.0) 10^{-11}$
INT	A	850	$(6.9 \pm 1.2) 10^{-11}$	$(7.4 \pm 21.6) 10^{-11}$
INT	B	930	$(3.3 \pm 3.4) 10^{-9}$	$(2.7 \pm 15.2) 10^{-9}$
ISIS	A	850	$(3.7 \pm 0.4) 10^{-11}$	$(3.9 \pm 11.4) 10^{-11}$
ISIS	B	850	$(3.1 \pm 0.4) 10^{-11}$	$(3.1 \pm 9.0) 10^{-11}$
ISIS	D	850	$(2.0 \pm 1.9) 10^{-11}$	$(1.9 \pm 10.5) 10^{-11}$
ISIS	FBH	500	$(1.9 \pm 1.9) 10^{-10}$	$(1.9 \pm 10.8) 10^{-10}$
ISIS	FBH	400	$(2.7 \pm 0.3) 10^{-10}$	$(1.8 \pm 9.8) 10^{-10}$
ISIS	FBH	300	$(2.7 \pm 0.5) 10^{-10}$	$(8.2 \pm 29.7) 10^{-11}$
OncoRay	A	800	$(1.4 \pm 0.3) 10^{-12}$	$(1.3 \pm 3.7) 10^{-12}$
OncoRay	A	700	$(3.5 \pm 0.6) 10^{-13}$	$(3.5 \pm 8.3) 10^{-13}$
OncoRay	A	600	$(2.4 \pm 0.2) 10^{-13}$	$(2.1 \pm 5.3) 10^{-13}$
OncoRay	B	800	$(7.8 \pm 2.1) 10^{-11}$	$(1.5 \pm 3.4) 10^{-11}$
OncoRay	B	700	$(2.0 \pm 0.4) 10^{-11}$	$(2.0 \pm 4.4) 10^{-11}$
OncoRay	B	600	$(1.1 \pm 0.2) 10^{-11}$	$(7.6 \pm 16.5) 10^{-12}$
OncoRay	B	500	$(6.0 \pm 0.6) 10^{-12}$	$(3.5 \pm 8.1) 10^{-12}$
OncoRay	C	800	$(2.2 \pm 0.3) 10^{-12}$	$(1.8 \pm 4.6) 10^{-12}$
OncoRay	C	700	$(1.4 \pm 0.2) 10^{-12}$	$(1.4 \pm 3.0) 10^{-12}$
OncoRay	C	600	$(8.9 \pm 0.1) 10^{-13}$	$(8.8 \pm 19.1) 10^{-13}$
OncoRay	C	500	$(4.9 \pm 1.0) 10^{-13}$	$(4.8 \pm 11.2) 10^{-13}$
OncoRay	D	800	$(7.2 \pm 0.3) 10^{-12}$	$(5.5 \pm 19.7) 10^{-12}$
OncoRay	D	700	$(3.0 \pm 0.6) 10^{-13}$	$(2.6 \pm 9.2) 10^{-13}$

C. Log-Files

In the following, the measurement data is given.
Thereby the **'Run'** indicates the run number of the experiment and is used to identify the associated voltage and current logs. **'beam on'** gives the start time of the run, **'Type'** the device type and **'DUT Nr.'** the unique identification number of the device so that each DUT can be assigned to a measurement. 'V_{DS}' and 'V_{GS}' give the voltages at the drain, and if given at the gate. **'f'** is the fluence at which the device failed in units of ions or nucleons per square centimeter. The last column **'Status'** shows whether the device has failed at this fluence or survived it.
Any other special features are named in the table heading.

Measurement at GANIL

Tab. C.1.: Logfile of the measurement at GANIL 2018-06-07.
Run gives the GANIL Experiment-Run, Deg. gives the degrader in front of the beamwindow

Run	**beam on**	**Deg.**	**Type**	**DUT Nr.**	**V$_{DS}$**	**V$_{GS}$**	**f [Ion/cm^2]**	**Status**
515	18:24	0	Type A	001	600	0	2.76E+05	fail
516	18:27	0	Type A	002	100	0	3.00E+05	pass
517	18:30	0	Type A	002	200	0	3.00E+05	pass
518	18:33	0	Type A	002	300	0	3.00E+05	pass
519	18:37	0	Type A	002	400	0	3.00E+05	pass
520	18:40	0	Type A	002	500	0	3.00E+05	pass
521	18:43	0	Type A	002	550	0	3.00E+05	pass
522	18:47	0	Type A	002	600	0	6.00E+05	pass
523	18:57	0	Type A	002	650	0	3.00E+05	pass
524	19:02	0	Type A	003	500	0	9.65E+05	fail
525	19:40	0	Type A	004	500	-10	1.00E+06	pass
526	19:46	0	Type A	004	550	-10	1.00E+06	pass

Tab. C.1.: Continuation logfile GANIL

Run	beam on	Deg.	Type	DUT Nr.	V_{DS}	V_{GS}	f [Ion/cm^2]	Status
527	19:51	0	Type A	004	600	-10	2.42E+05	fail
529	19:56	0	Type A	005	550	-10	1.60E+05	fail
530	20:15	0	Type A	006	500	-10	1.00E+06	pass
531	20:23	0	Type A	006	450	0	1.00E+06	pass
532	21:02	400	Type A	006	300	0	1.00E+06	pass
532	21:08	400	Type A	006	650	0	4.44E+04	fail
533	21:01	400	Type A	007	350	0	1.00E+06	pass
534	21:15	400	Type A	007	400	0	1.00E+06	pass
535	21:21	400	Type A	007	450	0	1.00E+06	pass
536	21:26	400	Type A	007	500	0	5.00E+05	fail
537	21:47	0	Type B	001	600	0	2.60E+04	fail
538	21:49	0	Type B	002	400	0	9.40E+04	fail

Measurements at ChipIR (ISIS)

Tab. C.2.: Logfile of the measurement at ChipIR (ISIS -Rutherford Laboratory) 2018-09-24

Run	beam on	Type	Dev Nr.	V_{DS} [V]	V_{GS} [V]	Status	f [n/cm^2]
1	13:14:00	Type A	001	400	0	pass	3.274E+09
	13:14:00	Type A	002	400	0	pass	3.274E+09
2	13:31:00	Type A	001	500	0	pass	3.286E+09
	13:31:00	Type A	002	500	0	pass	3.286E+09
3	13:20:00	Type A	001	550	0	pass	3.273E+09
	13:20:00	Type A	002	550	0	pass	3.273E+09
4	14:07:00	Type A	001	600	0	pass	3.237E+09
	14:07:00	Type A	002	600	0	pass	3.237E+09
5	14:24:03	Type A	001	650	0	pass	3.239E+09
	14:24:03	Type A	002	650	0	pass	3.239E+09
6	14:51:07	Type B	002	400	0	pass	3.242E+09
	14:51:07	Type B	003	400	0	pass	3.242E+09

Tab. C.2.: Continuation logfile ChipIR 2018-09-24

Run	beam on	Type	Dev Nr.	V_{DS} [V]	V_{GS} [V]	Status	f [n/cm^2]
7	15:09:00	Type B	002	500	0	pass	3.295E+09
	15:09:00	Type B	003	500	0	pass	3.295E+09
8	15:25:00	Type B	002	550	0	pass	3.266E+09
	15:25:00	Type B	003	550	0	pass	3.266E+09
9	16:22:16	Type B	002	600	0	pass	3.276E+09
	16:22:16	Type B	003	600	0	pass	3.276E+09
10	16:39:03	Type B	002	650	0	pass	3.271E+10
	16:39:03	Type B	003	650	0	pass	3.271E+10
11	16:59:00	Type A	004	500	0	pass	3.258E+09
	16:59:00	Type A	005	500	0	pass	3.258E+09
12	17:15:00	Type A	004	550	0	pass	3.237E+09
	17:15:00	Type A	005	550	0	pass	3.237E+09
13	17:30:00	Type A	004	600	0	pass	3.246E+09
	17:30:00	Type A	005	600	0	pass	3.246E+09
14	17:45:00	Type A	004	650	0	pass	3.422E+09
	17:45:00	Type A	005	650	0	pass	3.422E+09
15	18:03:00	Type A	007	500	0	pass	3.248E+09
	18:03:00	Type A	010	500	0	pass	3.248E+09
16	18:19:00	Type A	007	550	0	pass	3.243E+09
	18:19:00	Type A	010	550	0	pass	3.243E+09
17	18:34:00	Type A	007	600	0	pass	3.248E+09
	18:34:00	Type A	010	600	0	pass	3.248E+09
18	18:50:00	Type A	007	650	0	pass	3.252E+09
	18:50:00	Type A	010	650	0	pass	3.252E+09
19	19:07:00	Type B	005	500	0	pass	3.248E+09
	19:07:00	Type B	006	500	0	pass	3.248E+09
20	19:23:00	Type B	005	550	0	pass	3.248E+09
	19:23:00	Type B	006	550	0	pass	3.248E+09
21	19:40:00	Type B	005	600	0	pass	3.241E+09
	19:40:00	Type B	006	600	0	pass	3.241E+09
22	19:58:00	Type B	005	650	0	pass	3.237E+09
	19:58:00	Type B	006	650	0	pass	3.237E+09
23	20:15:00	Type B	010	500	0	pass	3.250E+09
	20:15:00	Type B	009	500	0	pass	3.250E+09

Tab. C.2.: Continuation logfile ChipIR 2018-09-24

Run	beam on	Type	Dev Nr.	V_{DS} [V]	V_{GS} [V]	Status	f [n/cm^2]
24	20:31:00	Type B	010	550	0	pass	3.688E+09
	20:31:00	Type B	009	550	0	pass	3.688E+09
25	20:59:00	Type B	010	600	0	pass	3.240E+09
	20:59:00	Type B	009	600	0	pass	3.240E+09
26	21:05:00	Type B	010	650	0	pass	3.249E+09
	21:05:00	Type B	009	650	0	pass	3.249E+09
27	21:25:00	Type B	002	750	0	pass	3.243E+09
	21:25:00	Type B	003	750	0	pass	3.243E+09
28	21:43:00	Type B	002	850	0	pass	3.476E+09
	21:43:00	Type B	003	850	0	pass	3.476E+09
29	22:03:00	Type B	002	950	0	pass	3.271E+09
	22:03:00	Type B	003	950	0	pass	3.271E+09
30	22:19:00	Type A	001	750	0	pass	3.400E+09
	22:19:00	Type A	002	750	0	pass	3.400E+09
31	22:36:00	Type A	001	850	0	pass	3.340E+09
	22:36:00	Type A	002	850	0	pass	3.340E+09
32	22:52:00	Type A	001	950	0	pass	2.373E+09
	22:52:00	Type A	002	950	0	fail	2.373E+09
33	23:05:00	Type A	001	950	0	pass	3.598E+09

Tab. C.3.: Logfile of the measurement at ChipIR (ISIS -Rutherford Laboratory) 2018-09-25

Run	beam on	Type	Dev Nr.	V_{DS} [V]	V_{GS} [V]	Status	f [n/cm^2]
34	01:03:00	Type D	001	400	0	pass	3,302E+09
	01:03:00	Type D	002	400	0	pass	3,302E+09
35	01:20:00	Type D	001	500	0	pass	3,242E+09
	01:20:00	Type D	002	500	0	pass	3,242E+09
36	01:36:48	Type D	001	550	0	pass	3,185E+09
	01:36:48	Type D	002	550	0	pass	3,185E+09
37	01:51:43	Type D	001	600	0	pass	3,255E+09
	01:51:43	Type D	002	600	0	pass	3,255E+09
38	02:07:26	Type D	001	650	0	pass	3,219E+09
	02:07:26	Type D	002	650	0	pass	3,219E+09

Tab. C.3.: Continuation logfile ChipIR 2018-09-25

Run	beam on	Type	Dev Nr.	V_{DS} [V]	V_{GS} [V]	Status	f [n/cm^2]
39	02:24:02	Type C	001	400	0	pass	3,219E+09
	02:24:02	Type C	002	400	0	pass	3,219E+09
40	02:39:46	Type C	001	500	0	pass	3,251E+09
	02:39:46	Type C	002	500	0	pass	3,251E+09
41	02:55:13	Type C	001	550	0	pass	3,248E+09
	02:55:13	Type C	002	550	0	pass	3,248E+09
42	03:10:41	Type C	001	600	0	pass	3,271E+09
	03:10:41	Type C	002	600	0	pass	3,271E+09
43	03:25:50	Type D	003	500	0	pass	3,248E+09
	03:25:50	Type D	004	500	0	pass	3,248E+09
44	03:42:06	Type D	003	550	0	pass	3,292E+09
	03:42:06	Type D	004	550	0	pass	3,292E+09
45	03:57:49	Type D	003	600	0	pass	3,470E+09
	03:57:49	Type D	004	600	0	pass	3,470E+09
46	04:14:20	Type D	003	650	0	pass	3,276E+09
	04:14:20	Type D	004	650	0	pass	3,276E+09
47	04:30:36	Type C	003	500	0	pass	3,256E+09
	04:30:36	Type C	004	500	0	pass	3,256E+09
48	04:46:01	Type C	003	550	0	pass	2,707E+09
	04:46:01	Type C	004	550	0	pass	2,707E+09
49	05:01:56	Type C	003	600	0	pass	3,242E+09
	05:01:56	Type C	004	600	0	pass	3,242E+09
50	05:17:15	Type C	003	650	0	pass	3,306E+09
	05:17:15	Type C	004	650	0	pass	3,306E+09
51	05:33:34	Type D	005	550	0	pass	3,288E+09
	05:33:34	Type D	006	550	0	pass	3,288E+09
52	05:49:23	Type D	005	600	0	pass	3,286E+09
	05:49:23	Type D	006	600	0	pass	3,286E+09
53	06:05:30	Type D	005	650	0	pass	3,273E+09
	06:05:30	Type D	006	650	0	pass	3,273E+09
54	06:22:04	Type C	005	550	0	pass	3,292E+09
	06:22:04	Type C	006	550	0	pass	3,292E+09
55	06:37:48	Type C	005	600	0	pass	3,319E+09
	06:37:48	Type C	006	600	0	pass	3,319E+09

Tab. C.3.: Continuation logfile ChipIR 2018-09-25

Run	beam on	Type	Dev Nr.	V_{DS} [V]	V_{GS} [V]	Status	f [n/cm^2]
56	06:54:02	Type C	005	650	0	pass	3,319E+09
	06:54:02	Type C	006	650	0	pass	3,319E+09
57	07:11:43	Type D	001	650	-4	pass	3,315E+09
	07:11:43	Type D	002	650	-4	pass	3,315E+09
58	07:28:46	Type D	001	750	-4	pass	3,465E+09
	07:28:46	Type D	002	750	-4	pass	3,465E+09
59	07:46:18	Type C	001	650	-18	pass	3,303E+09
	07:46:18	Type C	002	650	-18	pass	3,303E+09
60	08:02:22	Type C	001	750	-18	pass	3,299E+09
	08:02:22	Type C	002	750	-18	pass	3,299E+09
61	09:59:00	Type A	011	750	-10	pass	3,249E+09
	09:59:00	Type A	012	750	-10	pass	3,249E+09
	09:59:00	Type A	013	750	-10	pass	3,249E+09
62	10:15:17	Type B	010	750	-10	pass	3,259E+09
	10:15:17	Type B	011	750	-10	pass	3,259E+09
	10:15:17	Type B	012	750	-10	pass	3,259E+09
63	10:39:33	Type B	010	950	-10	pass	1,397E+10
	10:39:33	Type B	011	950	-10	pass	1,397E+10
	10:39:33	Type B	012	950	-10	pass	1,397E+10
64	11:46:11	Type B	013	950	0	fail	2,554E+09
	11:46:11	Type B	014	950	0	fail	2,130E+10
	11:46:11	Type B	015	950	0	pass	2,775E+10
65	15:30:00	Type A	021	950	0	fail	1,255E+08
	15:30:00	Type A	025	850	0	pass	2,604E+10
	15:30:00	Type A	026	850	0	pass	2,604E+10
66	18:10:40	Type A	027	650	0	pass	5,934E+09
	18:10:40	Type B	019	650	0	pass	5,934E+09
	18:10:40	Type D	007	650	0	fail	0,000E+00
67	18:39:09	Type A	027	800	0	pass	3,001E+10
	18:39:09	Type B	019	800	0	fail	1,670E+10
68	20:57:05	Type A	027	950	0	fail	9,236E+09
	21:42:32	Type A	029	650	0	pass	2,407E+09
69	21:42:32	Type B	021	650	0	pass	2,407E+09
	21:42:32	Type D	009	650	0	pass	2,407E+09

Tab. C.3.: Continuation logfile ChipIR 2018-09-25

Run	beam on	Type	Dev Nr.	V_{DS} [V]	V_{GS} [V]	Status	f [n/cm^2]
70	21:54:48	Type A	029	850	0	fail	2,795E+09
	21:54:48	Type B	021	850	0	pass	1,054E+10
	21:54:48	Type D	009	850	0	pass	1,054E+10
71	22:43:53	Type B	021	950	0	fail	2,955E+09
	22:43:53	Type D	009	950	0	fail	9,231E+09
72	23:28:08	Type C	007	650	0	pass	2,202E+09
	23:28:08	Type C	008	650	0	pass	2,202E+09
	23:28:08	Type C	009	650	0	pass	2,202E+09
73	23:39:08	Type C	007	800	0	pass	2,257E+09
	23:39:08	Type C	008	800	0	pass	2,257E+09
	23:39:08	Type C	009	800	0	pass	2,257E+09
74	23:50:24	Type C	007	950	0	pass	4,108E+10
	23:50:24	Type C	008	950	0	pass	4,108E+10
	23:50:24	Type C	009	950	0	pass	4,108E+10

Tab. C.4.: Logfile of the measurement at ChipIR (ISIS -Rutherford Laboratory) 2018-09-26

Run	beam on	Type	Dev Nr.	V_{DS} [V]	V_{GS} [V]	Status	f [n/cm^2]
75	04:00:25	Type A	030	650	0	pass	2,225E+09
	04:00:25	Type B	022	650	0	pass	2,225E+09
	04:00:25	Type D	017	650	0	pass	2,225E+09
76	04:12:16	Type A	030	850	0	pass	2,229E+09
	04:12:16	Type B	022	850	0	pass	2,229E+09
	04:12:16	Type D	017	850	0	pass	2,229E+09
77	04:24:35	Type A	030	950	0	fail	1,255E+08
	04:24:35	Type B	022	950	0	pass	7,438E+09
	04:24:35	Type D	017	950	0	fail	1,255E+08
78	05:01:19	Type A	031	650	0	pass	2,231E+09
	05:01:19	Type B	023	650	0	pass	2,231E+09
	05:01:19	Type D	018	650	0	pass	2,231E+09
79	05:12:44	Type A	031	850	0	pass	1,605E+10
	05:12:44	Type B	023	850	0	fail	8,578E+09
	05:12:44	Type D	018	850	0	pass	1,605E+10

Tab. C.4.: Continuation logfile ChipIR 2018-09-26

Run	beam on	Type	Dev Nr.	V_{DS} [V]	V_{GS} [V]	Status	f [n/cm^2]
	06:29:10	Type D	018	950	0	pass	6,742E+09
81	07:03:58	Type A	032	650	0	pass	2,233E+09
	07:03:58	Type B	024	650	0	pass	2,233E+09
	07:03:58	Type D	019	650	0	pass	2,233E+09
82	07:16:01	Type A	032	850	0	fail	6,277E+09
	07:16:01	Type B	024	850	0	fail	1,090E+10
	07:16:01	Type D	019	850	0	fail	6,611E+09

Tab. C.5.: Logfile of the measurement at ChipIR (ISIS -Rutherford Laboratory) 2018-09-27

Run	beam on	Type	Dev Nr.	V_{DS} [V]	V_{GS} [V]	Status	f [n/cm^2]
83	09:10:49	FBH	287	200	-2	pass	3,376E+09
	09:10:49	FBH	288	200	-2	pass	3,376E+09
	09:10:49	FBH	289	200	-2	pass	3,376E+09
84	09:27:41	FBH	287	250	-2	pass	3,282E+09
	09:27:41	FBH	288	250	-2	pass	3,282E+09
	09:27:41	FBH	289	250	-2	pass	3,282E+09
85	09:43:21	FBH	287	300	-2	pass	3,353E+09
	09:43:21	FBH	288	300	-2	pass	3,353E+09
	09:43:21	FBH	289	300	-2	fail	2,149E+09
86	10:00:40	FBH	287	350	-2	pass	3,406E+09
	10:00:40	FBH	288	350	-2	pass	3,406E+09
87	10:16:47	FBH	287	400	-2	pass	3,312E+09
	10:16:47	FBH	288	400	-2	pass	3,312E+09
88	10:32:36	FBH	287	450	-2	pass	3,401E+09
	10:32:36	FBH	288	450	-2	pass	3,401E+09
89	10:48:55	FBH	287	500	-2	fail	2,586E+09
	10:48:55	FBH	288	500	-2	pass	3,288E+09
90	11:18:21	FBH	287	500	-2	leakage	3,431E+09
	11:18:21	FBH	288	500	-2	pass	3,431E+09
91	11:36:07	FBH	287	550	-2	leakage	3,301E+09
	11:36:07	FBH	288	550	-2	pass	3,301E+09

Tab. C.5.: Continuation logfile ChipIR 2018-09-27

Run	beam on	Type	Dev Nr.	V_{DS} [V]	V_{GS} [V]	Status	f [n/cm^2]
92	11:52:05	FBH	287	600	-2	leakage	8,751E+09
	11:52:05	FBH	288	600	-2	fail	8,751E+09
93	12:35:19	FBH	290	200	-2	pass	3,319E+09
	12:35:19	FBH	291	200	-2	leakage	1,381E+08
94	12:51:24	FBH	290	250	-2	leakage	3,376E+09
	12:51:24	FBH	291	250	-2	leakage	6,620E+08
95	13:08:16	FBH	290	300	-2	leakage	3,419E+09
	13:08:16	FBH	291	300	-2	leakage	1,134E+09
96	13:23:50	FBH	290	400	-2	leakage	3,013E+08
	13:23:50	FBH	291	400	-2	leakage	5,084E+09
97	14:00:00	FBH	290	600	-2	fail	1,475E+09
	14:00:00	FBH	291	600	-2	fail	6,821E+08
	14:29:11	Type B	025	650	0	pass	3,283E+09
	14:29:11	Type D	014	650	0	pass	3,283E+09
99	14:45:06	Type A	033	850	0	pass	1,309E+10
	14:45:06	Type B	025	850	0	fail	2,092E+09
	14:45:06	Type D	014	850	0	pass	1,309E+10
100	15:50:49	Type A	033	950	0	fail	1,780E+10
	15:50:49	Type D	014	950	0	fail	1,271E+10
101	17:15:24	Type A	034	850	0	pass	3,282E+09
	17:15:24	Type B	026	850	0	pass	3,282E+09
	17:15:24	Type D	015	850	0	pass	3,282E+09
102	17:31:16	Type A	034	950	0	fail	1,716E+09
	17:31:16	Type B	026	950	0	pass	2,596E+10
	17:31:16	Type D	015	950	0	pass	2,596E+10
103	19:33:00	Type B	026	1000	0	pass	7,747E+09
	19:33:00	Type D	015	1000	0	pass	7,747E+09
104	20:11:29	Type A	035	850	0	pass	3,093E+09
	20:11:29	Type B	027	850	0	pass	3,093E+09
	20:11:29	Type D	016	850	0	pass	3,093E+09
105	20:28:08	Type A	035	950	0	fail	5,653E+08
	20:28:08	Type B	027	950	0	pass	6,535E+09
	20:28:08	Type D	016	950	0	fail	1,255E+09

Tab. C.5.: Continuation logfile ChipIR 2018-09-27

Run	beam on	Type	Dev Nr.	V_{DS} [V]	V_{GS} [V]	Status	f [n/cm^2]
106	21:24:03	FBH	293	200	-2	pass	3,268E+09
	21:24:03	FBH	294	200	-2	pass	3,268E+09
	21:24:03	FBH	295	200	-2	pass	3,268E+09
107	21:40:46	FBH	293	250	-2	pass	3,266E+09
	21:40:46	FBH	294	250	-2	pass	3,266E+09
	21:40:46	FBH	295	250	-2	pass	3,266E+09
108	21:56:41	FBH	293	300	-2	pass	7,838E+09
	21:56:41	FBH	294	300	-2	fail	2,469E+09
	21:56:41	FBH	295	300	-2	leakage	1,046E+09
109	22:36:04	FBH	293	350	-2	pass	3,381E+09
	22:36:04	FBH	295	350	-2	leakage	3,381E+09
110	22:53:08	FBH	293	400	-2	fail	7,113E+08
	22:53:08	FBH	295	400	-2	leakage	7,113E+08
111	23:03:48	FBH	296	200	-2	pass	3,594E+09
	23:03:48	FBH	297	200	-2	pass	3,594E+09
112	23:21:19	FBH	296	250	-2	pass	3,304E+09
	23:21:19	FBH	297	250	-2	pass	3,304E+09
113	23:37:35	FBH	296	300	-2	pass	3,259E+09
	23:37:35	FBH	297	300	-2	pass	3,259E+09
114	23:53:51	FBH	296	350	-2	pass	4,629E+09
	23:53:51	FBH	297	350	-2	pass	4,629E+09

Tab. C.6.: Logfile of the measurement at ChipIR (ISIS -Rutherford Laboratory) 2018-09-28

Run	beam on	Type	Dev Nr.	V_{DS} [V]	V_{GS} [V]	Status	f [n/cm^2]
115	00:16:37	FBH	296	400	-2	pass	1,321E+10
	00:16:37	FBH	297	400	-2	leakage	3,090E+09
116	01:19:20	FBH	296	450	-2	leakage	1,238E+10
	01:19:20	FBH	297	450	-2	leakage	1,238E+10
117	02:55:22	Type A	038	850	0	fail	4,952E+09
	02:55:22	Type B	030	850	0	pass	1,308E+10
	02:55:22	Type D	022	850	0	pass	1,308E+10

Tab. C.6.: Continuation logfile ChipIR 2018-09-27

Run	beam on	Type	Dev Nr.	V_{DS} [V]	V_{GS} [V]	Status	f [n/cm^2]
118	04:02:43	Type B	030	950	0	pass	1,364E+10
	04:02:43	Type D	022	950	0	fail	5,825E+08
119	05:10:02	Type C	010	1000	0	pass	2,479E+10
	05:10:02	Type C	011	1000	0	pass	2,479E+10
	05:10:02	Type C	012	1000	0	pass	2,479E+10

Measurement at CHARM (CERN)

Tab. C.7.: Logfile of the measurement at CERN 2018-11-27

Run	beam on	Type	Dev Nr.	V_{DS} [V]	Status	f [I/cm^2]
		Type A	118	300	pass	1.860E+08
1	10:04	Type A	119	400	pass	1.860E+08
		Type A	120	500	pass	1.860E+08
		Type A	118	500	pass	1.110E+08
2	11:07	Type A	119	600	pass	1.110E+08
		Type A	120	700	pass	1.110E+08
		Type B	120	500	pass	3.060E+08
3	11:45	Type B	121	600	pass	3.060E+08
		Type B	122	700	pass	3.060E+08
		Type C	100	500	leakage	2.790E+08
4	15:41	Type C	101	600	leakage	2.790E+08
		Type C	102	700	leakage	2.790E+08
		Type A	121	700	pass	9.210E+08
5	17:14	Type B	123	700	fail	5.430E+08
		Type C	103	700	pass	9.210E+08
6	22:21	Type A	121	700	pass	4.800E+07
		Type C	103	700	pass	4.800E+07
7	22:38	Type A	121	750	leakage	5.040E+08
		Type C	103	750	fail	3.060E+08

Measurement at Fraunhofer INT

Tab. C.8.: Logfile of the measurement at INT 2019/2020

Date	Run	beam on	Type	Dev Nr.	V_{DS} [V]	Status	f [I/cm^2]
2019-12-19	1	08:58:00	Type B	31	700	pass	4.09E+10
	1	08:58:00	Type B	32	700	pass	4.09E+10
	2	09:52:00	Type B	31	750	pass	4.11E+10
	2	09:52:00	Type B	32	750	pass	4.11E+10
	3	10:30:00	Type B	31	800	pass	4.11E+10
	3	10:30:00	Type B	32	800	pass	4.11E+10
	4	11:59:00	Type B	31	850	pass	4.12E+10
	4	11:59:00	Type B	32	850	pass	4.12E+10
	5	12:46:00	Type B	31	900	pass	4.11E+10
	5	12:46:00	Type B	32	900	pass	4.11E+10
	7	13:34:00	Type A	44	800	pass	4.11E+10
	7	13:34:00	Type A	45	800	pass	4.11E+10
	8	14:11:00	Type A	44	850	pass	4.11E+10
	8	14:11:00	Type A	45	850	fail	3.12E+09
	9	15:10:00	Type A	44	900	pass	4.11E+10
	9	15:10:00	Type A	46	850	fail	5.50E+09
	10	15:49:00	Type A	44	950	pass	4.11E+10
2020-01-08	11	08:48:00	Type A	44	950	pass	4.26E+10
	11	08:48:00	Type A	48	850	pass	4.26E+10
	12	09:45:00	Type A	44	1000	fail	2.30E+10
	13	12:28:00	Type B	33	900	pass	4.15E+10
	13	12:28:00	Type B	34	900	pass	4.15E+10
	16	15:01:00	Type A	47	850	fail	4.55E+09
	16	15:01:00	Type A	49	850	pass	2.51E+10
	17	15:30:00	Type A	49	900	pass	2.07E+10
	18	15:53:00	Type A	49	950	fail	1.81E+10
2020-01-09	19	08:31:00	Type B	35	850	pass	2.19E+10
	19	08:31:00	Type B	36	850	pass	2.19E+10
	20	09:10:00	Type B	35	900	pass	2.17E+10
	20	09:10:00	Type B	36	900	pass	2.17E+10
	21	09:33:00	Type A	50	850	pass	2.23E+10
	21	09:33:00	Type A	51	850	pass	2.23E+10

Tab. C.8.: Continuation logfile INT

Date	Run	beam on	Type	Dev Nr.	V_{DS} [V]	Status	f [I/cm^2]
	22	09:59:00	Type A	50	900	pass	2.35E+10
	22	09:59:00	Type A	51	900	pass	2.35E+10
	23	10:21:00	Type A	50	950	fail	1.16E+10
	23	10:21:00	Type A	51	950	pass	2.20E+10
	24	12:12:00	Type D	24	800	pass	2.18E+10
	24	12:12:00	Type D	25	800	pass	2.18E+10
	25	13:06:00	Type D	24	850	pass	2.18E+10
	25	13:06:00	Type D	25	850	pass	2.18E+10
	26	13:28:00	Type D	24	900	pass	2.19E+10
	26	13:28:00	Type D	25	900	pass	2.19E+10
	27	13:51:00	Type D	24	950	pass	2.19E+10
	27	13:51:00	Type D	25	950	pass	2.19E+10
	28	14:17:00	Type D	24	1000	pass	2.19E+10
	28	14:17:00	Type D	25	1000	pass	2.19E+10
	29	14:45:00	Type D	24	1050	pass	2.18E+10
	29	14:45:00	Type D	25	1050	pass	2.18E+10
	30	15:10:00	Type D	24	1100	pass	4.36E+10
	30	15:10:00	Type D	25	1100	pass	4.36E+10
2020-01-10	31	08:11:00	Type B	35	900	pass	2.25E+10
	31	08:11:00	Type B	36	910	pass	2.25E+10
	32	08:55:00	Type B	35	900	pass	2.18E+10
	32	08:55:00	Type B	36	920	pass	2.18E+10
	33	09:25:00	Type B	35	900	pass	2.19E+10
	33	09:25:00	Type B	36	930	fail	1.22E+08
	34	09:51:00	Type B	35	900	pass	1.71E+10
	35	10:18:00	Type B	35	900	pass	4.44E+10
	36	12:01:00	Type B	38	900	pass	2.17E+10
	36	12:01:00	Type B	39	900	pass	2.17E+10
	37	12:50:00	Type B	38	910	pass	2.18E+10
	37	12:50:00	Type B	39	910	pass	2.18E+10
	38	13:14:00	Type B	38	920	pass	2.19E+10
	38	13:14:00	Type B	39	920	pass	2.19E+10
	39	13:43:00	Type B	38	930	pass	2.17E+10
	39	13:43:00	Type B	39	930	pass	2.17E+10

Tab. C.8.: Continuation logfile INT

Date	Run	beam on	Type	Dev Nr.	V_{DS} [V]	Status	f [I/cm^2]
	40	14:11:00	Type B	38	940	pass	2.18E+10
	40	14:11:00	Type B	39	940	pass	2.18E+10
	41	14:38:00	Type B	38	950	pass	2.11E+10
	41	14:38:00	Type B	39	950	pass	2.11E+10
	42	15:05:00	Type B	38	960	pass	2.20E+10
	42	15:05:00	Type B	39	960	pass	2.20E+10
	43	15:34:00	Type B	38	970	pass	2.21E+10
	43	15:34:00	Type B	39	970	pass	2.21E+10
	44	16:15:00	Type B	38	1040	pass	2.17E+10
	44	16:15:00	Type B	39	1030	pass	2.17E+10
2023-05-02	45	14:01:00	Type B	41	950	pass	5.18E+11
	45	14:01:00	Type B	99	950	pass	5.18E+11
	45	14:01:00	Type B	98	950	pass	5.18E+11
2023-05-03	46	09:45:00	Type B	41	950	pass	4.95E+11
	46	09:45:00	Type B	99	950	pass	4.95E+11
	46	09:45:00	Type B	98	950	pass	4.95E+11
2023-05-05	47	10:10:00	Type A	110	800	pass	4.04E+09
	47	10:10:00	Type A	89	800	pass	4.04E+09
	48	10:33:00	Type A	106	800	pass	1.01E+12
	48	10:33:00	Type A	110	800	pass	1.01E+12
	48	10:33:00	Type A	89	800	pass	1.01E+12

Measurement at OncoRay

Tab. C.9.: Logfile of the measurement at OncoRay (Dresden) 2020-09-23/24/25

Date	Run	beam on	Type	Dev Nr.	V_{DS} [V]	Status	f [p/cm^2]
23.09.2020	1	15:36	Type A	65	800	pass	3,15E+09
	2	15:56	Type A	65	800	pass	4,27E+10
	3	16:11	Type A	65	800	pass	1,16E+12
	4	16:41	Type A	68	800	fail	3,31E+11
	5	16:49	Type A	69	800	fail	4,51E+11
	6	16:55	Type B	42	800	fail	2,24E+11
	7	16:57	Type B	43	800	fail	7,61E+09
	8	16:58	Type B	44	800	fail	7,21E+09
	9	17:00	Type C	37	800	fail	1,03E+11
	10	17:04	Type C	38	800	fail	3,40E+11
	11	17:10	Type C	39	800	fail	7,44E+11
	12	17:19	Type D	50	800	pass	1,17E+12
24.09.2020	13	9:30	Type B	45	800	fail	5,32E+09
	14	9:33	Type B	46	800	fail	9,70E+10
	15	9:47	Type B	47	700	fail	5,41E+09
	16	9:50	Type B	48	600	fail	3,31E+09
	17	9:52	Type B	49	500	fail	8,45E+11
	18	10:14	Type C	40	800	fail	1,05E+12
	19	10:36	Type C	41	700	fail	7,77E+11
	20	10:48	Type C	42	600	fail	4,78E+11
	21	10:55	Type C	43	500	fail	1,53E+12
	22	11:13	Type C	44	400	fail	7,11E+11
	23	11:37	Type A	70	800	fail	8,01E+11
	24	11:48	Type A	71	700	fail	2,73E+12
	25	12:32	Type A	72	600	fail	2,75E+12
	26	12:44	Type A	73	500	pass	1,01E+13
	27	13:12	Type A	74	700	fail	1,76E+12
	28	13:22	Type D	51	800	fail	5,37E+10
	29	12:23	Type D	52	800	fail	1,56E+11
	30	13:26	Type D	53	700	fail	3,05E+12
	31	13:42	Type D	54	600	leak	4,69E+12
	32	14:20	Type A	75	700	fail	1,83E+12

Tab. C.9.: Continuation logfile OncoRay

Date	Run	beam on	Type	Dev Nr.	V_{DS} [V]	Status	f [p/cm^2]
	33	14:31	Type A	76	600	pass	1,01E+13
	34	14:45	Type B	50	700	fail	6,71E+10
	35	14:57	Type B	51	600	fail	6,26E+10
	36	14:58	Type B	52	500	fail	3,48E+11
	37	15:00	Type C	45	700	fail	4,20E+10
	38	15:01	Type C	46	600	fail	5,28E+10
	39	15:04	Type C	47	500	fail	3,36E+12
	40	15:22	Type D	55	600	pass	8,79E+12
	41	16:13	Type A	78	700	fail	5,67E+11
	42	16:16	Type A	79	600	fail	1,10E+12
	43	16:20	Type A	80	500	pass	1,02E+13
	44	16:40	Type B	53	700	fail	5,54E+10
	45	16:42	Type B	54	600	fail	4,19E+11
	46	16:46	Type B	55	500	fail	4,57E+10
	47	16:48	Type C	48	700	fail	1,28E+12
	48	16:57	Type C	49	600	fail	1,52E+12
	49	17:01	Type C	50	500	fail	1,54E+12
	50	17:12	Type D	56	600	pass	3,28E+13
25.09.2020	51	9:20	Type C	51	700	fail	1,20E+12
	52	9:32	Type C	52	600	fail	1,81E+12
	53	9:48	Type C	53	500	fail	3,10E+12
	54	10:00	Type B	56	700	fail	7,43E+10
	55	10:01	Type B	57	700	fail	2,68E+10
	56	10:02	Type B	58	700	fail	7,13E+10
	57	10:04	Type B	59	600	fail	1,82E+11
	58	10:06	Type B	60	600	fail	1,73E+10
	59	10:08	Type B	61	600	fail	1,07E+11
	60	10:10	Type B	62	500	fail	1,43E+11
	61	10:22	Type B	63	500	fail	6,42E+10
	62	10:23	Type C	54	700	fail	3,74E+11
	63	10:26	Type C	55	700	fail	7,36E+11
	64	10:31	Type C	56	600	fail	1,10E+12
	65	10:46	Type C	57	600	fail	1,89E+12
	66	11:00	Type C	58	500	fail	9,36E+11

Tab. C.9.: Continuation logfile OncoRay

Date	Run	beam on	Type	Dev Nr.	V_{DS} [V]	Status	f [p/cm^2]
	67	11:03	Type A	81	700	pass	7,24E+12
	68	14:42	Type A	82	700	fail	1,77E+12
	69	14:52	Type A	83	600	fail	4,62E+12
	70	15:18	Type A	85	600	fail	1,65E+12
	71	15:25	Type A	84	600	pass	9,82E+12
	72	15:40	Type A	86	700	pass	1,02E+13
	73	15:54	Type A	87	500	pass	1,01E+13
	74	16:07	Type D	57	700	fail	1,73E+12
	75	16:12	Type D	58	700	pass	1,05E+13

Acknowledgment

I would like to thank Prof. Dr. Alfred Dewald for the opportunity to work on this topic and for his supervision during the project. I would also like to thank Prof. Dr. Thomas Michely for further reviews of the submitted work.

I would particularly like to thank Dr. Stefan Höffgen for his supervision during the process and for his willingness to explain and discuss, as well as the other members of the Fraunhofer INT NEO-Working group for their significant support in planning and carrying out the measurements.

Furthermore, I would like to thank for the opportunity to realize the experiments for this work in the framework of collaborations at different accelerators. Special partners who made this possible were C. Cazzaniga and C. Frost from the UKRI-Neutron and Muon-Source, P. Fernández-Martínez from CERN and J. Pawelke from OncoRay HZB Dresden.
For one measurement, we received DUTs from the Power Electronics Department around Dr. Würfl of the Ferdinand-Braun-Institut, the Leibnitz-Institut für Höchstfrequenztechnik (Berlin) whose structure and radiation sensitivity could be extensively discussed with Dr. Oliver Hilt preliminary and following to the measurements work.

Finally, I would also like to thank all the proofreaders of my work for their time.

Erklärung

Hiermit versichere ich an Eides statt, dass ich die vorliegende Dissertation selbstständig und ohne die Benutzung anderer als der angegebenen Hilfsmittel und Literatur angefertigt habe. Alle Stellen, die wörtlich oder sinngemäß aus veröffentlichten und nicht veröffentlichten Werken dem Wortlaut oder dem Sinn nach entnommen wurden, sind als solche kenntlich gemacht. Ich versichere an Eides statt, dass diese Dissertation noch keiner anderen Fakultät oder Universität zur Prüfung vorgelegen hat; dass sie - abgesehen von unten angegebenen Teilpublikationen und eingebundenen Artikeln und Manuskripten - noch nicht veröffentlicht worden ist sowie, dass ich eine Veröffentlichung der Dissertation vor Abschluss der Promotion nicht ohne Genehmigung des Promotionsausschusses vornehmen werde. Die Bestimmungen dieser Ordnung sind mir bekannt.
Darüber hinaus erkläre ich hiermit, dass ich die Ordnung zur Sicherung guter wissenschaftlicher Praxis und zum Umgang mit wissenschaftlichem Fehlverhalten der Universität zu Köln gelesen und sie bei der Durchführung der Dissertation zugrundeliegenden Arbeiten und der schriftlich verfassten Dissertation beachtet habe und verpflichte mich hiermit, die dort genannten Vorgaben bei allen wissenschaftlichen Tätigkeiten zu beachten und umzusetzen. Ich versichere, dass die eingereichte elektronische Fassung der eingereichten Druckfassung vollständig entspricht.

Köln den 21. März 2024

Digital unterschrieben von Dorothea Woelk
Datum: 2024.03.21 '13:31:53 +01'00

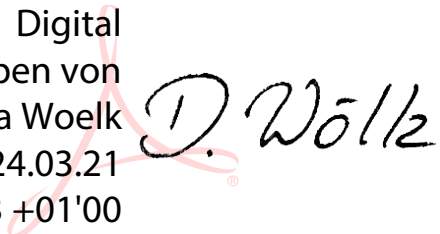

Dorothea Wölk

Erklärung: Die Abbildungen in 3.1 wurden zur Initial vorgelegten Version aktualisiert, nachdem ein Fehler in der Quelltext-Syntax bemerkt wurde.